INSTITUTO SUPERIOR TÉCNICO
Universidade Técnica de Lisboa

UNIVERSITY OF PADUA

FACULTY OF ENGINEERING

MECHANICAL ENGINEERING DEPARTMENT–SECTION MATERIALS

MASTER DEGREE COURSE IN MATERIALS ENGINEERING

MASTER DEGREE THESIS WORK

SELF-ASSEMBLED 3D PHOTONIC CRYSTALS FOR APPLICATIONS IN OPTICAL COMMUNICATIONS

FABBRICAZIONE DI CRISTALLI FOTONICI 3D AUTO-ASSEMBLATI, PER APPLICAZIONI NELLE COMUNICAZIONI OTTICHE

Supervisor (University of Padua): Ch.mo Prof. Massimo Guglielmi

Supervisors (UTL-Lisboa): Profª. Drª. Maria Clara Henriques Batista Gonçalves

Dr. Luís Miguel Amante Fortes

Student: GIULIA SMONKER

n. 603132-IR

ACADEMIC YEAR 2010-2011

Ai miei genitori, e agli amici veri

Ever tried. Ever failed. No matter. Try Again. Fail again. Fail better.
SAMUEL BECKETT

Se vuoi essere felice non fare paragoni, se vuoi essere felice non attribuire colpe.

O valor das coisas não está no tempo em que elas duram,
mas na intensidade com que acontecem.
Por isso existem momentos inesquecíveis,
coisas inexplicáveis e pessoas incomparáveis!
FERNANDO PESSOA

Abstract

English version

Nanotechnology has arisen as one of the most important fields in recent scientific research.

In this thesis work, the activity is mainly focused on the synthesis of nanocomposites for the fabrication of three-dimensional photonic crystals. The 3D inverse opal structures are considered very promising for their peculiar periodic properties in the confinement and propagation of light. To obtain such structures, an innovative method of co-assembly has been tested, based on the self-assembly of polystyrene microspheres, in a suspension containing the infiltrating material, through a mechanism of evaporation.

The introduction of rare-earth ions in this ordered lattice has the purpose of studying a possible increase in light emission efficiency, due to the effect of the photonic band gap.

The ALD method for the co-doping of inverse opals is an innovative work, presenting by the first time a RE active silicon inverse opal. In the present study, the enhancement of the erbium emission at 1.54 microns assumes considerable importance, for future applications in optoelectronics (laser in the IR) and optical communications.

Versione italiana

Il campo delle nanotecnologie è diventato, oggi, uno dei settori più importanti nella ricerca scientifica.

In questo lavoro di tesi, l'attività si è principalmente focalizzata sulla sintesi di nano compositi per la fabbricazione di cristalli fotonici tridimensionali. Le strutture 3D ad opale inverso sono considerate molto promettenti per le loro peculiari proprietà periodiche nelle modalità di confinamento e propagazione della luce. Per l'ottenimento di tali strutture è stato sperimentato un metodo innovativo di co-assembly, basato sul self-assembly di microsfere di polistirene, all'interno di una sospensione contenente il materiale infiltrante, attraverso un meccanismo di evaporazione.

L'introduzione di ioni di terre rare in questo reticolo ordinato ha come scopo lo studio di un possibile incremento dell'efficienza del segnale luminoso, grazie all'effetto del band gap fotonico.

Il metodo ALD per il co-dopaggio di opali inversi rappresenta un approccio innovativo, conducendo per la prima volta ad un opale inverso di silicio attivato con terre rare. Notevole importanza assume, nella presente ricerca, il miglioramento del picco di emissione dell'erbio a 1,5 micron, per future applicazioni nel campo dell' optoelettronica (laser nell'IR) e nelle comunicazioni ottiche.

Table of contents

Introduction

This thesis work, carried out within the mandatory internship required to obtain the Master Degree in Materials Engineering, is part of a research activity involving a bilateral collaboration between the Research Group of "Instituto de Ciência e Engenharia de Materiais e Superfícies-ICEMS" of the "Universidade Tecnica de Lisboa-IST" in Lisbon (Portugal) and the Photonic Crystal Group of "Instituto de Ciencia de Materiales de Madrid-ICMM/CSIC" in Madrid (Spain) and has been developed in both the ICEMS and the ICMM laboratories.

The project is related to the investigation of three dimensional photonic crystals (3D PhCs), nanostructured periodic materials that respond to light waves over a desired range of frequencies, by perfectly reflecting them, or allowing them to propagate only in certain directions, or confining them within a specified volume.
In particular, the focus is on the optical properties of a class of 3D PhC named artificial infiltrated and inverse opals, produced with an innovative co-assembly technique, which integrates the "bottom-up" approach of self-assembly and the sol-gel process in a unique step.
The first part of the experimental work deals with the optimization of the fabrication processes for the opal-based structures, as for the composition of the suspensions and the parameters influencing the growth.
In this phase, the close cooperation with the Photonic Crystal Group of ICMM/CSIC has been useful, due to the experience gained by this group in the synthesis of nano-photonic materials.
The second part of the work focuses on the co-doping of the opal-based structures with active lanthanide ions as emitters (Er^{3+} and Yb^{3+}), in the perspective of an enhancement of the Er^{3+} photoluminescence intensity, derived by the resonance properties of the photonic host structure.
Final aim is related to explore innovative applications in optoelectronics, especially in the area of the low-threshold laser technology.

This thesis includes two sections, theory in the first one, experimental work in the second one. As regards as the theoretical part, a brief review on PhCs is developed in Chapter 1, the self-assembly, sol-gel and co-assembly processes are illustrated in Chapter 2 and Chapter 3 gives

an overview on the emission properties and applications of the rare earth elements used in this study.

The experimental part is elaborated in Chapter 4 and 5; in Chapter 4, the complete description of the fabrication of infiltrated and inverse opal structures is presented, while in Chapter 5 the investigation trials referred to the co-doping can be found.

At the end, a conclusive section has been dedicated to some further research perspectives in this field.

Chapter 1

Three-dimensional photonic crystals

1.1 Introduction

The control of the optical properties of matter has been one of the principal goals of research in recent years. Photonics is a technology that received an enormous amount of interest; its final aim is the use of the photon as an information carrier, like the electron is used in semiconductor technology.

The idea is that, by using light to transfer data between logic devices, higher data rates are achievable using photons instead of electrons, because transmission is faster and less costly, partly due to the absence of charge and mass.

In this sense, the invention of the optical fiber in the seventies has strongly boosted the communication technology[1]. However, the true breakthrough in the control of the optical properties of matter was the introduction of the concept of Photonic Crystal (PhC) by Yablonovitch[2] and John[3] in 1987.

A PhC is a structure that can prevent the propagation of light over a certain band of wavelengths, where the isolated materials are otherwise transparent, while allowing the propagation in some others. For this reason, PhCs are materials that allow the manipulation of light in new and unexpected ways[4] and open a new range of possibilities for the generation and propagation of light.

1.2 Photonic Crystals

1.2.1 Definition

Photonic Crystals can be defined as composite artificial structures with unusual optical properties; they are constructed from alternating regions of dielectric materials with different refractive indices.

In other words, they present a periodic modulation of the dielectric constant (or, in other words, of the refractive index ($n \cong \sqrt{\varepsilon}$) in 1, 2 or 3 dimensions of space.

When the wavelength of the radiation is comparable with the length scale of the periodicity of the modulation, light is strongly scattered and so propagation through the material is precluded (Fig. 1.1).

They are generally built up by semiconductor or dielectric materials, even if in the last years the PhC based on metal or dielectric-metal has also demonstrated excellent optical properties.

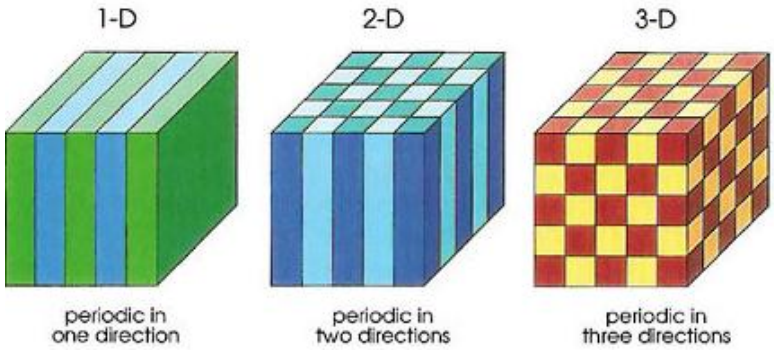

Fig. 1.1 *Schematic depiction of PhC periodic in one, two, and three directions; the different colors represent materials with different dielectric constants (adapted from[4]).*

The fabrication method depends on the number of dimensions desired for the crystal periodicity:

- In a one-dimensional PhC (1D), layers of different dielectric constant may be deposited or adhered together to form a band gap in a single direction. They can be easily generated through programmed deposition of alternating layers of different dielectric materials (e.g. evaporation, sputtering), epitaxial growth (MOCVD, MBE) or the realization of corrugations by lithography and etching. An example is a distributed Bragg reflector, constructed in a short segment of optical fiber that reflects particular wavelengths of light and transmits all others.

- In a two-dimensional PhC (2D), the periodicity exists in two directions and in the third the crystal is homogeneous. These materials are composed of a lattice of dielectric columns; holes may be drilled in a substrate that is transparent to the wavelength of radiation that the band gap is designed to block, produced via selective etching of the underlying substrates through masks. Triangular and square lattices of air gaps become the holes that confine the modes. An example is the *Holey fiber*, which can be made by taking cylindrical rods of glass in hexagonal lattice and then heating and stretching them. It is designed to possess enhanced properties over (normal) optical fibers. For 2D PhC, the fiber draw techniques developed for communications fibers are used, in which structures made of a slab of material can be patterned using techniques borrowed from the semiconductor industry.
- In a three-dimensional PhC (3D), the complicated structure apparently required by such crystals has made them difficult to fabricate. However, in 1991, Yablonovitch demonstrated the first 3D photonic band gap (PBG) in the microwave regime; the structure that he was able to produce involved drilling an array of holes in a transparent material, where the holes of each layer formed an inverse diamond structure. In 1994, a three-dimensional crystal was proposed, specifically designed to be amenable to fabrication at sub-micron length scales[5]. This structure is designed to be fabricated in a layered fashion using two different dielectric materials (in this case, silicon and silicon dioxide); in this design, staggered channels of the lower-dielectric material pass through the high-dielectric substrate, and a triangular lattice of air holes is etched through the whole thing perpendicular to the channels. Then, several other types of structures have been developed[6-7].

Many variations on these topologies continue to be proposed, mainly in conjunction with different fabrication strategies, and we will now talk about three successful approaches:

- *layer-by-layer fabrication*, in which individual crystal layers are deposited one-by-one and etched with a 2D pattern via standard lithographic methods (top-down processing) (Fig. 1.2);
- *colloidal self-assembly*, in which small dielectric spheres in a fluid automatically arrange themselves into close-packed (FCC) crystals by surface forces (bottom-up processing) (Fig. 1.2);

- *holographic lithography*, in which a variety of 3D crystals can be formed by an interference pattern of four laser beams to harden a light-sensitive resin (which is then back-filled and dissolved, as with colloids, to achieve the required index contrast).

The second and third techniques are remarkable for their ability to construct large-scale 3D crystals (thousands of periods) in a short time.

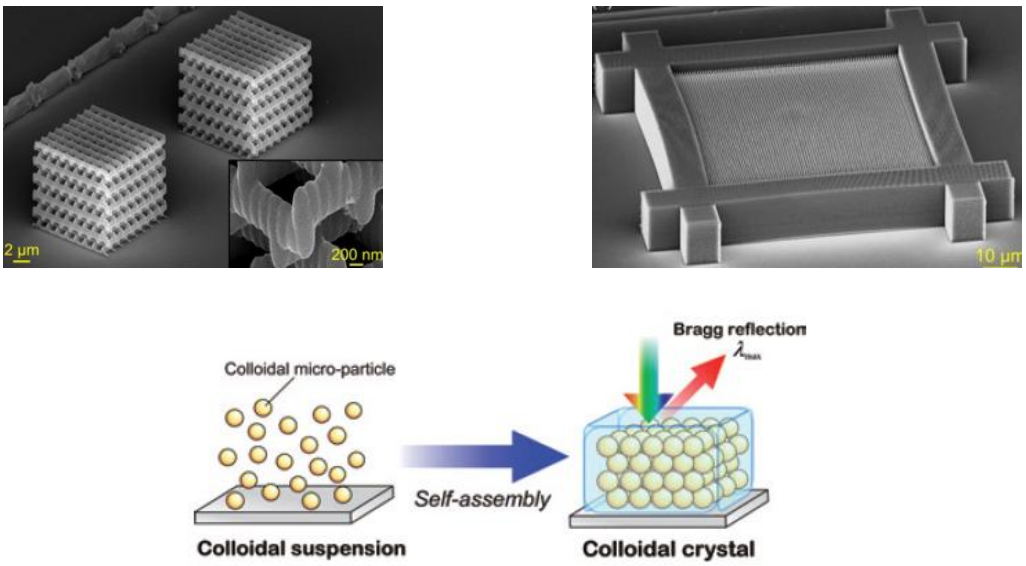

Fig. 1.2 *In the upper part, Woodpile PhC fabricated by direct laser writing (adapted from[8]); in the lower part, schematic illustration of self-assembly of colloidal microparticles (adapted from[9]).*

The major challenge for higher dimensional PhC is certainly in fabrication of these structures with sufficient precision to prevent scattering losses and with processes that can be robustly mass produced[10]. An example of how 3D PhC films and fibers can be produced in mass-scale consists in using a shear-assembly technique, which stacks 200-300 nm colloidal polymer spheres into perfect films of FCC lattice. Since the particles have a softer transparent rubber coating, the films can be stretched and molded, tuning the PBGs and producing striking structural color effects.

Since all these techniques require state-of-the-art and equipment to produce nano-sized features, computer modeling of prospective photonic-crystal structures is also a very important area of research.

1.2.2 Parameters related to the photonic band structure

There are some parameters that, determining the photonic band structure, influence the optical properties of the PhC. They are indicated below:

- *type of crystalline structure* (or *symmetry*); it is how the refraction index is modulated (e.g. triangular or squared structures in 2D or FCC, BCC or diamond in 3D).

  In Fig. 1.3 a representation in the real space of a 1D, 2D and 3D PhC is shown and of the reciprocal space regions for which propagation of light is shielded.

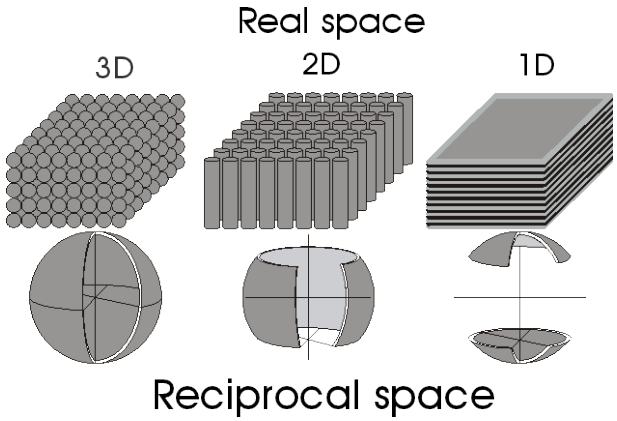

Fig. 1.3 *Real space representation of a PhC and reciprocal space regions for which propagation is shielded (adapted from[11]).*

  In the FCC case of 3D PhC, the higher symmetry of the hexagonal lattice is reflected by the fact that the Brillouin zone is closer to circular than to the square lattice, so the distances in reciprocal space to the principal points of the irreducible zone are similar;

- *dielectric constant contrast;* it is the ratio between the highest and the lowest index of refraction of the two materials of the composite structure.

  Band gaps tend to appear in structures with a higher dielectric contrast, where the scattering of light can be more significant. For a given crystal lattice, there is no PBG until the dielectric contrast is increased to some threshold value. Above this nonzero threshold, the gap opens up and its width usually increases monotonically with the dielectric contrast. A high dielectric constant contrast produces that the optical bands significantly depart from the free photon behavior, producing wider gaps at the Bragg planes (Brillouin zone edges) in the reciprocal space[4] (Fig. 1.4).

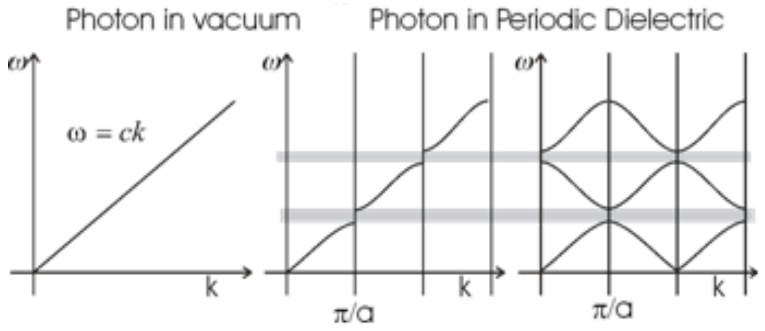

Fig. 1.4 *Energy dispersion relations for a free photon and a photon in a PhC (adapted from[11]).*

- *filling factor*; it is the ratio between the volume occupied by each dielectric with respect to the total volume of the composite;
- *topology*; how the periodic modulation is realized takes into account the disposition of scattering centers, which can be either "cermet" (isolated from each other) or "network" (connected between them); if the scattering centers are regularly arranged in a medium, light is coherently scattered;
- *shape of the scattering centers*; in a composite formed by two dielectrics, we will consider the scattering centre in which light propagates more slowly. Recently, it has been shown that a slight modification of either the symmetry or the shape of the scatterer can enlarge the gap.

1.2.3 Applications of photonic crystals

Concerning the possible applications of PhCs, they were initially proposed as materials capable to forbid the spontaneous emission of a source of light contained inside them and to localize the light. These structures have interesting applications in the microwave to millimeter wave range; for instance, in an antenna mounted on an engineered PBG substrate with a gap at the radiation frequency the losses can be minimized, leading to highly directional transmitters. Other applications include angular filters and cladding material for preventing losses in waveguide structures that contain junctions.

Nevertheless, it is for visible and near-infrared frequencies where PBG materials are likely to have their most important impact.

An interesting application of these structures allows the creation of an enhanced ''superprism'' effect, that is the observation of angular magnification outside the PhC medium; for a single wavelength light beam, a small tilt in the incident angle will result in a much larger change in the propagation direction of the outgoing beam. It would be very useful

for a number of applications ranging from new devices for wavelength-division-multiplexed (WDM) systems to optical elements for beam manipulation within integrated optical circuits[12].

1D PhCs are already in widespread use in the form of thin-film optics, for antireflection coatings on lenses, dichroic mirrors and color changing paints and inks, while 2D PhCs are available in the form of photonic-crystal fibers, which use a microscale structure to confine light for applications in nonlinear devices and guiding wavelengths.

3D periodic structures offer additional features leading to new device concepts, with applications to low-threshold laser devices, optical amplifiers, optical switches, all-optical transistors, light-emitting diodes and important parts of PhC-based optical circuits. Opal-based structures have been used in development of optical sensors (change of the structure to answer an external stimulus)[13], chemical sensors[14] (high specific surface and high sensibility to spectroscopic changes) and as catalysts[15] (porous nature).

These photonic devices could offer some advantages instead of electronic ones, above all a higher operative speed, derived from the intrinsic carriers (photons instead of electrons) and the processes involved in their working (optical answer instead of electronic answer of materials), and less dissipation.

They represent a new frontier in photon-atom interaction phenomena and nonlinear optics. Some representative pictures are shown in Fig. 1.5.

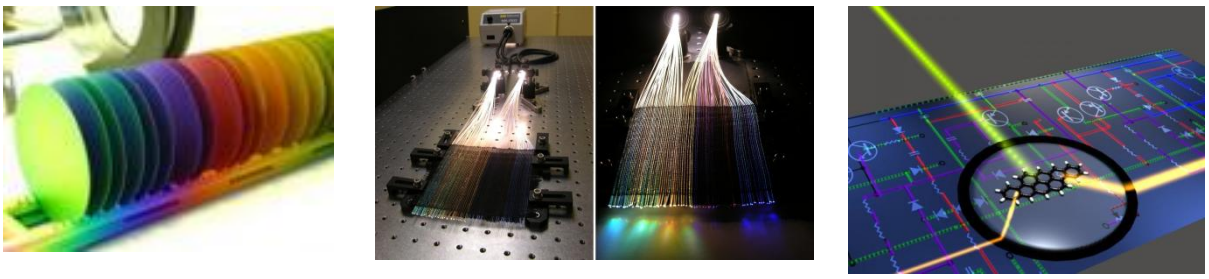

Fig. 1.5 *A new type of electronic ink, based on PhC called P-ink developed by the Toronto based Start-Up Company Opalux (a). Color-tunable photonic textiles using PhC Fibers (b). An artist view of a photonic circuit with molecular building blocks. A single-molecule optical transistor is depicted using a standard symbol for an electronic transistor (c).*

1.3 Propagation of light inside a photonic crystal

The influence of the periodic structure on the electromagnetic response of the medium can lead to profound modifications, as compared with those of an equivalent homogeneous medium.

1.3.1 Band structure

The band structure represents the relation between the energy and the propagation direction of the radiation inside the crystal. It is a tool to predict and study the photonic answer of our system as it permits one to know the allowable energy levels for the photons.

To understand this concept, a comparison between the similarities in the behavior of photons therein and electrons in solids has to be made, using some concepts of solid state physics.

An electronic crystal can be viewed as a periodic distribution of basic units such as atoms or molecules that scatter in the periodic lattice; as a direct consequence of this periodicity in the electronic potential, the energy levels are eventually restricted to certain allowed energy bands separated by energy gaps.

In a PhC, the photons scatter in the periodic lattice in the same way and present bands and gaps for photon states.

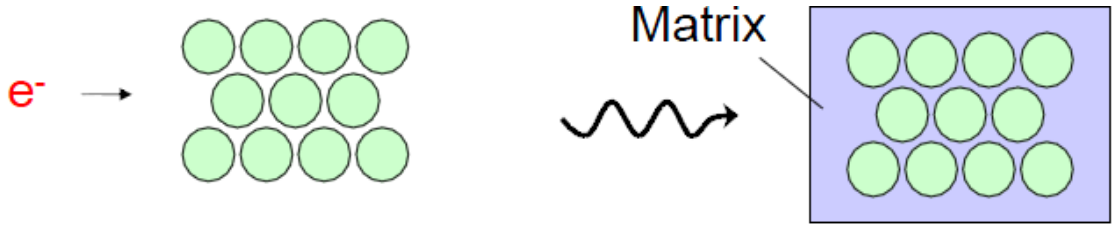

Fig. 1.6 *Crystal lattice of ions in an electronic crystal (left) and typical PhC structure, made of a matrix and spheres having different dielectric properties (right).*

The Schrödinger equation for an electron of effective mass *m* in a crystal, in which the potential is *V(r)*, can be written as:

$$\left[-\frac{\hbar^2}{2m}\nabla^2 + \mathrm{V}(r)\right]\Psi(\mathrm{r}) = \mathrm{E}\Psi(\mathrm{r}) \quad [1.1]$$

where *V(r)* is a periodic function with the periodicity of the lattice, R: $V(r) = V(r + R)$.

The eigenstates of this equation are also periodic functions with period R. The dispersion relationship derived, *E(k)*, will present a forbidden band for all energies E which have imaginary values.

Similarly, in a medium in which a spatial modulation of the dielectric constant $\varepsilon(r)$ exists, photon propagation is governed by the classical wave equation.

Maxwell's equations can be treated as an eigenproblem, in analogue with Schrödinger's equation. It can be expressed in terms of the magnetic field H(r) as:

$$\nabla \times \left[\frac{1}{\varepsilon(r)} \nabla \times H(r)\right] = \left(\frac{\omega}{c}\right)^2 H(r) \quad [1.2]$$

Where ε is the dielectric function and c is the speed of light. This is an eigenvalue equation, with eigenvalue (ω/c). In a PhC, $\varepsilon(r)$ is a periodic function: $\varepsilon(r) = \varepsilon(r + R)$.

The electron wave equation is not scalable, since an intrinsic length measure is associated to the electron (de Broglie wavelength) whereby the potential periodicity can be gauged. This restriction does not apply for photons.

The photon wave equation is scalable, hence if a PhC presents a given periodicity length, it will show photonic bands in a certain range of frequency and a scaling of it will result in a new system with exactly the same band scheme, only accordingly scaled. If we halve the size we double the energies. For example, in presence of a PhC of period a with a gap in a frequency ν, if we scale of a factor L (periodicity La), the gap will appear at ν/L. This permits the production of models at a different scale, normally with a bigger lattice parameter, for extrapolating the properties of the system in exam.

Thus, the same linear-algebraic theorems as those in quantum mechanics can be applied to the electromagnetic wave solutions. As the resolution of the electron wave equation gives the band diagram by means of the electron standing waves, the allowed energies (bands) and the forbidden energies (band gaps), solving the photon wave equation will permit to know the allowed and forbidden frequencies for photons.

1.3.2 Bloch waves

The resolution of the problem makes use of the Bloch approach, who firstly studied wave propagation in three-dimensionally periodic media in 1928. Bloch-wave description can be applied to any wave-like phenomenon in a periodic medium, exactly like photons in a periodic dielectric structure and represents a demonstration that waves in a 3D periodic medium can propagate without scattering.

Bloch's theorem states that the eigenfunctions for such a eigenproblem may be written as the product of a plane wave envelope function e^{ikx} and a periodic function (Bloch function)

$H_{nk}(x)$ that has the same periodicity as the dielectric lattice, with eigenvalues $\omega_n(k)$, $H(x) = e^{ikx}H_{nk}(x)$. The periodic function $H_{nk}(x)$ satisfies:

$$(\nabla + \mathrm{i}k) \times \left[\frac{1}{\varepsilon}(\nabla + \mathrm{i}k) \times H_{nk}\right] = \left(\frac{\omega_n(k)}{c}\right)^2 H_{nk} \quad [1.3]$$

yielding a different Hermitian eigenproblem over the primitive cell of the lattice at each Bloch wavevector *k*. This primitive cell is a finite domain if the structure is periodic in all directions, leading to discrete eigenvalues (n=1, 2,…).

These eigenvalues $\omega_n(k)$ are continuous functions of *k*, forming discrete bands when plotted versus the latter, in a band structure or dispersion diagram (both ω and k are conserved quantities, meaning that a band diagram maps out all possible interactions in the system).

Due to this periodicity, one need only to compute the eigensolutions for k within the primitive cell of this reciprocal lattice or, more conventionally, one considers the set of inequivalent wavevectors closest to the k = 0 origin, within a region called the first Brillouin zone.

Furthermore, the first Brillouin zone may itself be redundant if the crystal possesses additional symmetries such as mirror planes; by eliminating these redundant regions, one obtains the irreducible Brillouin zone, a convex polyhedron that can be found tabulated for most crystalline structures.

An example for a square and hexagonal lattice is shown in Fig. 1.7.

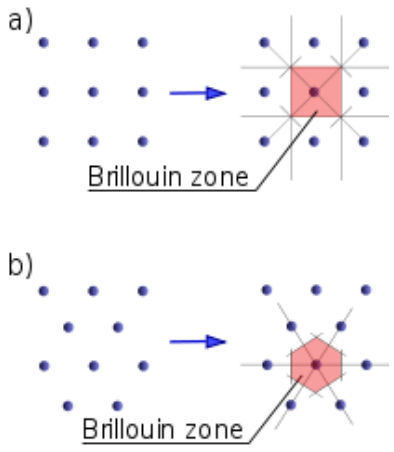

Fig. 1.7 *The reciprocal lattices (dots) and corresponding first Brillouin zones of (a) square lattice and (b) hexagonal lattice (adapted from[16]).*

Therefore, the band structure is the collection of energy eigenstates. The solutions are separated in energy by a finite spacing at each *k*, so if there is a separation that extends over all wave vectors, it is called a complete band gap.

From the band structure, all the properties of particles in a periodic potential can be calculated.

The demonstration of the fact that waves in a 3D periodic medium can propagate without scattering is a corollary of this result, and lays in the fact that the Bloch wave vector *k* is a conserved quantity in a crystalline system and hence the group velocity of the wave is conserved.

1.3.3 Photonic band gap

The optical forbidden gaps are frequency ranges where light does not propagate in the composite and are originated from the periodicity in the refractive index.

To design PhC systems, it is essential to engineer the location and size of the band gap. In Fig. 1.8 the blue lines are allowed frequency states, in yellow the regions of PBG, where the travelling of photons is prohibited.

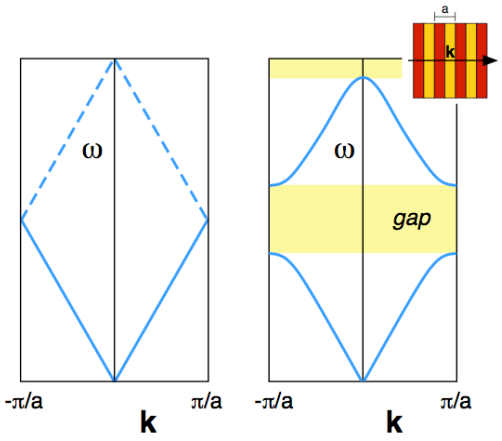

Fig. 1.8 *Band diagram (dispersion relation) with frequency ω versus wave number k of a uniform, ideal 1D medium, where the dashed lines represent a higher order Brillouin Zone (left). Schematic effect on the bands of a real periodic dielectric variation (inset), where a gap has been opened (right) (adapted from[17]).*

The size of the PBG depends on the difference between the refractive index of the two dielectric regions; if the difference is small, the band gap will be small.

A complete PBG (full gap) is a range of ω that are forbidden regardless of the propagation direction in the PhC, where no propagating (real *k*) solutions of Maxwell's equations exist for any *k*, while propagating states surround the gap above and below.

There are also incomplete PBGs (pseudo gaps), which does not occur independently of the propagation direction and therefore, only exist over a subset of all possible wave vectors, polarizations and symmetries.

Representation of triangular and square 2D crystals are showed in Fig. 1.9 to highlight the formation of a full gap and a pseudo gap, respectively.

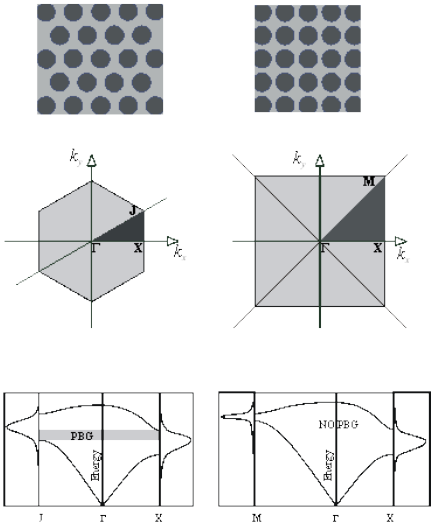

Fig. 1.9 *Real and reciprocal space representation of triangular and square 2D crystals to highlight the formation of a full band gap and a pseudo gap (adapted from[11]).*

These gaps can be used, for example, to completely block the propagation of photons irrespective of their polarization or moving direction, to localize photons to the specific area at certain frequencies, to manipulate the dynamics of a spontaneous or stimulated emission process and to serve as a lossless waveguide to direct the flow of light along a specific path.

1.4 3D photonic crystals

From the technological point of view, the fabrication of a complete PBG material is much more interesting, because complete confinement of light can only be achieved by extending the PBG into the third dimension, thus all the investigation in the last years has been following this route.

1.4.1 3D photonic crystals structures

Quite advanced examples have been demonstrating the construction of structures with complete band gaps and, in many cases, these structures have been characterized at wavelengths ranging from the microwave regime to the infrared regime.

The 3D photonic structures known are:

- diamond lattices of air holes;
- drilled dielectrics known as Yablonovite;
- woodpile structures of orthogonal dielectric columns; these "rods" are repeatedly etched by beam lithography, filled in and then new material is deposited thereon, repeating the process until the structure is of the desired height. The fill-in material is then dissolved using an agent that can dissolve the fill in material but not the deposition material;
- inverse opals, consisting of regular arrangements of spherical void spaces surrounded by solid walls. They are made after solidification of an infiltrating solution in the void spaces of synthetic opal templates, made of colloidal spheres, followed by the removal of the template. The spheres are dissolved using an heating treatment or a chemical attack;
- stacks of alternating two-dimensional crystals of rods and holes (a more general class of PhCs than Yablonovite).

In the following diagrams are showed the photonic band structures for this kind of structures. The wave vector varies across the irreducible Brillouin zone between the labeled high-symmetry points and the characteristic complete PBG is shown in yellow.

➢ **Diamond lattice**

The first prototype of Yablonovitch in 1991, that showed a full PBG in the microwave region, consisted of a modified diamond structure, carried out by drilling holes in a bulk material along three well chosen directions, with a typical length scale of the order of mm (Fig. 1.10).

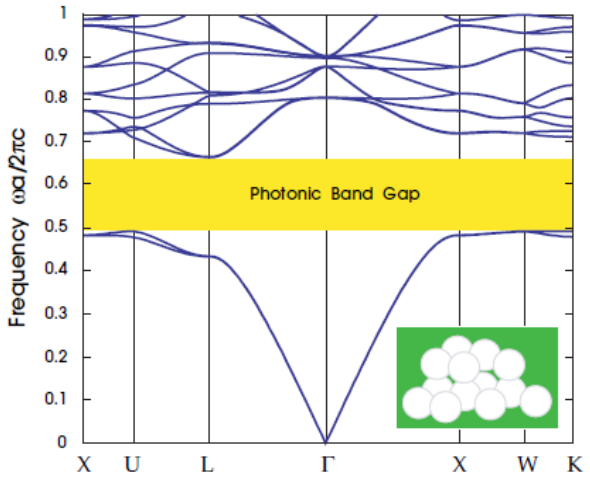

Fig. 1.10 *The photonic band structure for the lowest bands of a diamond lattice of air spheres in a high dielectric material (ε=13) (adapted from[4]).*

In fact, an arrangement of dielectric spheres in a diamond like structure, once provided the filling factor properly chosen, clearly possess a full photonic gap[18]; it is located between the second and the third band for a refractive index contrast superior to 2 and a low filling fraction of the material of superior index. In this sort of symmetry, a threshold value of 4 for the dielectric constant contrast is needed to open a full gap.

- **Yablonovite**

Yablonovite is a distorted rod-connected diamond structure that presents complete band gap (Fig. 1.11).

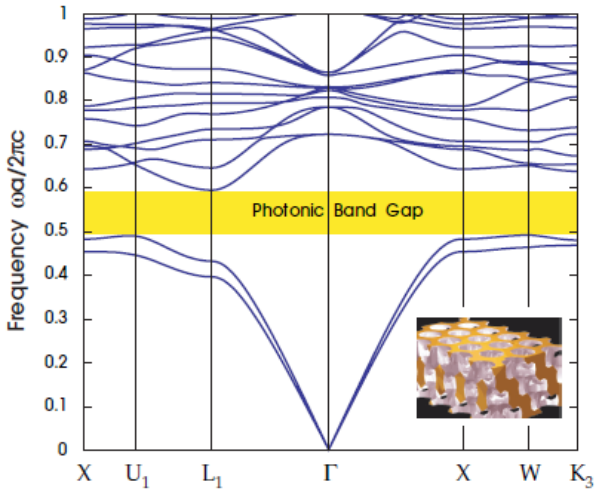

Fig. 1.11 *The photonic band structure for the lowest bands of Yablonovite (adapted from[4]).*

The rod-connected diamond has open air channels along the (110) directions. Thus, this structure is made by the sculpting of a cubic dielectric block by drilling cylindrical holes along the six equivalent (110) cubic directions[19].

- **Woodpile**

The woodpile Face Centered Tetragonal (FCT) structure possesses one-dimensional (1D) periodic structure on each layer and is produced by controlling the period of both horizontal/vertical directions and the aspect ratio of the periodic structures[20]. The photonic band structure with the complete PBG is represented in Fig. 1.12.

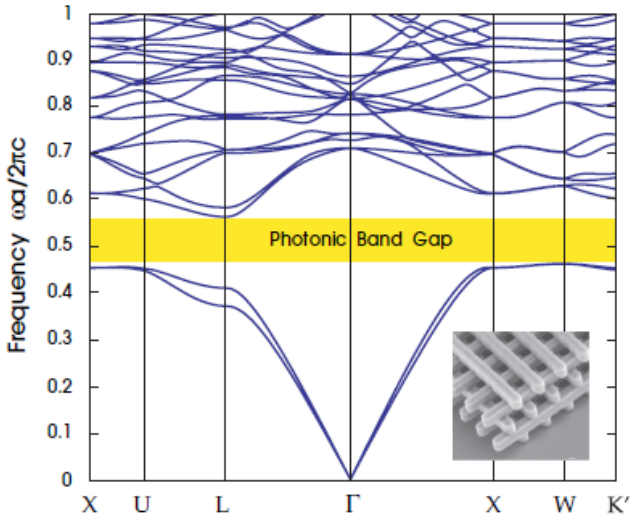

Fig. 1.12 *The photonic band structure for the lowest bands of the woodpile structure with ε=13 in air (adapted from[4]).*

The irreducible Brillouin zone is larger than that of the FCC lattice, due to the reduced symmetry.

- **Inverse opal**

In FCC structures, the first gap opens in the Γ-L direction, hence transmission at frequencies within this region is strongly inhibited, giving rise to a dip in transmittance and a peak in reflectance.

Early work on colloidal crystal[21], artificial opals and inverse opals[22] employed reflection and transmission spectra to map the dispersion of the L-pseudogap in the surroundings of the L point in reciprocal space, to determine the presence of higher order stop bands and also the full PBG in inverse opals. In fact, FCC dielectric structures do not have a PBG that extends throughout the Brillouin zone, because of the degeneration in correspondence to the zones W and U; for this particular symmetry, the appearance of a PBG requires a larger refractive index contrast $\delta n = \frac{n_2}{n_1}$ and a different topology.

For instance, a full PBG for an inverse opal compact FCC structure can be achieved provided a contrast of dielectric constant of 8 is reached. In these conditions, there is the presence of a complete PBG (yellow) between the eighth and ninth band (Fig. 1.13).

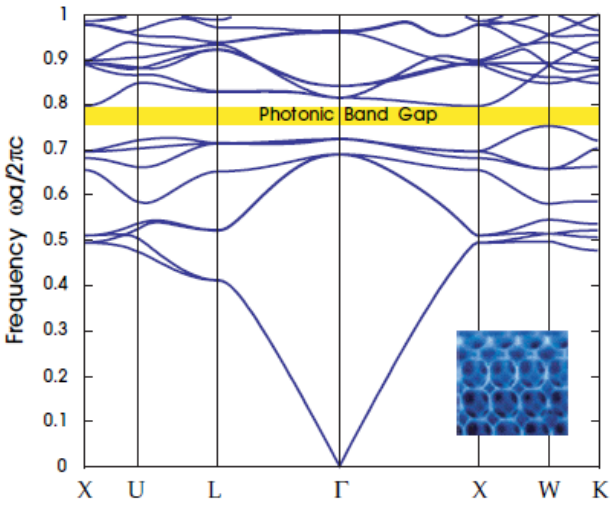

Fig. 1.13 *The photonic band structure for the lowest bands of an inverse opal structure: a face-centered cubic (fcc) lattice of close-packed air spheres in dielectric (ε=13) (adapted from[4]).*

The stocking direction of inverse opals is (111) and the normal reflectance means correspond to Γ-L direction.

The measure of other crystallographic faces different from (111) or the measure in other directions different from the Γ-L is possible by carving or fracture[23], to evidence the existence of a complete photonic gap in these structures.

1.4.2 Opal and inverse opal structures

All the 3D structures presented require specific equipments and precise technologies to be obtained. To study the formation of a complete PBG, in this work we will focus on the inverse opal structure, because it is an FCC structure more stable and easy to achieve.

Recently, materials based on self-organized structures have revealed themselves as a real possibility to obtain robust PBG materials with gaps in the visible and infra-red regions of the electromagnetic spectrum.

The easier and more economic way to fabricate inverse opal structures is based on artificial opals, resulting from the imitation of the natural opal structure, a 3D arrangement of ordered spheres in an FCC structure. In fact, the precious opal is one of the finest natural examples of highly ordered arrays of amorphous colloidal spheres of silica (SiO_2), which can be formed over a very long range (typically on the order of a few millimeters to one centimeter).

To achieve the formation of an artificial opal, the sol (colloidal suspension of solid particles in a liquid) in which the spheres are suspended has to evaporate in a controlled way to produce the crystallization of particles on a substrate.

For an opal PhC (Fig. 1.14) made of silica or polymer spheres embedded in air (FCC lattice of close-packed dielectric spheres), the difference in the refractive index contrast between the two materials is enough for the opening of a pseudo gap but not of a complete one[4]. As seen in Fig. 1.15, small gaps appear only at particular points in the band diagram.

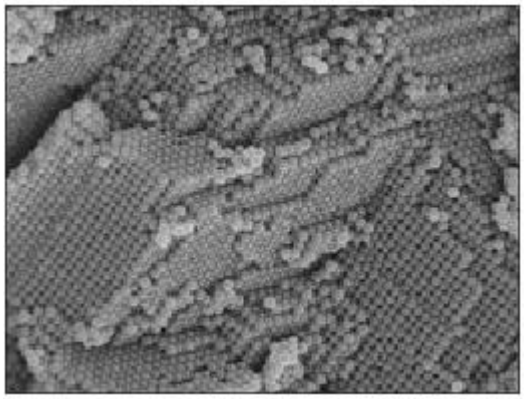

Fig. 1.14 *Opal PhC.*

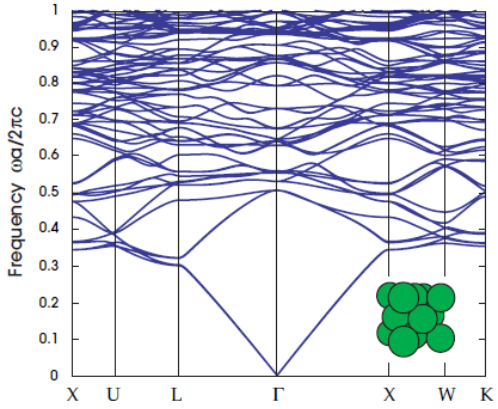

Fig. 1.15 *The photonic band structure for the lowest-frequency electromagnetic modes of a face-centered cubic (FCC) lattice of close-packed dielectric spheres (ε=13) in air (adapted from[4]).*

The *k* vectors of these partial gaps correspond to particular directions at which a particular wavelength, and therefore a particular color, is reflected. The narrowness and directionality of these gaps are the source of the bright, iridescent colors that make natural opal gems so attractive. This sort of structural color is responsible for many of the iridescent colors found in nature; iridescent surfaces are due to optical wave interference in the multilayer structure present at the wavelength scale underneath the surface (Fig. 1.16).

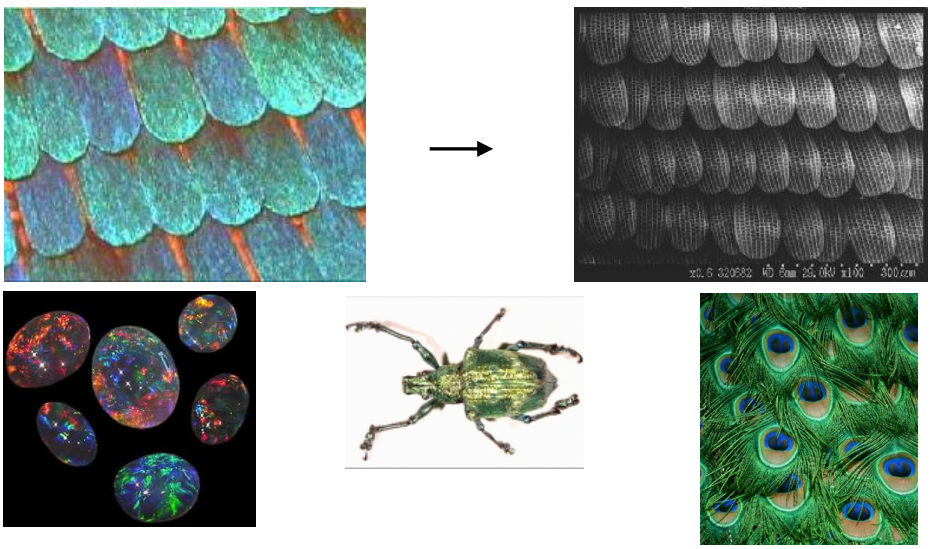

Fig. 1.16 *Iridescent, structural colors found in nature: butterfly wings, opal gems, beetle and peacock feathers.*

Considering an example, the beetle has a green iridescence which comes from sub-micron tetrahedral structures on its surface[24]. It transpires that a single beetle scale is not a continuous crystal, but includes some 200 pieces of chitin, each with the diamond-like structure but oriented to different directions. So each piece reflects a slightly different wavelength or shade of green.

For the exploitation of these peculiar properties, scientific teams are now trying to copy the structure in a semiconducting material to make a controllable optical element.

Starting from the artificial opal, it can be used like a template to fabricate the inverse opal.

By replacement of the material constituent the photonic structure by voids and vice-versa, an "inverted-structure" is obtained.

The associated procedure usually consists in infiltrating the ordered assembly of spheres with a type of solid-forming material or precursor that is able to completely penetrate the void space between the building blocks.

Subsequently, the infiltrated material is converted into a solid and then the template is selectively removed by chemical etching or calcination (Fig. 1.17).

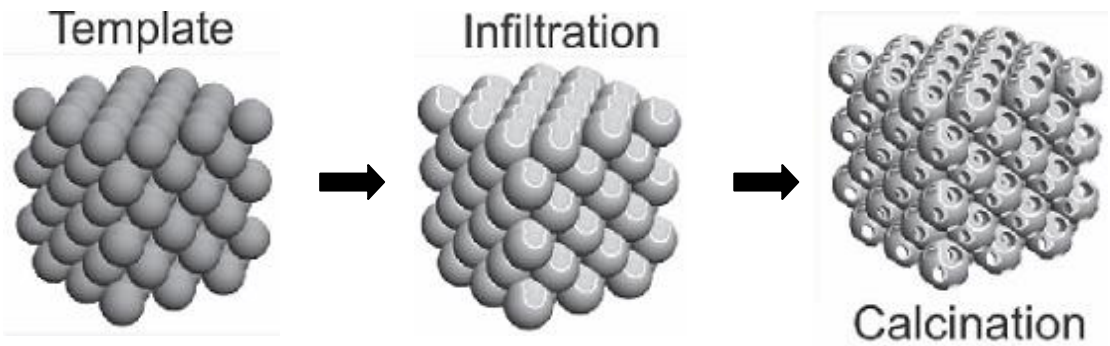

Fig. 1.17 *Fabrication of the inverse opal.*

This leads to a material built by nanosized bridges and junctions around a regular and compact arrangement of air spheres. In many cases, the shrinkage associated with the removal of the template reduces the size of the macropores by 10-30% of the initial structure size[25]. It turns out that the inverse structure can have a complete PBG; only a refractive index contrast superior of 2.9 guarantees the opening of a complete PBG between the eighth and ninth band, so the infiltrating dielectric material have to present high refraction index (n>2.9).

The first inverse opal with a sufficient contrast was built in 2000 by Blanco and co-workers[26] and was based on silicon.

1.5 Modified Bragg's law

The physical phenomenon which describes the PhC behavior in the interaction with an electromagnetic wave is the localization of light, which is achieved from the scattering and interference produced by a coherent wave in a periodic structure.

The periodic arrays of submicrometer spherical particles provide similar arrays of interstitial voids, which act as a natural diffraction grating for visible light waves, particularly when the interstitial spacing is of the same order of magnitude as the incident lightwave[27]. It gives rise to peculiar and interesting optical properties.

When white light shines upon the PhC, certain wavelengths do not penetrate very far and are selectively reflected from the periodic scatterers of the PhC, like the highest density plane (111) in a face-centered cubic (FCC) structure (Fig. 1.18).

(a) *(b)*

Fig. 1.18 *Diffraction of white light by FCC colloidal crystals at the (111) crystal planes (a) and schematic representation of FCC crystalline cell with (111) planes outlined (b).*

Each wavelength is reflected exactly at the same frequency as the incident light, regardless of its direction or polarization state. Then, wherever in space the radiation interferes constructively, by adding scattered rays with phase differences multiple of 2π, a colored crystal will be observed.

The wavelength (or frequency) range which is forbidden to propagate through the periodic structure is called a *stop band* and corresponds to a *PBG* in the optical density of states. The remaining transmitted light generates the complementary color.

Due to the periodicity of the structures involved, an analogy with X-ray diffraction in electronic crystals can be made, and the modified form of Bragg's law for the optical region can be applied for the description of the phenomenon.

Bragg's law of diffraction applies to any wave in any periodic object; a periodic object reflects incident wave when the Bragg's law conditions are satisfied by the light wavelength and the interplanar spacing of the crystal.

The periodicity of PhC structure depends on the lattice parameter; for this reason, light with wavelength of the order of the lattice parameter will suffer diffraction.

The Bragg condition is represented in this formula:

$$m\lambda = 2d_{hkl}\, cos\theta_{int} \quad [1.4]$$

where m is the diffraction order (m=1,2,3…), λ is the free space wavelength of the light, d_{hkl} the interplanar spacing between the scattering planes (labeled by the Miller indices) and θ_{int} is the internal angle.

Considering a flat interface between two dielectrics ε_1 and ε_2, light can be described by a ray with an incident angle θ_1 and a refracted angle θ_2 given by Snell's law. In the experimental measurements the external incidence angle on the sample is controlled, so:

$$n_{int} sin\theta_{int} = n_{ext} sin\theta_{ext} \quad [1.5]$$

where the indexes refer to the external and internal refractive indexes and angles.

The resulting modified form of Bragg's law for the optical region, that takes into account Snell's law of refraction is[28]:

$$m\lambda = 2d_{hkl}\sqrt{(n_{eff}^2 - \sin^2\theta_{ext})} \quad [1.6]$$

where n_{eff} is the effective refractive index of the composite PhC.

The term n_{eff}^2 is sometimes be substituted by the ε_{eff}, dielectric constant of the materials that compose the crystal ($\varepsilon_{eff} = n^2_{eff}$). For calculating the effective refractive index, among the approximated expressions proposed for the bulk dielectric properties of inhomogeneous materials, the simplest ones are the mixing rules, based on the additive property:

$$n_{eff}^2 = f n_1^2 + (1-f) n_2^2 \quad [1.7]$$

This form of Bragg's law allows one to know the gap position in first approximation, because represents the longest wavelength diffracted by the packing, for an observer perpendicular to the surface, but the applicability is restricted to systems with moderate dielectric contrast.

The interplanar spacing d_{hkl} for (*hkl*) planes in the FCC lattice was calculated using the following relation: $d_{hkl} = \frac{a}{\sqrt{(h^2+k^2+l^2)}}$ [1.8], where *a* is the unit cell size.

The notable (*hkl*) sets of the diffraction planes that strongly participate in light diffraction of an FCC type lattice are (111), (220) and (200); the focus will be on the (111) set of planes because is the most densely packed.

The following relation links the interplanar spacing *d* with the colloidal sphere diameter D and it is derived from structural parameters:

$$d_{111} = \frac{a}{\sqrt{3}} \text{ where } a = \frac{2D}{\sqrt{2}} \quad [1.9]$$

The diameter of the spheres is comparable to the wavelength of visible light, so the opal acts as 3D diffraction lattice for visible light and its colors are determined by the diameter of the spheres and the refraction index of the composite. Therefore, the control of these parameters can allow the continuous adjustment of the diffraction wavelengths of the composite.

References

1 Dutton, H. J. R. *Understanding optical communications*, (Prentice Hall PTR, 1998).

2 Yablonovitch, E. *Inhibited Spontaneous Emission in Solid-State Physics and Electronics*, Phys Rev Lett, 58, 20 (1987) 2059.

3 John, S. *Strong localization of photons in certain disordered dielectric superlattices*, Phys Rev Lett, 58, 23 (1987) 2486.

4 Joannopoulos J.D., J. S., Winn JN & Meade RD. *Photonic Crystals: Molding the Flow of Light*, 2°ed edn, (2008).

5 Fan, S., Villeneuve, P. R., Meade, R. D. & Joannopoulos, J. D. *Design of three-dimensional photonic crystals at submicron lengthscales*, Appl Phys Lett, 65, 11 (1994) 1466-1468.

6 Inoue, K., Wada, M., Sakoda, K., Hayashi, M., Fukushima, T. & Yamanaka, A. *Near-infrared photonic band gap of two-dimensional triangular air-rod lattices as revealed by transmittance measurement*, Phys Rev B, 53, 3 (1996) 1010.

7 Noda, S., Tomoda, K., Yamamoto, N. & Chutinan, A. *Full Three-Dimensional Photonic Bandgap Crystals at Near-Infrared Wavelengths*, Science, 289, 5479 (2000) 604-606.

8 <http://www.aph.kit.edu/>.

9 Furumi, S., Fudouzi, H. & Sawada, T. *Self-organized colloidal crystals for photonics and laser applications*, Laser & Photonics Reviews, 4, 2 (2010) 205-220.

10 Busch K., L. S., Wehrspohn R., Foll H. . *Photonic Crystals - Advances in Design, Fabrication and Characterization*, (2003).

11 <http://luxrerum.icmm.csic.es/>.

12 Tandon, S. N., Soljacic, M., Petrich, G. S., Joannopoulos, J. D. & Kolodziejski, L. A. *The superprism effect using large area 2D-periodic photonic crystal slabs*, Photonics and Nanostructures - Fundamentals and Applications, 3, 1 (2005) 10-18.

13 Pan, G. S., Kesavamoorthy, R. & Asher, S. A. *Optically nonlinear Bragg diffracting nanosecond optical switches*, Phys Rev Lett, 78, 20 (1997) 3860-3863.

14 Lee, K. & Asher, S. A. *Photonic crystal chemical sensors: pH and ionic strength*, J Am Chem Soc, 122, 39 (2000) 9534-9537.

15 Bartlett, P. N., Dunford, T. & Ghanem, M. A. *Templated electrochemical deposition of nanostructured macroporous PbO2*, Journal of Materials Chemistry, 12, 10 (2002) 3130-3135.

16 <http://wapedia.mobi/en/Brillouin_zone>.

17 <http://ab-initio.mit.edu/photons/tutorial/photonic-intro.pdf>.

18 Ho, K. M., Chan, C. T. & Soukoulis, C. M. *Existence of a photonic gap in periodic dielectric structures*, Phys Rev Lett, 65, 25 (1990) 3152.

19 Yablonovitch, E., Gmitter, T. J. & Leung, K. M. *Photonic band structure: The face-centered-cubic case employing nonspherical atoms*, Phys Rev Lett, 67, 17 (1991) 2295.

20 Wang, L., Zhang, S., Wang, Q., Chen, J., Jiang, W. & Chen, R. *Fabrication of three-dimensional (3D) woodpile structure photonic crystal with layer by layer e-beam lithography*, Applied Physics A: Materials Science & Processing, 95, 2 (2009) 329-334.

21 Tarhan, I. I. & Watson, G. H. *Photonic band structure of fcc colloidal crystals*, Phys Rev Lett, 76, 2 (1996) 315-318.

22 Thijssen, M. S. *et al. Inhibited light propagation and broadband reflection in photonic air-sphere crystals*, Physical Review Letters, 83, 14 (1999) 2730-2733.

23 Palacios-Lidon *et al. Optical study of the full photonic band gap in silicon inverse opals*, Vol. 81 (American Institute of Physics, 2002).

24 <http://www.electronicsweekly.com/Articles/2008/05/27/43802/beetle-reveals-natural-photonic-crystal-ideal-for-semiconducting.htm>.

25 Lytle J.C., S. A. in *Annual Review of Nano Research* Vol. 1 (ed Brinker J. Cao G.) 1-64 (World Scientific Publisher Co., 2006).

26 Blanco, A. *et al. Large-scale synthesis of a silicon photonic crystal with a complete three-dimensional bandgap near 1.5 micrometres*, Nature, 405, 6785 (2000) 437-440.

27 Hiltner, P. A. & Krieger, I. M. *Diffraction of light by ordered suspensions*, The Journal of Physical Chemistry, 73, 7 (1969) 2386-2389.

28 Almeida R.M, G. M. C. in *Photonic glasses* (ed Rolindes Balda) 67-88 (2006).

Chapter 2

Self-assembly and sol-gel processes

2.1 Introduction

In the last years, numerous nanofabrication strategies are being pursued to fabricate photonic crystals. Among them, colloidal self-assembly[1] and multi-beam interference lithography[2] are great tools to build large area single crystals with interesting optical properties.

In many areas of science and technology, the synthesis of materials by the "bottom-up" approach of colloidal self-assembly recently has been of great popularity as an alternative to the conventional "top-down" lithographic fabrication, due to several operative advantages.

They include a wider versatility with respect to the choice of materials, a relative ease of access and a richness of results offered. The cost of implementation is low and unbeatable if compared with the expensive lithography equipment; moreover, the time needed for the sample production is reduced about several times and an increase in the limit thickness can be achieved.

2.2 Colloidal stability

One system presents colloidal nature when a substance is microscopically dispersed uniformly throughout another substance and the dimensions of the dispersed phase stay in the range 1-1000 nm.

In a colloidal system, interactions are mainly dominated by short-range forces, such as van der Waals attractions, electrostatic interactions and also by entropic and steric forces. The inertia of the dispersed phase is small enough that it exhibits Brownian motion (or Brownian diffusion), a rapid and random walk driven by the momentum imparted by collisions with molecules of the suspending medium, which homogenize the distribution of various species in the solution.

Typically, in a dispersion, the Brownian motion competes with the gravitational force, which induces the sedimentation of the particles. In certain circumstances, may occur that particles adhere together (due to interparticle attraction) and form aggregates of increasing size, which may settle out due to gravity; in this case, the formation of an initial aggregation is called "flocculation" and this process is reversible ("deflocculation"). If the aggregate changes to a much denser form it is said to undergo "coagulation", in an irreversible way (Fig. 2.1).

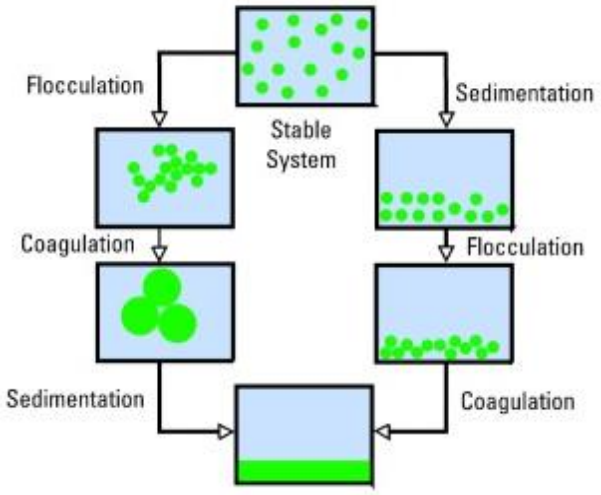

Fig. 2.1 *Flocculation, coagulation and sedimentation in colloidal systems.*

Therefore, a colloidal system is metastable from a thermodynamic point of view, but stable from a kinetic one.

2.2.1 Electric double-layer theory

The agglomeration occurrence depends on the forces be produced between particles. The long order attraction forces are present in all the solid surfaces and take place from a minimum distance between two particles, while the electrostatic repulsion forces are associated to the superficial charges and are attenuated to a varied extent by the presence of the double layers.

In a solution, there always exist surface charges determining both ions and counter ions, which have charge opposite to that of the determining ions. The extent of the diffuse double layer is dependent on the ionic strength of the electrolytes and the valence of each of the ions and it has a typical thickness of about 10 nm.

The important factor to evaluate the aggregation between two charged particles is not the electric charge itself but the electric potential, related to the organization of the charges in the surface and the counter-ions (Fig. 2.2).

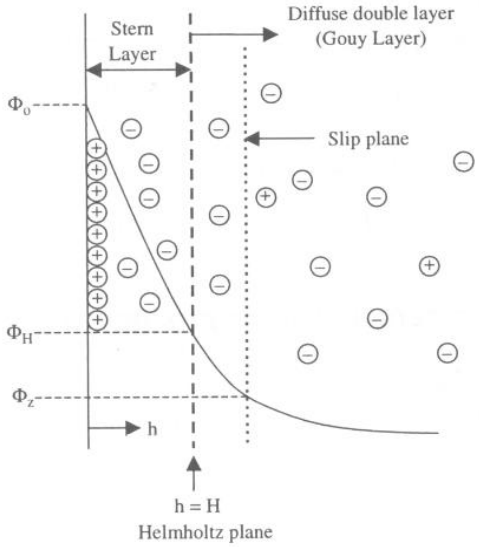

Fig. 2.2 *Schematic illustration of the electrical double layer structure and the electric potential near the solid surface. Surface charge is assumed to be positive.*

The continue vertical line in Fig. 2.2 represents the limit of a solid surface in contact with water, with a charge associated (positive, in this case). The negative counter ions are distributed along the distance and the electric potential is given as a function of the distance from the solid surface.

According to Stern's theory, a fraction of these counter ions, with opposite charge in relation to the surface, is adsorbed, forming a mono layer near the surface, named "Stern layer". It is evidenced a fall in the potential until the Stern layer, due to the high concentration of counter ions, from the surface value (defined as Nernst potential Φ_0) to the limit value of the Stern

layer (defined as Stern potential Φ_H). In colloidal systems, Stern potential is determinant because of its sensitivity to variations in the nature and concentration of the counter ions.

The concentration of the counter ions external to the Stern layer decrease exponentially with the distance from the surface.

Within the diffuse layer, the region which separates the ions associated with the particle from those in the bulk phase is represented by a shear plane, whose value of potential is referred to as the zeta potential Φ_Z. It is a measure of the kinetic stability of a colloidal system and, when sufficiently elevated, can prevent the aggregation of adjacent particles. If it is a low value, no force will prevent flocculation and consequent aggregation. Generally, the kinetic stability occurs with values higher than 30 mV or lower than -30 mV.

Electrical neutrality ultimately exists at an infinite distance from the particle surface.

It has to be noticed that although the discussion has been focused on a flat surface in an electrolyte solution, the concepts are applicable to curved surfaces as well, assuming that the surface is smooth and thus the surface charge is distributed uniformly; such assumptions are certainly valid for spherical particles.

2.2.2 DLVO Theory

The DLVO theory (Derjaguin, Landau, 1937; Verwey, Oberbeek, 1944) is one of the more used theories for the interpretation of the stability of a colloidal system. It states that the stability of a colloidal particle in a suspension depends from its total potential energy, that can be written as a sum of two contributions: the van der Waals attraction (V_A) and the electrostatic repulsion (V_R)[3].

$$V_{TOT} = V_A + V_R \quad [2.1]$$

This theory describes the force between charged surfaces interacting through a liquid medium and combines the effects due to the double layer of counter ions.

In case of small, equal sized spheres and low potentials, the van der Waals attraction is:

$$V_A = -\frac{Aa}{12D} \quad [2.2]$$

where A is the Hamaker constant (typically about 10^{-20}J), a is the radius of the particle and D is the distance between particles.

The electrostatic repulsion, per surface area, is:

$$V_R = 2\pi a\varepsilon\Phi^2 e^{-kD} \quad [2.3]$$

where ε is the solvent permeability, Φ the zeta potential and k a function of the ionic composition.

So, the total potential of a colloidal particle can be written as:

$$V_{TOT} = -\frac{Aa}{12D} + 2\pi a\varepsilon\Phi^2 e^{-kD} \quad [2.4]$$

The Fig. 2.3 shows the van der Waals attraction potential (V_A), the electric repulsion potential (V_R) and the combination of the two opposite potentials as a function of the distance between two surfaces.

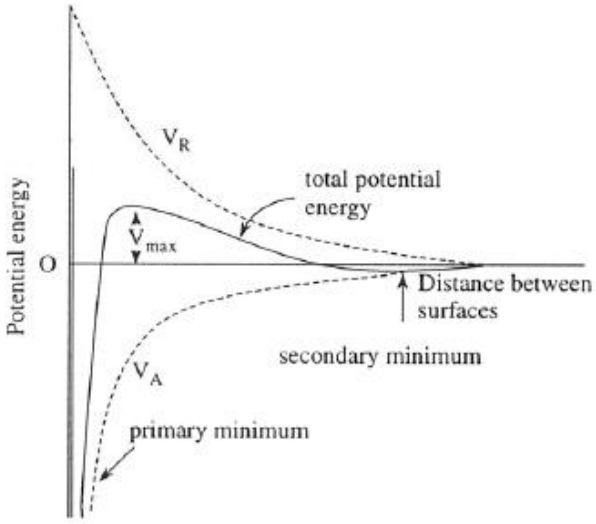

Fig. 2.3 *Schematic representation of DLVO potential.*

An energy barrier, resulting from the repulsive force, prevents two particles from approaching one another and adhering together, but, if the particles collide with sufficient energy to overcome that barrier, the attractive force will pull them into contact and they will adhere strongly and irreversibly together. The primary and secondary minimums are the regions where the aggregation can occur and they are separated by the energy barrier *Vmax*.

Therefore, the system will maintain the kinetic stability only if the particles present a sufficiently high repulsion, to withstand flocculation and consequent coagulation. It should be noted that the repulsion is not directly due to the surface charge on solid particles, instead it is the interaction between two double layers.

To conclude, this theory asserts the importance of the repulsion forces to dominate (to have the kinetic stability in a colloidal system) and mainly two mechanisms can allow to achieve this: the steric stabilization and the electrostatic stabilization.

The first one is a thermodynamic stabilization method that consists in the attachment of polymer layers, which cover the surface of the interacting particles and prevent the contact among them.

The second one is a kinetic stabilization method and is linked to the distribution of the charges in the system.

The DLVO theory has a number of adjustable parameters, like the proper description of van der Waals force, the surface charge density and the surface potentials. Even so, an extended term is often needed to explain the behavior of a system.

In summary, this theory can often describe tendencies, but not quantitatively predict experimental results (without parameter fitting or extended theories).

In principle, it is valid under these conditions:

- dispersion is very dilute, so that the charge density and distribution on each particle surface and the electric potential in the proximity next to each particle surface are not interfered by other particles;
- no other force is present beside van der Waals force and electrostatic potential (gravity is negligible or the particle is significantly small, and there exist no other forces, such as magnetic field);
- geometry of particles is relatively simple, so that the surface properties are the same over the entire particle surface, thus surface charge density and distribution, as well as the electric potential in the surrounding medium, are the same;
- the double layer is purely diffusive, so that the distributions of counter ions and charge determining ions are determined by all three forces: electrostatic force, entropic dispersion and Brownian motion.

2.3 Self-assembly

The process of self-organization of colloidal particles relies on the tendency of components having sizes from the molecular to the macroscopic to spontaneously aggregate and self-assemble into ordered and structurally well-defined arrays.

These arrays can be quite related to the main crystal systems found in metallurgy and mineralogy (e.g. face centered cubic, body centered cubic, etc.), with the fundamental difference lying in the spatial scale of the unit cell (or lattice parameter) of the equilibrium structure in each particular case.

Self-assembly may occur in many different systems at different scales: from angstrom sized elements (atoms forming a crystal) to planets gravitationally arranged in solar systems. Although much of the work has focused on molecular self-assembly (formation of molecular crystals, lipid bilayers, phase separated polymers and self-assembled monolayers, etc.), many of the most interesting applications can be found at larger sizes and represent an available strategy for generating nanostructured materials[4].

Therefore, there are now three ranges of sizes of components for which it is important: molecular, nanoscale (colloids, nanowires, nanospheres and related structures) and meso- to macroscopic (objects with dimensions from microns to centimeters).

As for the colloidal particles crystallization, works from Pusey, Okubo and Nagayama dealt with the problem from different points of view. Okubo centered his studies in colloidal crystals (self-organization of colloidal micro particles in solution)[5]; Pusey studied glass transitions in three dimensional concentrated arrangements of colloidal particles[6], whereas Nagayama centered his efforts in studying two dimensional systems (colloidal self-assembled monolayer)[7].

Self-assembly is important in a range of fields: chemistry, physics, biology, materials science, nanoscience and manufacturing and moreover it has the opportunity to develop through the interchange of concepts and techniques among these fields.

2.3.1 Principles of self-assembly

The success of self-assembly is determined by some peculiar characteristics of the system.

The arrangement is attained without direct external action (typically referring to human intervention) and it is governed by a thermodynamic process that occurs through a balance of attractive and repulsive interactions and move the components in such a way that their final assembled structures exhibit a lower state of energy than the unassembled components. Forces that are taken advantage of underline the key role of weak interactions and include hydrogen bonding, van der Waals and Coulomb interactions, hydrophobic and hydrophilic interactions, acting on a strictly local level.

Therefore, the structure is constituted at the thermodynamic minimum, finding the best combination of interactions between subunits, but not forming covalent bonds between them.

The self-assembly normally is carried out in solution or at an interface to allow the required motion of the components. One challenge lies in assuring the mobility and agitation of the components because, as they become larger than molecules, Brownian motion rapidly

becomes irrelevant and gravity and friction become important; furthermore, the interaction with their environment can strongly influence the course.

The displacement of the particles inside the system can be described by means of the Einstein relation:

$$D = \mu k_B T$$

where: D is the diffusion constant, k_B is Boltzmann's constant, T is the absolute temperature, mobility μ is the ratio of the particle's terminal drift velocity to an applied force, $\mu = v_d / F$.

The thermodynamic properties can be recalled to rationalize another property often found in self-assembled systems: the sensitivity to perturbations exerted by the external environment.

Small fluctuations that alter thermodynamic variables might lead to marked changes in the structure and even compromise it, because the weak nature of interactions is responsible for the flexibility of the architecture and allows for rearrangements of the structure in the direction determined by thermodynamics. If fluctuations bring the thermodynamic variables back to the starting condition, the structure is likely to go back to its initial configuration.

This leads the identification of one more property, which is generally not observed in materials synthesized by other techniques: reversibility (or adjustability). The association either must be reversible or must allow the components to adjust their positions within an aggregate once it has formed. The strength of the bonds between the components, therefore, must be comparable to the forces tending to disrupt them.

In conclusion, the great influence exerted by external parameters in this processes makes certainly the synthesis more problematic, due to the many free parameters that require control, but, on the other hand, it has the exciting advantage that a large variety of shapes and functions on many length scales can be obtained (Fig. 2.4).

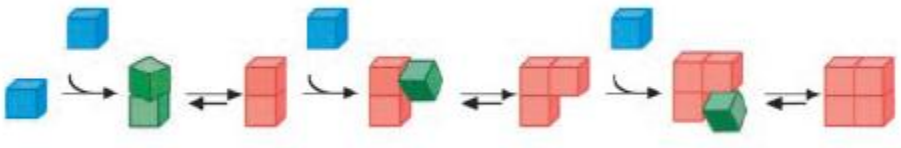

Fig. 2.4 *Components that can equilibrate, or adjust their positions once in contact, can form ordered crystals, if the ordered form is the lowest-energy form (shown in red).*

2.3.2 Applications of self assembled structures

The challenges for the future about nanofabrication and pattern at the nanoscale by self-assembly are numerous and concern many different areas of the material science[8].

To cite some example: in the medical area, new drug delivery agents and selective targeting strategies to diagnostic purposes, in electronics, the formulation of new nanoscale devices, then, the synthesis of new solid-state battery nanomaterials, of efficient, cheap and robust solar cells, of enhanced activity photo catalytic nanomaterials, of super lattice nanostructures and new power generation systems.

This strategy provides a way of assembling electrically or optically functional components, like optical gratings, sensors, anti-reflection coatings and microlens arrays for improving the extraction efficiency of LEDS.

The exploiting of the high porosity and large contact areas has been useful for gas sensors and catalysis applications, while the morphology of these systems and possibility to structure the surface with a fine degree of control has led to the use as super hydrophilic or super hydrophobic surfaces[9] (Fig. 2.5).

(a) *(b)* *(c)*

Fig. 2.5 *Optical diffraction grating (a), gas sensor (b), super hydrophobic to super hydrophilic structures (c).*

In the photonic research field, self-assembled nanostructures essentially comprise photonic crystals and glasses and the peculiar way in which they interact with light makes them promising for exploring novel optical performances, as parts of photonic integrated circuits, efficient light emitters (such as lasers) or in obtaining more efficient light sources of thermal emission.

2.4 Self-assembled photonic crystals

The use of self assembly process in photonics has steadily increased in the past twenty years with novel material techniques for the fabrication of photonic crystals[9].

In the mid-nineties, 3D structures based on self-assembled colloidal beads (artificial opals) were firstly used by Astratov et al.[10] as a natural method to obtain 3D PhCs in the optical range.

2.4.1 Building blocks

In these self-assembly processes, monodisperse, submicrometer, colloidal particles (e.g. polymer or silica microspheres) are used as building blocks to obtain photonic crystals.

The monodisperse particles most extensively used are the spherical ones, because their interactions are more isotropic and stacking is easier, but in some cases also particles with non spherical symmetry are considered, because they are interesting for the possibility to get packing structures with lower filling fraction, in contrast to the spherical particles which tend to crystallize in high density packing.

Even restricting the survey to the spherical shape, it is possible to find different approaches, such as homogeneous particles or composite particles (Core-Shell).

A large number of materials have been investigated, since they offer different functionalities and processing possibilities.

This includes organic and inorganic materials, and among them, oxides, chalcogenides and metals.

The organic spheres more spread in the opal preparation are polymers, mainly polystyrene (PS) and polymethylmethacrylate (PMMA), but also monodispersed carbon spheres have been used. The inorganic spheres withstand higher temperatures and have chemical properties very different from those of organic ones. Among the oxides, the SiO_2 spheres are very popular and are mainly produced by the Stöber method[11], while TiO_2 and ZnO spheres are interesting for their high refractive index and photonic properties. Among the chalcogenides, can be mentioned spherical metal sulphides like ZnS, CdS and ZnSe and, among the metals, gold and silver spheres.

2.4.2 Methods of preparation

Several methods have been proposed to realize optimal 3D structures with photonic crystal properties, starting from SiO_2 or polymer (mainly PS or PMMA) spheres[9].

The first method proposed was gravital sedimentation of SiO_2 spheres in diluted aqueous colloidal suspensions. This sedimentation procedure leads to easy fabrication of thick colloidal crystal films, typically with thicknesses of the order of a millimeter, under careful aging conditions. Due to the multiple domains, they tend to be mechanically fragile. However, sedimented samples often show weak Bragg reflection, because the microparticles adopt a polycrystalline structure with several point and line defects.

Alternatives to the natural sedimentation method were proposed to deal with larger spheres (up to 1 micrometer) based on electrophoresis or physical confinement by sonication, where the effects of gravity were minimized. Here, the imposed geometry of the cell forces the spheres to accommodate to a given fixed thickness and the fabrication of films with a large domain of several cm^2 within a few days is enabled.

The nowadays most widely used method is the vertical deposition (or convective deposition)[12], which is based on the gentle evaporation of the liquid (generally ethanol or water) forcing the spheres to arrange in the meniscus formed between a vertical substrate, the colloid suspension and air. This method can produce single crystals that contain defect densities that are significantly lower than in sedimented opals and provides precise control over the thickness with superior crystalline quality of the structures, even for diameters larger than 1 micrometer, if dealing with polymer beads.

Typically, a large single crystal size is pursued, with controlled orientation, reachable in the shortest times and with good mechanical properties.

From a technological viewpoint, however, there still remain some serious disadvantages; for example, the film thickness varies from the edge to the center, due to the changes in suspension concentration during solvent evaporation.

A different route to control solvent evaporation is to vertically lift the substrate with a given velocity using a step-motor; the concentration of particles is essentially constant during the film formation and the thickness is relatively uniform (Fig. 2.6).

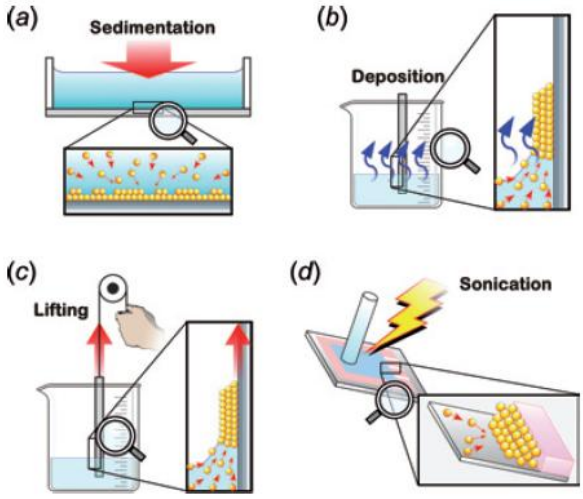

Fig. 2.6 *Illustrations of various procedures for fabricating colloidal crystal structures (adapted from[13]).*

Other methods are based on the Langmuir-Blodget technique and transfer monolayers formed in the air/liquid interface to a substrate, forming 2D or even 3D patterns by layer-by-layer procedure, although the optical quality of the structures formed in this way might be improved.

In the aim of a future large-scale production of SiO_2 colloidal photonic crystals, a new method based on spin coating has been recently developed. In fact, it allows the growth of planar artificial opals on large surfaces (wafer size) in a rapid way, although the crystalline (optical) quality of these structures is lower than samples obtained by vertical deposition.

In summary, a number of different techniques have been developed over the last few years to obtain self-assembled structures for photonic applications (Tab. 2.1); which of them is the most appropriate will depend on the particular use.

Type	Thickness	Area	Time	Optical Quality	Issues
Sedimentation[127]	mm	mm^2	weeks	poor	fragile, material waste
Cell confinement[130]	few to tens of monolayers	mm^2	1–2 days	good	opening the cell
Vertical Deposition[132]	1 to tens of monolayers	mm^2	1–2 days	excellent	large beads plummet
Langmuir-Blodgett[146]	1 to several monolayers	dm^2	hours	poor	sequential
Shear induced[158]	mm	dm^2	minutes	poor	polycrystaline, high amount needed
Motor drawing[142]	1 to tens of monolayers	mm^2	hours	good	high concentrations needed
Air-water interface[153]	few to tens of monolayers	mm^2	minutes	fair	indetermined orientation, substrate detached
Spin-Coating[154]	1 to tens of monolayers	wafer size	minutes	fair	polycrystalline
Wedge-Cell[145]	1 monolayer	cm^2	hours	excellent	only 2D

Tab. 2.1 *Summary of self-assembly techniques to obtain self-assembled structures for photonic applications (adapted from[9]).*

The vertical deposition method provides the highest optical quality and therefore it should be chosen when fundamental optical properties are going to be studied or exploited. In the experimental part of this work we will focus on this method which is also, to date, the most widely used one to produce photonic crystals templates.

2.4.2.1 Vertical deposition

The implementation of this method relies on the meniscus of the solvent to drive a flux of colloidal particles that, under the right conditions, will spontaneously assemble into ordered structures. In the laboratory, the general procedure involves placing a nearly vertical substrate in a suspension of colloidal spheres.

If we first consider the formation of a monolayer, liquid interface induces partially immersed spheres to close pack, then the liquid evaporating from the spheres brings in more liquid and the liquid flow brings in more spheres, so that at the end an ordered monolayer develops[14].

Evaporation on the surface of the meniscus causes dramatic flows of fluid and spheres, spheres get sucked into place by the flow, unlikely that structure forms in thermodynamic equilibrium, but, overall, the deposition of an ordered three-dimensional packing of more or less uniform thickness on the substrate predominates, starting from a position below the initial level of the contact line at the top of the meniscus.

After the opaline film is dried, the spheres adhere well enough to each other, and to the substrate, so that the film can be handled (or even re-immersed in solvent) without detaching or disintegrating easily (Fig. 2.7).

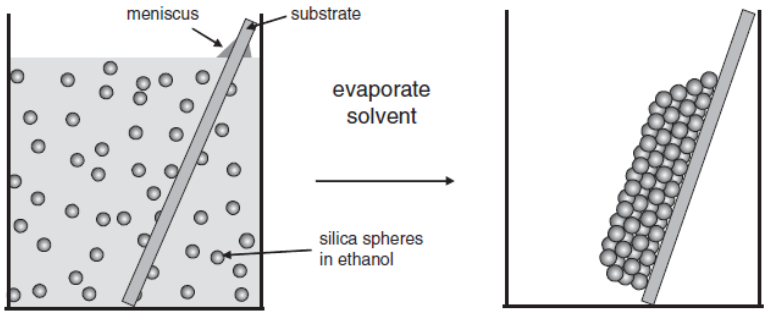

Fig. 2.7 *Opaline films can be formed by slow evaporation of a suspension of colloidal microspheres by vertical deposition (adapted from[14]).*

Crystal thickness, starting from one layer, increases monotonically with time as solvent evaporates, until an equilibrium thickness is reached. It is strongly dependent on the

concentration of colloid suspension and is determined by the meniscus properties which, in turn, depend on:

- temperature;
- rate of evaporation (ambient humidity and vapor pressure);
- surface tension of the liquid;
- concentration of the colloid.

Recently, various attempts have dealt with improving crystal quality by modifying key parameters such as evaporation rate, pressure and temperature. As an example, by applying negative pressure (vacuum) the density of defects can be reduced obtaining, in a particular case, large crack-free single crystal domains up to 1 mm^2 for polystyrene spheres of 300–400 nm[9].

Oscillatory thicknesses can also be appreciated on those regimes of growth, attributed to temporal variations of the evaporation velocity and caused by periodic changes of the friction force at the meniscus.

There are two possible crystal structures, the Hexagonal Close Packed (HCP) and the Face Centered Cubic (FCC), for hexagonal sheets of spheres to stack, both having the same packing volume (74%) at zero temperature (Fig. 2.8). Also can have random (e.g. ABACBCAC…) or random hexagonal close-packed (RHCP) stackings.

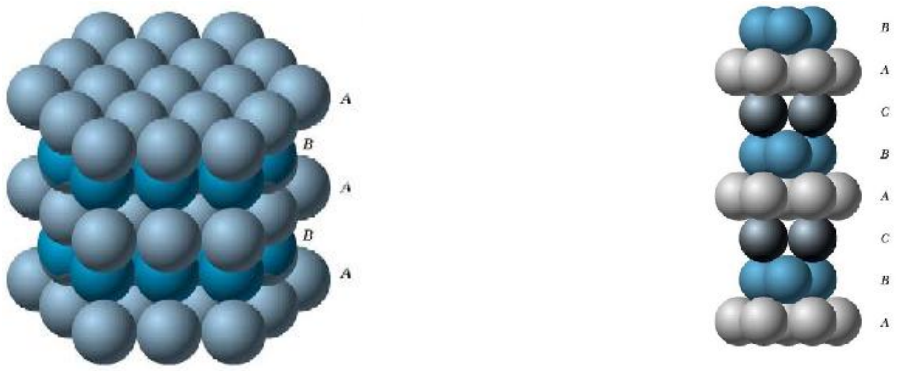

(a) *(b)*

Fig. 2.8 *Schematic representation of HCP (a) and FCC (b) arrangement of spheres.*

Woodcock theoretically demonstrated that when hard spheres self-assemble in thermo dynamical equilibrium, the FCC is slightly more stable than the HCP[15]. In fact, considering the thermodynamics, FCC is slightly lower in free energy, even if the energy difference is small (~10^{-3} kBT).

Most natural opals are RHCP, although in some cases FCC is observed, while opals sedimented over months have a preference for FCC[16]. The stability of FCC is well suited to the natural sedimentation method used in the early trials of self-assembling PhCs. However, the same arrangement has been found in systems well separated from equilibrium (like those obtained by vertical convective deposition) suggesting a different mechanism.

The reason can be that the true equilibrium structure of hard-sphere crystal is FCC, but that the difference in free energies (per particle) of FCC and HCP hard-sphere crystals are the same within an uncertainty of no more than $2x10^{-3}$ kBT. Thus, long-lived non-equilibrium states are easily achieved.

To summarize, thermodynamics favors FCC slightly, natural opals are typically random RHCP, synthetic opals with quick sedimentation are random RHCP, synthetic opals with slow sedimentation are FCC.

An hypothesis concerning the flow-driven placement of spheres has tried to explain the preference for the FCC crystal structure, assuming that the crystal structure in convective assembly is controlled mainly by the solvent flow[14]. Briefly, when sheets of hexagonally packed spheres are stacked, octahedral and tetrahedral interstitial sites are created inside the structure, through which the liquid is flowed, referring as *clear* (octacoordinate pore-body) and *obstructed* (tetracoordinate pore-body) niches.

Flow through the pore-space network is controlled by the pore-throats and into the clear niches is 33% higher than into the obstructed niches. If each subsequent layer of spheres were to lodge exclusively at the clear niches, because the flow rate into them is higher, FCC packing would result (ABCABC stacking is obtained) as a consequence of the particles to preferentially lodge at one set of niches (Fig. 2.9). According to this hypothesis, a more efficient draining succeed in determining the final orientation.

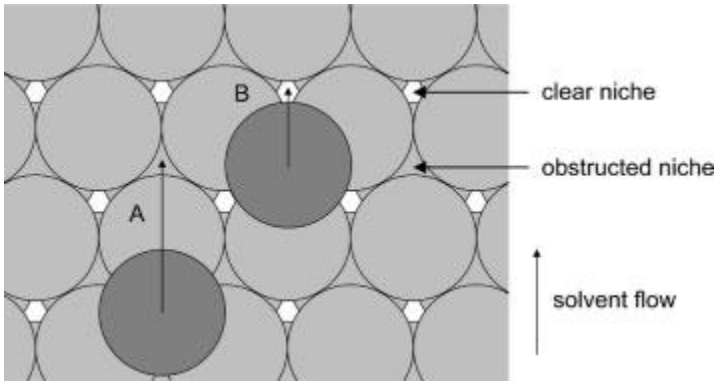

Fig. 2.9 *Hypothesis explaining the role of solvent flow in the formation of opals (adapted from[14]).*

This configuration can be described by saying that it corresponds to an FCC lattice with its [111] axis perpendicular to the substrate and that its (111) planes (compact hexagonal arrangements) having one of their rows of spheres vertical (perpendicular rather than parallel to the meniscus).

2.5 Sol-gel process

The sol-gel process is a low temperature and high-purity synthesis route that is particularly suitable for the deposition of thin films from a liquid phase[17].

The synthesis of solid materials by means of the "soft chemistry" has been developed in the last 30 years and these kind of synthesis can include reactions of "wet chemistry" and sol-gel chemistry, based on inorganic polymerization of molecular precursors. The precursors are mixed at a molecular level and multicomponent materials can be formed at temperatures lower than what is possible with the traditional methods of preparation. Metastable phases can be prepared, that stay kinetically stable until sufficiently high temperatures.

The sol-gel approach is adaptable to producing glasses and ceramics without powders, and films and fibers as well as bulk pieces[18]. In glasses production, for example, the sol-gel method permits preparation at far lower temperatures than by using conventional melting and it also makes possible synthesis of compositions that are difficult to obtain by conventional means because of problems associated with volatilization, high melting temperatures, or crystallization.

The sol-gel process, as the name implies, involves the evolution of inorganic networks through the formation of a colloidal suspension of solid particles in a liquid (*sol*) by means of hydrolysis and condensation, followed by the gelation of the sol to form a network in a continuous liquid phase (*gel*).

The precursors for synthesizing these colloids consist usually of a metal or metalloid element surrounded by various reactive ligands, defined as metal alkoxides $M(OR)_z$ (where "R" is an alchilic group like methyl or ethyl). Their extended use can be attributed to the fact that most of them are soluble in many organic solvents and react rapidly with water, and the final product obtainable presents a high homogeneity. The starting material is processed to form a dispersible oxide and forms a sol in contact with water or dilute acid. Removal of the liquid from the sol yields the gel, and the sol/gel transition controls the particle size and shape. The gel is a continued solid phase, with sub micrometric porosity, characterized of chains of

average length superior of 1 μm, and it can be dried or consolidate by the application of thermal treatments.

The reactions involved can be described as follows, and conduct to the formation of a network of oxides.

$$M\text{-}OR + H_2O \rightarrow M\text{-}OH + ROH \text{ (hydrolysis)}$$

$$M\text{-}OR + RO\text{-}M \rightarrow M\text{-}O\text{-}M + ROH \text{ (condensation)}$$

In case of silicon precursors, the reactions are:

$$Si - OR + H_2O \rightarrow Si - OH + ROH \text{ (hydrolysis)} \quad [2.5]$$

$$Si - OR + RO - Si \rightarrow Si - O - Si + ROH \text{ (condensation)} \quad [2.6]$$

$$\downarrow$$

$$Si(OR)_4 + 2H_2O \rightarrow SiO_2 + 4ROH \quad [2.7]$$

The most studied example is silicon tetraethoxide (or tetraethyl orthosilicate, TEOS, with the formula $Si(OC_2H_5)_4$). Its hydrolysis reaction is an example of a sol-gel process: it easily converts into silicon dioxide with ethanol as side product.

Sol-gel method permits the synthesis of a big variety of shapes of the same material, according to the way in which the solvent is eliminated. The high versatility of the technique has allowed a wide diffusion in different fields of applications.

In Fig. 2.10 a scheme synthesizes the route of obtaining different products from a solution containing the precursor.

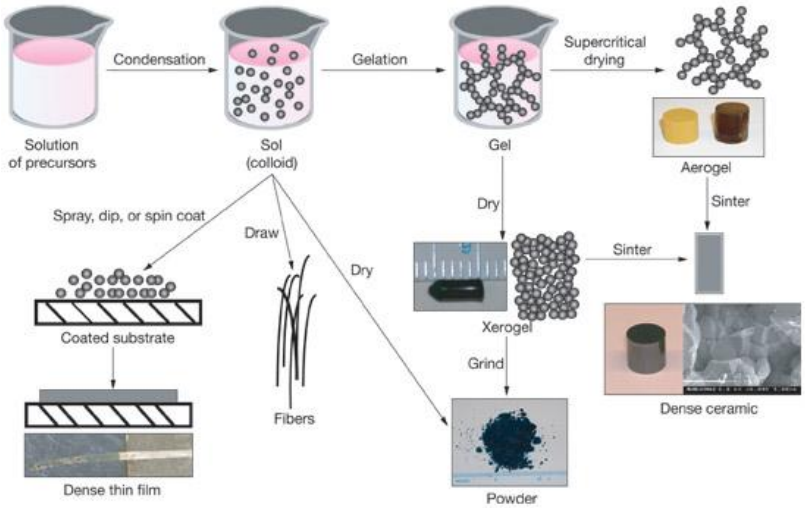

Fig. 2.10 *Scheme of the variety of the products that can be obtained by sol-gel technique.*

Sol-gel method is very popular and is widely employed to prepare oxide materials, multicomponent ceramics and nanophasic materials.

The soft chemistry approach of sol-gel has known a renewed interest because of the recent boom of nano-science. In fact, sol-gel processing has emerged as one of the most interesting routes to bottom-up preparation of nanomaterials, nanoparticles and surface functionalization of nano-structures.

Two main different approaches to sol-gel nanochemistry can be envisaged. In the first one, sol-gel reactions are used to obtain interconnected structures through polycondensation of the precursors, which is the typical bottom-up route for thin and ultra-thin film preparation. In the second one, the final material is obtained through an intermediate step by using sol-gel chemistry for the synthesis of nano-objects, such as nanoparticles or nano-building blocks.

Sol-gel chemistry can be, however, also combined with more sophisticated nano-synthesis techniques to get ordered and hierarchical structures; template of different dimensions can give hierarchical porous materials.

2.5.1 Hydrolysis

Metal alkoxides are popular precursors because they react readily with water and their hydrolysis reaction can occur in an acid or basic environment.

The reaction is called hydrolysis and occurs by a nucleophilic substitution mechanism involving a nucleophilic addition followed by proton transfer from the attacking molecule (H_2O) to the alkoxide, and a removal of the protonated species as alcohol or water.

The mechanism is synthesized here, in case of silicon alkoxides:

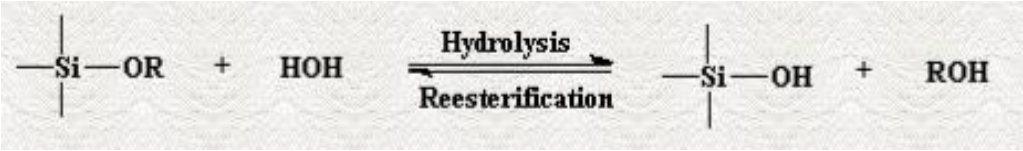

The parameters that govern this reaction are: the nature of the substituent R linked to the silicon, the molar ratio between H_2O/alkoxyde, the concentration of the solution, the ratio between H_2O/silicon, the presence of a catalyst, the pH, the temperature. If the substituents are bulkier, they have a retarding effect on the hydrolysis reaction.

In many cases, the alkoxydes precursors are immiscible in water (like tetraethoxysilane TEOS, for example), so there is the need for introducing an alcoholic solvent to homogenize the solution. The alcohol enters in the kinetic environment as a product, so can influence the equilibrium of the reaction.

Normally, the kinetics of the reaction in a neutral environment is very slow, and, under most conditions, condensation commences before hydrolysis is complete.

An acid or basic catalyst is frequently introduced to increase the reaction rate.

In Fig. 2.11 is represented the hydrolysis rate of TEOS as a function of the pH and can be noticed that the minimum is in correspondence of a pH=7, and then, in acidic or basic environment, the rate is increased.

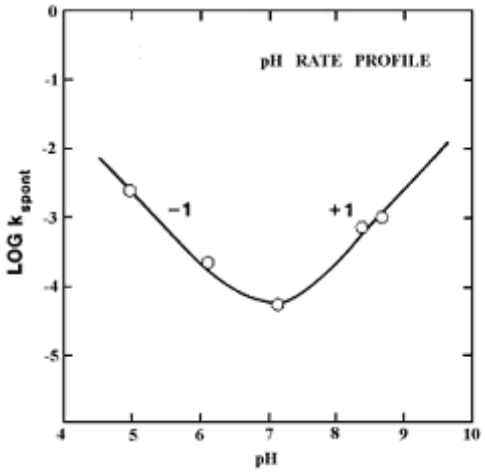

Fig. 2.11 *Hydrolysis rate as a function of the pH of the solution (adapted from[17]).*

As mentioned, acid or basic catalyst can be used to increase the hydrolysis rate. Examples of the acid catalysts are HCl, HNO_3, H_2SO_4, HF and, among the basic, NH_4OH, NaOH and n-Bu4NF, NaF, DMAP (dimethylaminopyridine) which behave as Lewis bases. HCl and NH_4OH are most generally used.

In the acid catalysis, it is likely that an alkoxide group is protonated in a rapid first step.

The oxygen of the alkoxy molecule is protonated from the H^+ introduced by the acid, resulting in an increase of the electrophilicity of the silicon center, which in turn becomes more susceptible toward attack by the nucleophilic species (water molecules).

This results in the formation of a penta-coordinate transition state with significant S_N2-type character.

Under these conditions, the hydrolysis is favored both by small electron-donating substitutes (R) which can better stabilize the positive charges present during the reaction intermediate formation.

The mechanism of the acid catalysis is schematized in Fig. 2.12:

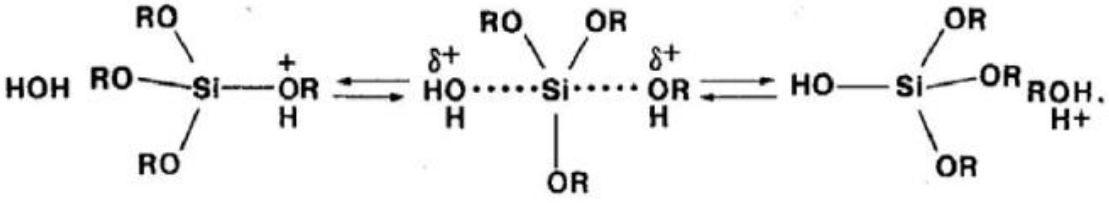

Fig. 2.12 *Hydrolysis mechanism of alkoxysilanes in acidic environment.*

The mechanism induced by the different acids behavior is the same, but it has been observed that the rate and extent of the hydrolysis reaction is most influenced by the strength and concentration of the catalyst; while all strong acids behave similarly, weaker acids (more elevated pH) require longer reaction times to achieve the same extent of reaction.

From a plot of the logarithm of the hydrolysis rate constant versus acid concentration, a slope of one was obtained and this explains that the reaction is first-order in acid concentration.

In the basic catalysis, in a rapid first step water dissociates to produce hydroxyl anions. The hydroxyl anion then attacks the silicon atom. The partially negative charged substituents reduce the silicon electrical density, stabilizing a negative intermediate phase and favoring the hydrolysis. Again, it is the case of an S_N2-type mechanism, in which the -OH displaces -OR with inversion of the silicon tetrahedron.

Once an initial hydrolysis has occurred, following reactions proceed stepwise, with each subsequent alkoxide group more easily removed from the monomer then the previous one, due to the fact that more highly hydrolyzed silicones are good electron acceptors species.

The scheme in Fig. 2.13 reports the mechanism of the basic catalysis:

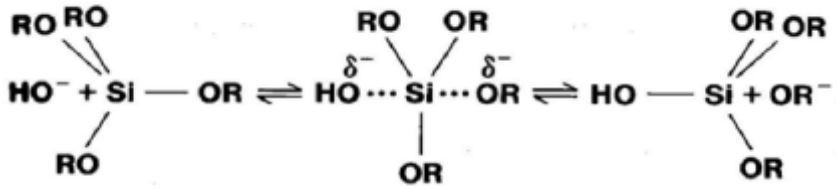

Fig. 2.13 *Hydrolysis mechanism of alkoxysilanes in basic environments.*

Under basic conditions, the hydrolysis reaction was found to be first-order in base concentration. Base-catalyzed hydrolysis of silicon alkoxides proceeds much more slowly than acid-catalyzed hydrolysis at an equivalent catalyst concentration, but it still tends to be complete and irreversible.

Depending on the amount of water and catalyst present, hydrolysis may go to completion (so that all of the OR groups are replaced by OH), or stop while the metal is only partially hydrolyzed, $Si(OR)_{4-n}(OH)_n$.

2.5.2 Condensation

In the condensation phase, the silanol species produced during hydrolysis reactions tend to polymerize with formation of Si-O-Si bonds.

Two different condensation mechanisms can develop: a silanol group attacking directly a silicon atom and provoking the subsequent expulsion of a water molecule, or attack with the removal of an alcohol molecule in case of a partially hydrolyzed monomer[17]:

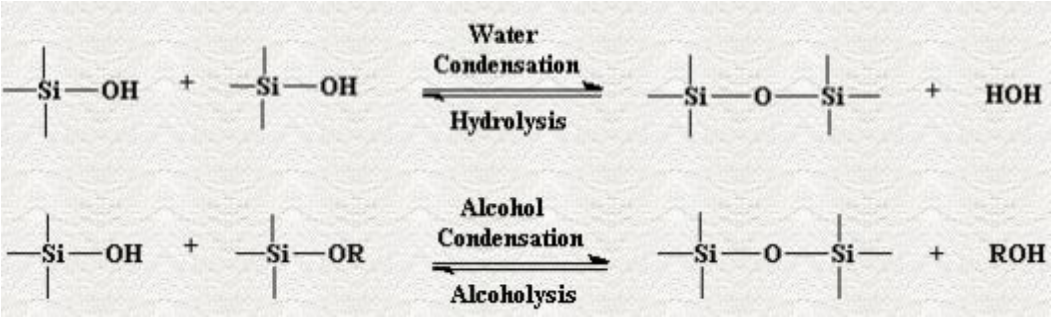

As for the hydrolysis reaction, the condensation can occur to the formation of inorganic networks without the presence of a catalyst, but this presence will serve to increase the reaction yield.

Numerous catalysts have been employed; mineral acids, ammonia, alkali metal hydroxides, and fluoride anions are the most commonly used.

The overall condensation rate is minimized at about pH=1.5-2, that corresponds to the isoelectric point of silica, while surface silanol groups are protonated and deprotonated at lower and higher pH values, respectively.

Silanols become more acidic with the extent of condensation of the siloxane network; the isoelectric point of polymers leading to gelation is lower than the one for the condensation of monomers and this is presumably due to the increasing acidity of silanols with the degree of condensation.

Polycondensation reaction results in a dramatic increase in the viscosity of the solution, and gelation results from the formation of an oxide- or alcohol- bridged network (the *gel*).

Considering the role of the catalysts, *condensation reactions in acidic environment* involves protonated silanol groups, which provides the silicon atoms with a more electrophilic character, thus exposing them to nucleophilic attack.

The groups that are more suitable for protonation are obviously the basic ones that is the silanol groups contained in monomers or oligomers with lower ramifications; condensation reactions may occur preferentially between neutral species and protonated silanols situated on monomers or at the end group of chains.

Therefore the substitution of alkoxy groups (electron-donors) with -OH and -SiO groups (electron-acceptors) tends to destabilize the formation of positive charges in the transition state, resulting in a slowdown of the condensation kinetics.

The general mechanism contemplates the formation of penta- or hexacoordinated silicon intermediates or transition states.

The commonly accepted mechanism for the *condensation in basic environment* includes the nucleophilic attack of a deprotonated silanol toward a neutral silicon atom.

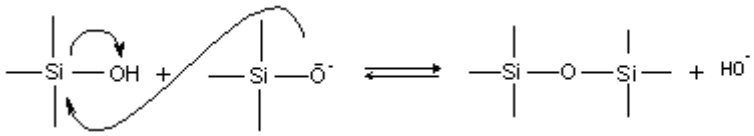

The reaction occurs above the isoelectric point of silanol groups, therefore depending on the polymerization degree.

The acidity of a silanol depends on the other substituent on the silicon atom. When basic OR and OH are replaced with O-Si, the reduced electron density on Si increases the acidity of the protons on the remaining silanols.

Therefore, one of the proposed mechanisms favors reaction between larger, more highly condensed species, which contain acidic silanols, and smaller, less weakly branched species.

The maximum condensation rate occurs at neutral pH (significant concentration of both protonated and deprotonated silanols), while the minimum condensation rate is observed at the isoelectric point.

The general mechanism contemplates the formation of penta- or hexacoordinated silicon intermediates or transition states.

The presence of deprotonated silanol groups in the growing species creates a mutual repulsion between them, favoring the monomer addiction to this growing specie more than the condensation between oligomeric chains.

In summary:

- the *acidic environment* favors the hydrolysis reaction, the condensation therefore slows down and proceeds thanks to reaction of neutral species with protonated Si-OH groups, leading to less ramifications in the polymer chains;
- in *basic environment* hydrolysis reaction has a slow course and speeds up with the increase of silanol group's concentration, while the condensation stage is faster and proceeds through addition of monomers to Si-O groups of the growing clusters. The resulting network is characterized by spherical oligomers and by a highly interconnected network. Condensation rate is higher in basic conditions, as deprotonated M-OR groups are more reactive nucleophiles.

2.5.3 Gelification

In the gelification phase, the transition between the *sol* and the *gel* takes place.

Cluster grow by condensation of polymer until the cluster collide, then links start to form between the clusters to produce a continuous solid network called *gel*.

The growth of the polymer chains continues with time, due to condensation and aggregation effects, progressively increasing the connections to the network and the stiffness of the gel and causing a volume contraction of the structure.

To identify the gel point, the sudden change in rheological behavior is generally used. The time of gelation, t_{gel}, is sometimes defined as corresponding to a certain value of viscosity, or, alternatively, as the point where the gel shows a determined of elasticity to be cut. However, the difficulties to compare different system using this parameter have led to other methods, which measure the viscoelastic behavior of the gel as a function of the shear rate.

Generally, the time of gelification is decreased by factors that increase the condensation rate. Other factors that contribute to its reduction are the increase in temperature, in the concentration of alkoxyde, in the water/alkoxide ratio and the decrease in the size of the alkoxy group. For gels made from silicon alkoxydes, gelation is much faster in the presence of a base or HF than of other acids.

The properties of a gel continue to change long after the gelation time, because the reactions that produce gelation continue, due to the presence of a substantial fraction of oligomers that are still free to diffuse and react.

The succeeding phase of the process is called *aging* and results in a substantial structural reorganization and contraction of the network, including the expulsion of the solvent and of

the liquid phase from the pores, the reduction of the interfacial area liquid/solid, and the formation of additional cross-links that solidify the network.

The final matrix structure results in a network of interconnected long linear chains in case of acidic catalysis and in an assembly of bulkier spherical domains with higher ramification degree in case of basic catalysis (Fig. 2.14).

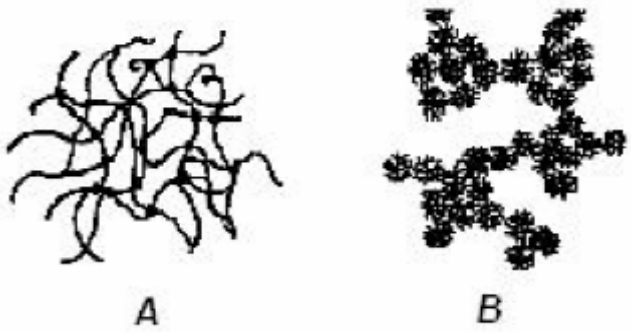

Fig. 2.14 *Chain structure of a gel obtained after condensation in acidic (A) or basic (B) environment.*

2.5.4 Drying

The gel phase is constituted of a continue solid phase, still containing a liquid phase; the drying process is needed to remove this liquid phase, with evaporation at room temperature.

The drying of the gel can be divided into different stages.

At first the gel network shrinks by an amount equal to the volume of liquid that evaporates, due to the capillary tension, and the liquid-vapor interface remains at the exterior surface of the body. Here the network is compliant, the tension in the liquid is low and the radius of the meniscus is larger than the pore radius.

The second stage begins when the body becomes increasingly stiff, the tension in the liquid rises and the radius decreases.

At the critical point, the radius of the meniscus becomes equal to the radius of the pores in the gel and the tension is maxima. Beyond that point, the meniscus recedes into the pores, leaving air-filled pores near the surface. Even as air invades the pores, a continuous liquid film supports flow to the exterior, so evaporation continues to occur from the surface of the body.

Eventually, the liquid becomes isolated into pockets and drying can proceed only by evaporation of the liquid within the body and diffusion of the vapor to the outside.

During this drying phase, the removal of the liquid contracts the gel and increases the matrix stiffness that progressively opposes to the deformation forces.

This tension state can give origin to cracks and can irreversibly damage the structure. It is more relevant for the gel prepared in acid catalysis than for gel prepared in basic catalysis, due to the minor dimensions of the pores.
Some methods exist to reduce this state of tension; among them, a slower drying to release the tensions, a more prolonged aging to create a solid network or the use of chemical additives to have a controlled drying.
The final product of the drying still contains some water, in the form of residual hydroxide groups, so a thermal treatment is needed for a further consolidation.

2.6 Infiltration of opal structures

The processing of the structures fabricated by self-assembly is concerned with various issues, but here the choice is to focus on the infiltration.

2.6.1 Conventional template infiltration

In the last few years, many works have developed opal-composites of a large variety of materials, mainly with the aim of using the opal as a template to obtain the inverse opal structure and increase the refractive index contrast or introduce active elements.
Different techniques have been employed to grow materials within the pores of the opaline structures. According to whether the material is only infiltrated, having been prepared earlier, or it is grown (synthesized) inside the structure, they can be divided into two categories: *physical infiltration* or *chemical infiltration*.
The colloidal crystal template is then selectively removed (by chemical etching or thermal decomposition) to yield an inverse porous structure (Fig. 2.15-a).
In *physical infiltration*, materials must be in the form of nanoparticles suspensions or molecular solutions, since they must be smaller than the pores of the template they are meant to impregnate. The usual ways are: by dipping the porous structure directly into the solution containing the material to be infiltrated, by dip-coating or by spin-coating[19-20].
In the dip-coating, for example, with the aim of infiltrating the voids in the self-assembled PS templates, the substrate covered by the template is lowered into the precursor solution and withdrawn at a low speed, while the silica sol penetrates the voids of the PS colloidal crystal by capillary forces.

In *chemical infiltration*, the chemicals are transported to the reaction site, but often the access port decreases in size as the reaction proceeds, putting a limit to what thickness can be grown. Wet chemistry methods firstly employed include: chemical bath deposition, sol-gel or electrodeposition, while gas based methods such as chemical vapor deposition (CVD) or atomic layer deposition (ALD) more recently employed have provided very conformal layers around the spheres, of controllable thickness and good homogeneity[21-22].

Many works in literature exist about the fabrication via a colloidal/sol-gel route, in which sol-gel solutions have been used as matrix precursors for the synthesis of porous oxide materials, such as SiO_2, TiO_2 and Al_2O_3.

However, cracking tends to occur upon drying both at the colloidal assembly stage and at the infiltration stage due to a combination of dehydration and/or polymerization-induced contraction and associated local capillary forces.

Moreover, an excessive infiltration in the second fabrication step results in over layers formation, whereas incomplete or no conformal deposition often leads to structural collapse during template removal in the third step.

2.6.2 Evaporative co-assembly in one single step

To avoid the need for liquid infiltration into a preassembled porous structure, an innovative single step process has been implemented to yield a colloidal composite by means of the evaporative co-assembly of a sacrificial colloidal template with a matrix material[23].

It combines the steps of template self-assembly with matrix infiltration into one single step process in which colloids are allowed to assemble directly from the sol-gel solution, to yield robust inverse opal films with no over layer, very large ordered domains and few cracks, due to the "gluing" action of the sol-gel matrix (Fig. 2.15-b).

The approach relies on polymer colloids (PS or PMMA) assembling in a broad range of sol-gel precursor solution ($M(OH)_4$), (where M=Si, Ti, Ge) through an evaporative deposition, to form a large area, defect-free composite opal film.

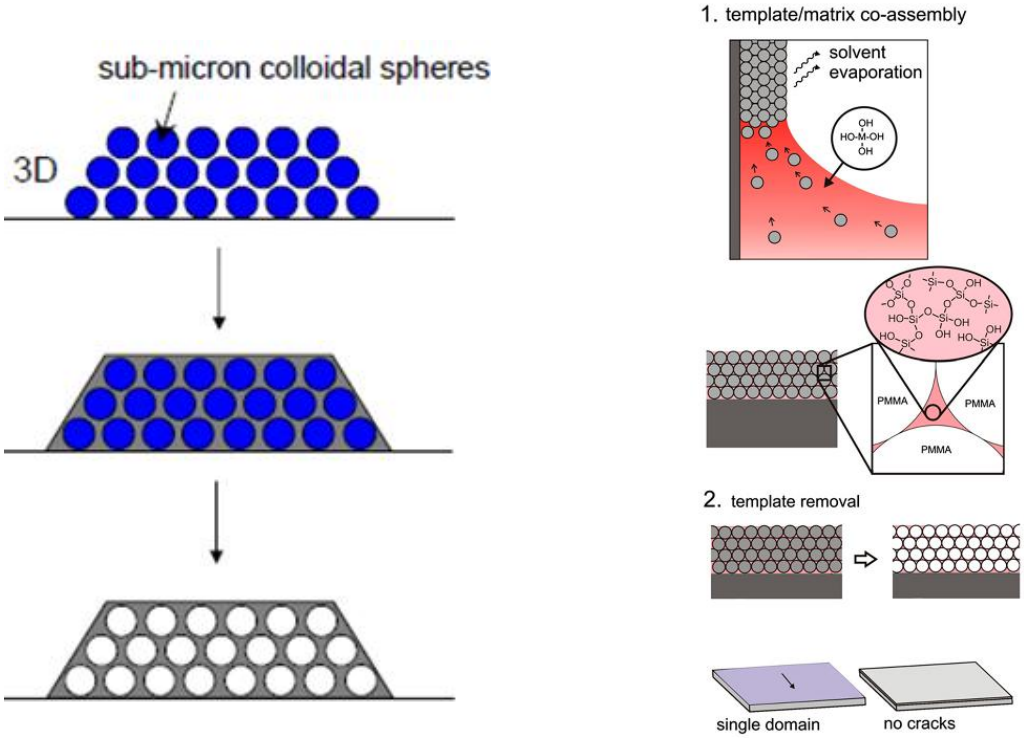

(a) *(b)*

Fig. 2.15 *Schematics of "conventional" colloidal template self-assembly (a), and co-assembly of colloids with a soluble matrix precursor (b), for the synthesis of inverse opal thin films (adapted from[23]).*

The resulting structure contains silica gel matrix material distributed uniformly in the interstitial spaces of the polymeric opal film and, upon firing, yields a high-quality inverse opal silica structure (I-SiO_2).

The advantages of this new approach can be summarized in: great reduction in the defect population (e.g. crack density), growth of large, highly ordered domains, prevention of over layer formation and non uniform infiltration, ability to form multilayered, hierarchical, patterned and curved film structures.

The sol-gel matrix that undergoes polycondensation at the time of colloidal assembly provides a glue/necking to the assembling spheres, so that the thin-walled interconnected silicate network can operate to inhibit the formation and propagation of cracks.

Moreover, the formation of a colloidal crystal and the associated interfaces between the polymerizing sol-gel solution and the assembling colloidal spheres may provide sites for the relaxation of tensile stresses encountered during the gelation process and the controlled release of the solvent during the polycondensation reaction can also occur at these interfaces and be channeled through the interconnected porous network to evaporate at the surface.

2.6.2.1 Applications of the co-assembly method

The co-assembly method enables the versatile fabrication of good quality inverse opal layers for a possible wide variety of applications, also in structures not practically attainable by conventional methods. Representative examples are shown in Fig. 2.16.

Multilayer inverse opal structures with varying pore sizes can be created by the successive deposition of template/matrix composite layers (Fig. 2.16-A). Such structures could have important applications in differential drug release, where sequential dosed release of components can be achieved by selective pore size engineering.

The exceptional ordering in this co-assembly process can be utilized for depositing inverse opal films onto topologically patterned substrates, suited for micro fluidics, optical and photonic devices, or sensors (Fig. 2.16-B).

Finally, co-assembly can be used to deposit inverse opals onto arbitrarily shaped substrates, such as curved surfaces, and such high-surface area could have important applications for catalysis and biomedical surfaces (Fig. 2.16-C).

These single-domain periodic inverse opal films can also behave as large-area photonic band gap structures for applications in photonics[24-25].

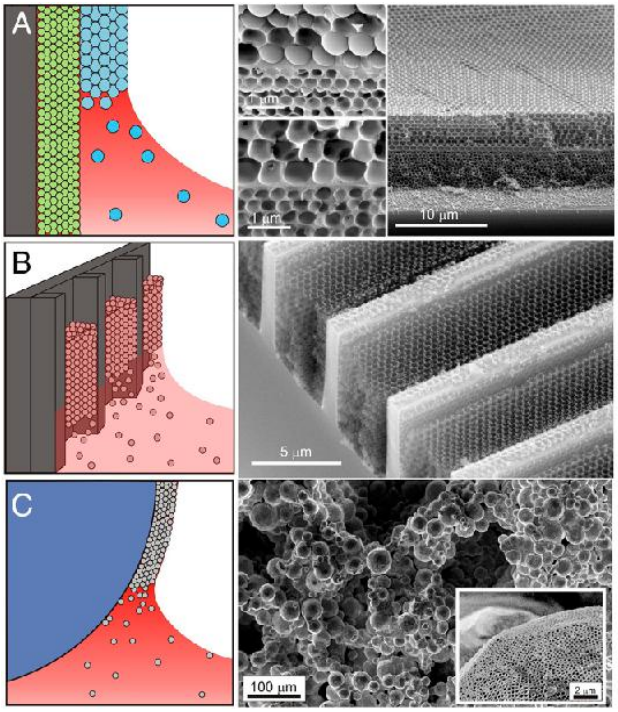

Fig. 2.16 *Novel SiO_2 inverse opal structures enabled by colloidal co-assembly. Schematics of the processes are shown on the left and the representative SEM images are shown on the right (adapted from[23]).*

References

1 Zhang, J., Li, Y., Zhang, X. & Yang, B. *Colloidal Self-Assembly Meets Nanofabrication: From Two-Dimensional Colloidal Crystals to Nanostructure Arrays*, Advanced Materials, 22, 38 (2010) 4249-4269.

2 Moon, J. H., Ford, J. & Yang, S. *Fabricating three-dimensional polymeric photonic structures by multi-beam interference lithography*, Polymers for Advanced Technologies, 17, 2 (2006) 83-93.

3 <http://www.kemi.kth.se/nuchem/colloid/mj_070420.pdf>.

4 Whitesides, G. M. & Boncheva, M. *Beyond molecules: self-assembly of mesoscopic and macroscopic components*, Proceedings of the National Academy of Sciences of the United States of America, 99, 8 (2002) 4769-4774.

5 Okubo, T. *Giant Colloidal Single Crystals of Polystyrene and Silica Spheres in Deionized Suspension*, Langmuir, 10, 6 (1994) 1695-1702.

6 Gasser, U., Weeks, E. R., Schofield, A., Pusey, P. N. & Weitz, D. A. *Real-Space Imaging of Nucleation and Growth in Colloidal Crystallization*, Science, 292, 5515 (2001) 258-262.

7 Dushkin, C. D., Nagayama, K., Miwa, T. & Kralchevsky, P. A. *Colored Multilayers from Transparent Submicrometer Spheres*, Langmuir, 9, 12 (1993) 3695-3701.

8 Ozin, G. A. *et al. Nanofabrication by self-assembly*, Materials Today, 12, 5 (2009) 12-23.

9 Galisteo-López, J. F., Ibisate, M., Sapienza, R., Froufe-Pérez, L. S., Blanco, Á. & López, C. *Self-Assembled Photonic Structures*, Advanced Materials, 23, 1 (2011) 30-69.

10 Astratov, V. N. *et al. Optical spectroscopy of opal matrices with CdS embedded in its pores: Quantum confinement and photonic band gap effects.*, Nuovo Cimento Della Societa Italiana Di Fisica D-Condensed Matter Atomic Molecular and Chemical Physics Fluids Plasmas Biophysics, 17, 11-12 (1995) 1349-1354.

11 Stöber, W., Fink, A. & Bohn, E. *Controlled growth of monodisperse silica spheres in the micron size range*, Journal of Colloid and Interface Science, 26, 1 (1968) 62-69.

12 Jiang, P., Bertone, J. F., Hwang, K. S. & Colvin, V. L. *Single-Crystal Colloidal Multilayers of Controlled Thickness*, Chemistry of Materials, 11, 8 (1999) 2132-2140.

13 Furumi, S., Fudouzi, H. & Sawada, T. *Self-organized colloidal crystals for photonics and laser applications*, Laser & Photonics Reviews, 4, 2 (2010) 205-220.

14 Norris, D. J., Arlinghaus, E. G., Meng, L., Heiny, R. & Scriven, L. E. *Opaline Photonic Crystals: How Does Self-Assembly Work?*, Advanced Materials, 16, 16 (2004) 1393-1399.

15 Woodcock, L. V. *Entropy Difference Between the Face-Centered-Cubic and Hexagonal Close-Packed Crystal-Structures*, Nature, 385, 6612 (1997) 141-143.

16 Pusey, P. N., van Megen, W., Bartlett, P., Ackerson, B. J., Rarity, J. G. & Underwood, S. M. *Structure of crystals of hard colloidal spheres*, Phys Rev Lett, 63, 25 (1989) 2753.

17 Brinker C.J., S. G. W. *Sol-Gel Science: The Physics and Chemistry of Sol-Gel Processing* (Academic Press, Inc., 1990).

18 Livage, J. *Sol-gel processes*, Current Opinion in Solid State and Materials Science, 2, 2 (1997) 132-138.

19 Velev, O. D. & Lenhoff, A. M. *Colloidal crystals as templates for porous materials*, Current Opinion in Colloid & Interface Science, 5, 1-2 (2000) 56-63.

20 Zhao, X. S. *et al. Templating methods for preparation of porous structures*, Journal of Materials Chemistry, 16, 7 (2006) 637-648.

21 Juárez, B. H., García, P. D., Golmayo, D., Blanco, A. & López, C. *ZnO Inverse Opals by Chemical Vapor Deposition*, Advanced Materials, 17, 22 (2005) 2761-2765.

22 Rugge, A., Becker, J. S., Gordon, R. G. & Tolbert, S. H. *Tungsten Nitride Inverse Opals by Atomic Layer Deposition*, Nano Letters, 3, 9 (2003) 1293-1297.

23 Hatton, B., Mishchenko, L., Davis, S., Sandhage, K. H. & Aizenberg, J. *Assembly of large-area, highly ordered, crack-free inverse opal films*, Proceedings of the National Academy of Sciences, 107, 23 (2010) 10354-10359.

24 Arsenault, A. C. *et al. From colour fingerprinting to the control of photoluminescence in elastic photonic crystals*, Nature Materials, 5, 3 (2006) 179-184.

25 Blanco, A. *et al. Large-scale synthesis of a silicon photonic crystal with a complete three-dimensional bandgap near 1.5 micrometres*, Nature, 405, 6785 (2000) 437-440.

Chapter 3

Rare Earth doping of photonic crystals

3.1 Introduction

The developing of light sources and electronic devices which detect and control light with high efficiency is strategic in the fields of telecommunications and optoelectronics.

The range of wavelengths of main interest for the Long Wavelength Band of telecommunications (Third Window, 1510-1600 nm) is centered in 1.54 µm, because it is the region in which the combined losses in silica fibers due to Rayleigh scattering, to hydroxyl absorption and to absorption caused by to the vibration of silicon-oxygen bonds are at a minimum (Fig. 3.1). The trivalent erbium ion has an optical transition that is responsible for a strong emission around 1.54 µm and corresponds to the transition from the first excited state ($^4I_{13/2}$) to the ground state (Fig. 3.2); the overlap of its high luminescence intensity in a low attenuation region has generated increasing interest in the doping with erbium to produce efficient optical sources.

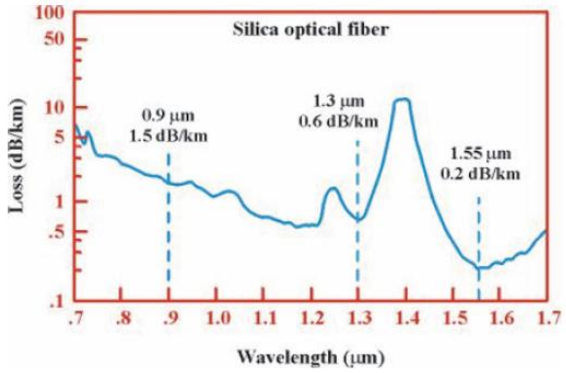

Fig. 3.1 *Scheme of the losses in optical fibers based on silica; the three windows with the minimum of losses are reported: 0.9 µm, 1.3 µm and 1.5 µm (adapted from[1]).*

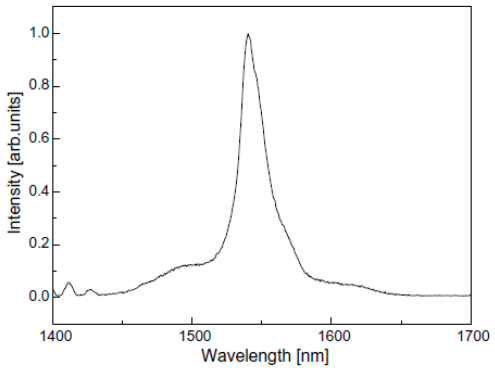

Fig. 3.2 *Photoluminescence spectrum of $^4I_{13/2} \rightarrow {}^4I_{15/2}$ transition of the Er^{3+} ion, upon excitation at 514.5 nm, showing the main emission at 1.54 µm (adapted from[2]).*

The requirement to operate at these wavelengths for full compatibility with fiber optic communications systems has led to intense work on different Er-doped matrices (based on silica) as host.

Erbium-doped glasses or crystals can be used as optical amplification media, erbium-doped optical fibers perform the gain medium in long-distance links and doped 3D photonic band gap materials can represent a new class of resonant nonlinear materials in which the threshold for nonlinear response is considerably lower than in all conventional photonic materials.

3.2 Theoretical principles

3.2.1 Rare earths: Erbium and Ytterbium

Rare earths (lanthanides) are a group of 14 elements with the common characteristic of having the 4f orbital partially filled: their electronic configuration is $4f^N5s^25p^66s^2$ (with N= number between 1 and 14).

All lanthanides show basically the same behavior and the same magnetic and optical properties; except for Ce and Eu, they have a unique oxidation state (+3). The reason is that the 4f orbitals are internal orbitals and therefore difficult to ionize.

Their optical properties have been observed for the first time in 1907 by J. Becquerel: these ions show very close emissions if inserted into a solid matrix, having the typical width of atomic transitions, involving the sublevels of the 4f shell.

Energy levels in RE ions are conventionally labeled according to their angular momentum and spin quantum numbers using term symbols such as $^4I_{13/2}$ or $^2F_{7/2}$. Here, the letters refer to the total orbital angular momentum of the ion obtained by combining the orbital angular momenta of the individual electrons, the left superscript is the number of possible orientations of the total spin of the ion and the right superscript gives the total angular momentum of the ion.

It is important to clarify the difference between the concepts of radiative transitions and non-radiative transitions between energy levels; a radiative transition occurs for the absorption or emission of the light, which can occur between levels with relevant difference in energy; a non-radiative transition is the result of the energy transformation involved in the electronic excitation of vibrational or rotational energy, which always occurs between very near energetic levels.

- **Erbium**

Erbium (Er) is a chemical element in the lanthanide series, having the electronic configuration $[Xe]4f^{12}6s^2$. It is widely used in the form of the trivalent ion Er^{3+} , formed by the loss of one electron from the 4f orbital and two electrons from the 6s orbital. It is interesting to the photonic community because it is responsible of a strong radiative emission in the near infrared around 1.54 μm.

Erbium radiative transitions in solid hosts resemble those of the free ion, so in Fig. 3.3 the energy level structure of the free erbium ion is reported, with the more common transitions.

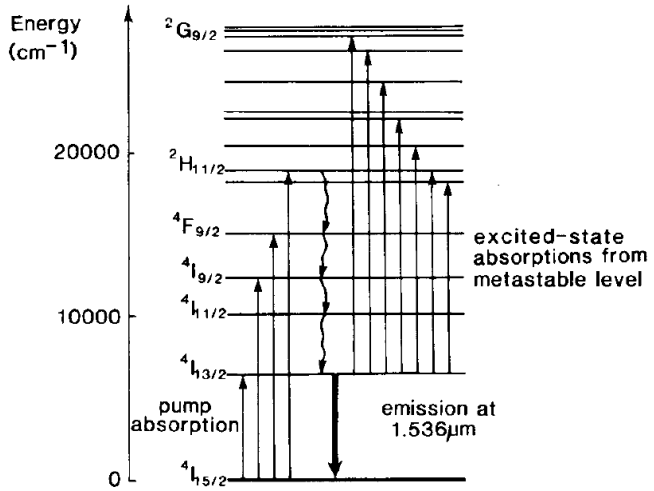

Fig. 3.3 *Energy level structure of the trivalent erbium ion, and some common optical transitions (adapted from[3]).*

The transition from the first excited state ($^4I_{13/2}$) to the fundamental state ($^4I_{15/2}$) results in the emission of a photon of wavelength 1.54 μm; the lifetime of the $^4I_{13/2}$ state is long (up to 14 ms in an amorphous silica host) and hence this is often referred to as the metastable state.

Absorption bands around 1480 nm, 980 nm, 810 nm and 520 nm correspond to transitions from the ground state to the top of the $^4I_{13/2,}$ $^4I_{11/2,}$ $^4I_{9/2}$ and $^4S_{3/2}$ manifolds, respectively.

Other radiative transitions that yield luminescence in the visible region exist, but these are of little importance for telecommunications applications.

Er ions are used as optical probes since it has several advantages over dyes, showing a narrower emission line width. Nevertheless, a significant excitation density of the erbium ions is required, and erbium lasers typically exhibit a high threshold pump power.

Moreover, the absorption cross sections are relatively small and the doping concentration is limited by the need to avoid excessive quenching processes (in which the reduction or

limitation of an excited-state population occur, mostly by undesired effects, e.g. "concentration quenching", for high concentrations of dopants, often associated with upconversion effects).

A common method to solve this problem is co-doping with ytterbium (Yb^{3+}) sensitizer ions.

- **Ytterbium**

Ytterbium (Yb) is a chemical element in the lanthanide series, having the electronic configuration $[Xe]4f^{14}6s^2$. It has acquired a prominent role in the form of the trivalent ion Yb^{3+}, which is used as a laser-active doping in a variety of host materials, including both crystals and glasses.

In Fig. 3.4 is reported the energy level structure of the free ytterbium ion.

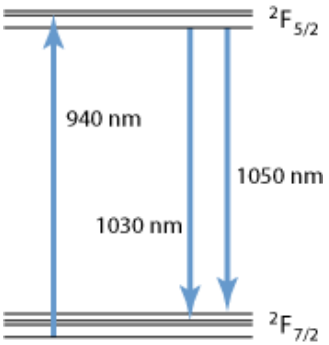

Fig. 3.4 *Energy levels of Yb^{3+} ions in Yb:YAG and the usual laser transitions (adapted from[4]).*

The electronic level structure is very simple, with only one excited state manifold ($^2F_{5/2}$) from the ground-state manifold ($^2F_{7/2}$).

Energy transfers between ions of different species are often exploited in lasers and amplifiers. Even though the erbium ions could directly absorb radiation in the near IR range (e.g. at 980 nm), this absorption is very weak, so the ytterbium ions are often used as sensitizers to increase the efficiency of pumping.

Ytterbium offers the advantage of a good spectral overlap (resonance) of its $^2F_{5/2}$ emission level with the erbium $^4I_{11/2}$ absorption (980 nm) and of a higher absorption cross-section (~25 times)[5], leading to an efficient energy transfer from ytterbium to erbium (Fig. 3.5).

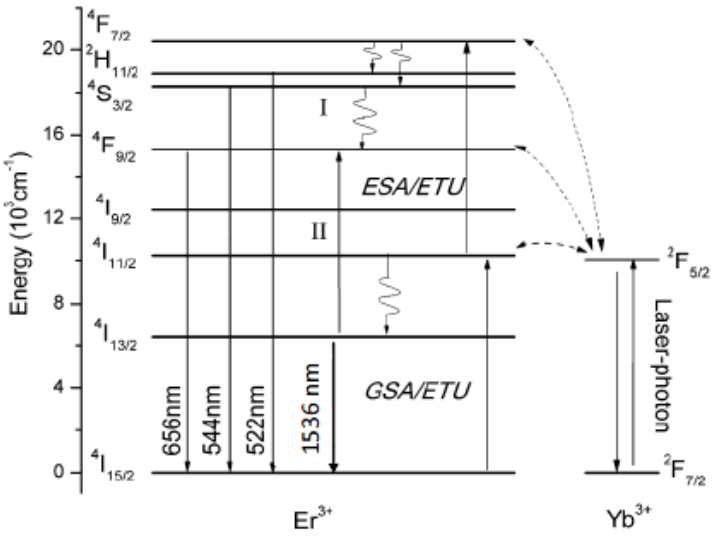

Fig. 3.5 *Simplified energy level diagram of Er^{3+} and Yb^{3+} ions.*

Solid straight lines with upward and down arrows denote pumping and upconversion transitions, and radiation transitions; dot lines and wavy arrows denote energy transfer and non-radiative relaxation; GSA, ESA and ETU are the acronyms for the ground state absorption, excited state absorption and energy transfer upconversion, respectively (adapted from[6]).

For example, the ytterbium ions can efficiently absorb pump radiation at 980 nm, and then transfer the energy to erbium ions in the ground-state manifold, making them promoted to the excited level $^4I_{11/2}$ with higher energy.

From that level, the ions are quickly transferred by non-radiative relaxations into the laser level $^4I_{13/2}$, almost fully suppressing any energy transfer back to ytterbium.

The $^4I_{13/2}$ level of erbium is properly the responsible for the 1.54 μm emission.

3.2.2 Mechanisms of energy transfer

In materials containing rare earths (RE) species, a number of different interactions may occur: between the incident photon and the ions and among the ions themselves.

In the first, the most important are the multistep excitation, due to classical *excited state absorption (ESA)* and the *upconversion fluorescence;* in the second, the most important are the *cooperative upconversion*, either between two ions or between a pair of ions and a third one, the *energy transfer upconversion (ETU)*, due to the fact that in many RE-doped solids ions may be connected energetically by energy transfer diffusion, and the *cross relaxation*[7].

A peculiar characteristic of the RE ions is their tendency for ion-ion interactions[8]. This study is based on the fact that, when the concentration of active ions is increased, a migration of energy between the centers is found. In addition, RE ions are prone to aggregation in solid hosts and, beyond a critical concentration, ions cluster together to form aggregates which increase the probability of these ion-ion interactions, reducing luminescence efficiencies and lifetimes. These can either be between ions of the same rare earth (as in the case of clustered material) or between different ions (as in the sensitization of one RE ion by another).

Ion-ion interactions due to multipolar interactions between neighboring RE ions have been treated for the first time in detail by Förster[9] and Dexter[10], whose model labeled two nearby ions as donor (D) and acceptor (A), respectively. The donor is that ion that is in the excited state and the acceptor is that ion that is initially unexcited.

- **Energy Transfer**

Energy transfer occurs in a system when absorption and emission do not take place within the same center. It can occur between laser ions of the same species (energy migration) or different species.

Considering the energy migration between two nearby erbium ions, an ion in the metastable state can interact with a ground state ion, promoting it to the $^4I_{13}/_2$ level (Fig. 3.6).

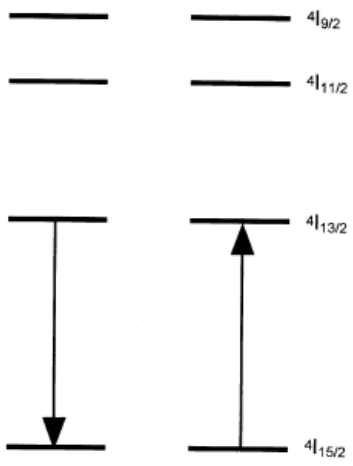

Fig. 3.6 *Energy migration between Er ions (adapted from[8]).*

Although radiative emission may still occur from the second ion, the probability of non-radiative decay is increased with each successive transfer, and hence this constitutes a loss mechanism. In a gain medium, for example, when the excitation energy is transported via energy transfer between laser ions of the same species, the laser efficiency can be affected

both in positive and negative ways: the efficiency may be increased, but it can also be severely reduced when the excitation energy is transported to crystal defects where non-radiative decay occurs.

In the other case, when the excitation energy is transported between laser ions of different species, energy migration usually facilitates energy transfer to other ions (Fig. 3.7).

(a) *(b)*

Fig. 3.7 *Energy transfer between ions of the same species (a) and between ions of different species: Yb^{3+} to Er^{3+} (b) (adapted from[11]).*

The dominant mechanism behind this is usually the dipole–dipole resonant interaction (*Förster energy transfer*) between closely located ions. As the strength of the dipole–dipole interaction rapidly vanishes with increasing distance between the ions (with the inverse sixth power of distance), it depends strongly on the doping concentration, on the size of the crystal's unit cell and also on the tendency of ions to form clusters.

In summary, in this thesis work, the objective of the co-doping with erbium and ytterbium is the occurrence of energy transfer from Yb^{3+} ions to Er^{3+} ions, to increase the luminescence efficiency of the Er^{3+} ion by a coupling, by means of resonant levels, to the absorption bands of the Yb^{3+} codopant.

It is usual to recur to co-doping inside materials where it is necessary to improve the absorbance efficiency, because it is quite difficult for the Er^{3+} to obtain an efficient transition between the levels $^4I_{15/2}$ e $^4I_{11/2}$. This is due to a limitation in the concentration of dopants, to avoid the phenomena of concentration extinction, which manifest themselves by the reduction in decay lifetimes, associated to every energetic level, and loss of photoluminescence intensity. Introducing a second rare-earth dopant can also provide the added inhibition of aggregation of the emitting species through the formation of a solvation shell.

The occurrence of simultaneously upconversion phenomena is not desirable because the aim is the exploitation of the emission of erbium located in the near IR, since it would result in an effective reduction of the main transition efficiency of the excited material.

3.3 Doping of 3D photonic crystal structures

3.3.1 Reasons for the doping

The functionalization of photonic bandgap materials with luminescent emitters is of particular interest, since in this case their structure can affect not only the incident but also the emitted light.

In fact, they represent a mean for localizing and trapping light in all spatial directions and, simultaneously, an approach for the complete inhibition of spontaneous emission, over a broad frequency range.

The spontaneous emission rate of an atom is not only a property of the atom, but also depends on the density of states (DOS), a property determined by the atom's dielectric environment.

The local density of states (LDOS) for photons, in these materials, exhibits considerable variation from point to point in coordinate space and reveals large spectral gaps even in the absence of a PBG in the total density of states, if properly designed (Fig. 3.8).

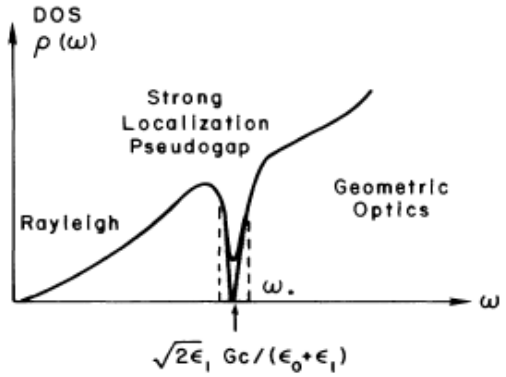

Fig. 3.8 *Photon density of states exhibiting low-frequency Rayleigh scattering and high-frequency geometric-optics extended states separated by a pseudogap of strongly localized photons (adapted from[12]).*

The inhibition and enhancement of the emission are due to the low photon density of states at the stop band and high density of states at the band edge, respectively.

It is possible to engineer an arbitrary number of individual localized states which may interact weakly with each other inside the material, in order to obtain a more robust trapping of light than the resonance in conventional microcavity modes.

If the emitter atom has a radiative transition in or near the PBG the decay of emitted light can be slowed down or completely inhibited in the ideal case of a complete photonic band gap.

Moreover, scattering of emitted light that propagates through the photonic crystal can change in an angle-dependent manner and parameters, such as lifetime, or in an angle-independent way, such as total emitted power. These properties allow tuning of the emission spectrum, directionality of emission and rate of emission[13].

For these reasons, are these gaps in the LDOS that control the nature of radiative dynamics and that may lead to novel effects in quantum and nonlinear optics[14].

Quantum optical features are properly related to the drastic alteration of the photon DOS.

Then, nonlinear wave propagation effects in the form of ultrashort solitary wave pulses can still occur, as a result of their large group velocity dispersion near a photonic band edge and complex symmetries, while linear wave propagation is absent inside the gap.

There have been experimental reports on the effects of the photonic structure with an incomplete photonic stop band on the rate of spontaneous emission of photoluminescent guests, such as fluorescent organic dyes[15] and quantum dots[16]. However, there are several disadvantages, such as the broad emission bands of these emitters (especially as for the organic dyes), which always leads a partial matching between the photonic band gap and the emission bands.

To measure the larger inhibition effect of the PBG on the spontaneous emission rate, conditions requests are the presence of a complete PBG joined to efficient emitters.

As seen in Chapter 1, to achieve a complete PBG in a 3D crystal, it is required a high-enough index contrast (>2.9); the focus on inverse opal structures is expected to be an ideal geometry; the mesoscale of voids and the ordered structure of the dielectric mean can lead to a correspondent periodic arrangement of emitter compounds inside the matrix, with the luminescent centers embedded into the matrix or grafted onto the pore walls.

The choice of lanthanide ions as emitters allows higher efficiency, due to narrower spontaneous emission linewidths, with high quantum yields and longer lifetimes[17].

Until now, few reports exist about photoluminescence properties of lanthanide ions embedded in an inverse opal matrix (SiO_2, TiO_2, ZnO) and the need is still to develop appropriate systems to optimize the effect.

The most qualified idea in this sense relies on the exploitation of the Er^{3+} emission at 1.54 μm to fit well with the calculated PBG of a silicon inverse opal[18].

The 1.54 μm Er emission energy is smaller than the Si band-edge energy and therefore, the Si host does not absorb the Er emission.

It can be noticed that the effects on spontaneous emission, in these photonic crystals with relatively high index contrast, are mostly determined by medium- and short-range order in the crystal. Thus, large-scale disorder should not be considered a major problem in studies on modified spontaneous emission.

3.3.2 Doping techniques

The doping of inverse opal structures has to retain the photonic band properties of the material, so an uneven distribution of the infiltrated luminescent material must be avoided, since otherwise it would result in a broad distribution of effective pore diameters or even a clogging of the macro pores.

RE ions can be embedded in inverse opal matrices either by using *physical* or *chemical infiltration* methods.

3.3.2.1 Physical methods

The physical methods are based on wet chemistry and contemplate the insertion of the doping ions in the precursor solution used for the infiltration of the direct opal. They represent the most common way because the ions can be introduced in optically active state, even if some practical solubility limits exist.

In principle, the advantage stays in the assumption that the whole photonic material (matrix) will be composed of luminescent material and not only the inner surfaces.

- **Dip-coating**

3D inverse opal photonic crystals, doped with erbium and ytterbium have been prepared by means of an infiltration via sol-gel dip-coating, with a SiO_2 sol doped solution by the addition of precursors for the erbium and ytterbium such as chlorides or nitrates[2,19].

High chemical purity can be achieved by this method, but some disadvantages stay in the presence of inhomogeneities in the infiltration, due to the difficulty in penetrating the whole template structure in deep.

The tendency is that the solution succeeds to infiltrate solely the first layers of the template, with the consequent localization of the doping elements only in certain areas of the sample. Moreover, the presence of defects in the film quality can be attributed to the dipping mechanism.

- **Nanocrystals**

A PMMA template structure has been infiltrated with a colloidal solution consisting of prehydrolyzed tetramethoxysilane (TMOS) in methanol and luminescent rare earth doped lanthanum phosphate ($LaPO_4$) nanocrystals[20]. The resulting inverse opal structure is composed of 70 wt% of nanocrystals and 30 wt% of silicon dioxide, working as a binder (Fig. 3.9).

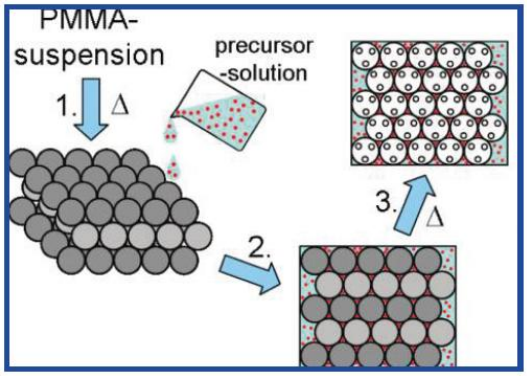

Fig. 3.9 *Illustration of the preparation method of inverse opal structures infiltrated with a solution of doped nanocrystals (adapted from[20]).*

Another example is given of induction of cubic phase α-$NaYF_4$:Yb^{3+}/Er^{3+} nanocrystals to self-assemble in polystyrene (PS) colloidal crystal hierarchical arrays, to obtain, after removing the PS colloidal template, highly ordered 3D inverse opal PCs consisting of densely packed cubic or hexagonal Er doped nanocrystals.

Because of their small size and high colloidal solubility, the nanocrystals are able to completely penetrate the void space of the template structure. The crystal lattice provides a rigid and well-defined environment for the dopant ions, which is not affected by the preparation of the inverse opal.

3.3.2.2 Chemical methods

The chemical methods are mainly based on reactions in the vapor phase and deposition of the active ions once the inverse matrix has already been obtained.

These non-equilibrium methods can help somehow to increase the concentration of erbium ions incorporated but, even so, also in highly doped materials only a small fraction of them is optically active[21]. In all cases, in fact, they have a tendency to aggregate together at high concentrations to form optically inactive clusters. For these reasons, it results that only a thin layer of luminescent material can be applied to the inner surfaces of the macro pores that,

depending on the absorption cross section of the luminescent material, can result in poor absorption of the excitation light.

To cite an example, the functionalization with rare earth complexes of the cavities in a silica inverted opal has been reported in the gas phase loading procedure reported by[22], in which metallorganic complexes with fluorinated ligands are sublimated into the silica inverse opals (previously fabricated) and converted into rare earth nanofluorides and oxifluorides within the cavities of the matrix.

The conversion can lead to strongly associated particles within the cavities, forming agglomerates, in case of rapid heating, while, in case of a slow heating, a loss of the deposited complexes can occur, due to their volatility.

In this case, sublimation of the complexes, in contrast with solution infiltration, allows obtaining a complete filling of the pores and a structure with good optical properties and loading levels.

3.4 Applications: towards a RE photonic laser

3.4.1 Introduction

The wide applicability and versatility of rare earths for lasers arise from several attractive spectroscopic properties. Stimulated emission has been observed from three divalent and nine trivalent lanthanide ions, in various hosts, at wavelengths in the visible and infrared. It has also been observed in lasers operating pulsed and continuously, and in lasers ranging in size from thin films or small fibers (for applications in integrated optics) to large, high-power glass lasers for controlled fusion experiments[23].

They are extensively used for optically-pumped solid-state lasers in the visible and near-infrared since they possess a large number of excited states suitable for optical pumping and subsequent decay to metastable states, having high quantum efficiencies and narrow f→f emission lines.

3.4.2 Laser principle

The word laser means “light amplification by stimulated emission of radiation” and it can be described as an optical amplifier placed inside a resonant optical cavity, in which a gain medium amplifies the beam by the process of stimulated emission.

An electron in an excited state may follow two types of emission processes (Fig. 3.10).

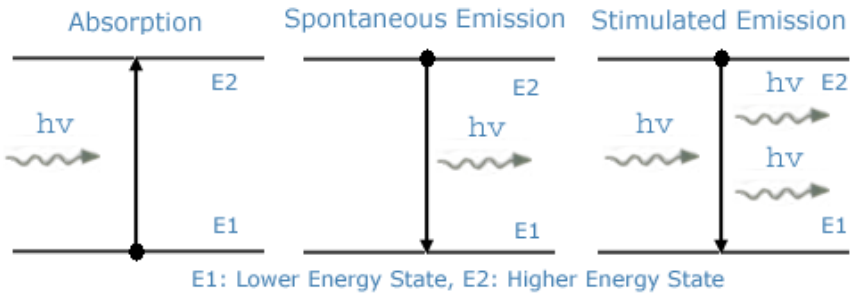

Fig. 3.10 *Absorption, spontaneous and stimulated emission.*

Absorption from the electronic ground level E_1 to an excited state E_2 takes place when photons of adequate energy E_2-E_1=hν are present. Afterwards, the electron in the excited state may undergo two paths of radiative decay, namely spontaneous or stimulated emission. Spontaneous emission is a process where the electron undergoes the transition to a state of lower energy by itself. In the stimulated emission process a photon of adequate energy stimulates the transition of the electron in the energy state E_2 to the lower energy level E_1. The electric field of the stimulating electron couples with that of the excited electron and causes the emission of a photon the same frequency and direction as the incoming photon; they are in phase.

To obtain stimulated emission between two energy levels, a population inversion is necessary. The gain medium absorbs pump energy, which raises some electrons into higher energy quantum states (excited); when the number of particles in one excited state exceeds the number of particles in some lower-energy state, population inversion is achieved and the amount of stimulated emission due to light that passes through is larger than the amount of absorption; hence, the light is amplified.

The resonator typically consists of two mirrors, between which a coherent beam of light travels in both directions, reflecting back on it so that an average photon will pass through the gain medium repeatedly before it is emitted from the output aperture or lost to diffraction or absorption. If the gain (amplification) in the medium is larger than the resonator losses, then the power of the recirculating light can rise exponentially.

Lasers have some outstanding properties which make them to unique light sources, including a small beam divergence, line width (monochromatic, coherence), high intensity output and the possibility of generating short duration pulses. To this day, thousands of laser transitions are known within a range covering the infrared up to X-ray radiation.

The development of new, more powerful lasers goes in parallel with the requirements of evolving technologies; a topical example is given by the optoelectronics field.

3.4.3 Photonic-based laser radiation sources

In general, the laser feedback from photonic materials infiltrated with fluorescent emitters can be rationalized by two mechanisms: one is *photonic crystal lasing* and the other is *random lasing*[24].

3.4.3.1 Photonic lasing

In the idea of a photonic crystal laser, the lasing regime is strongly associated with the lattice periodicity, defined by the distances between crystalline planes, and it is due to optical feedback originating from multiple reflections in these periodic structures.

It is a requisite for this PhC lasing to enhance refractive index contrast, to make the photonic crystal simultaneously confine light and provide optical gain.

Even if the laser emission lines are produced within the approximate range of high-reflectance spectral region associated with photonic stop band, their wavelength is not fixed to the corresponding Bragg wavelength of the periodic structure, but is tunable within the photonic stop band[13]. On the other hand, the lasing wavelength does not necessarily coincide spectrally with the peak PL intensity. Generally, lasing occurs at wavelengths that appear to be correlated to both the stop band reflectivity and the PL bands.

Using this photonic band gap effect, the research activity addresses to the realization of a **low-threshold nanolaser**, in the perspective to realize a laser in which the threshold is reduced a lot ("low-threshold") or ultimately minimized ("thresholdless laser"), focusing on the spontaneous emission suppression by a strong optical confinement using a photonic nanocavity.

In fact, in a microcavity, the spontaneous emission rate can be greatly enhanced compared with that in free space; this is so-called "Purcell effect"[25]. The Purcell factor is proportional to the ratio between the cavity quality factor (Q) and the mode volume (V_{mode}).

Low threshold lasing has been demonstrated in a three-dimensional polymeric photonic crystal derived from colloidal suspension, with dye molecules incorporated as optical gain medium[26] (Fig. 3.11).

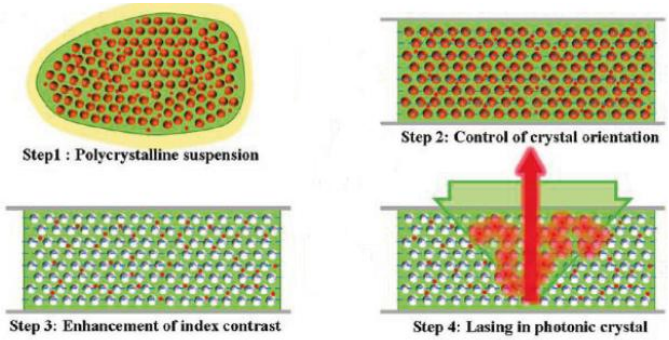

Fig. 3.11 *Scheme for the preparation of porous photonic crystals with high refractive index contrasts and lasing in the photonic crystals (adapted from[26]).*

Under irradiation of excitation light source, the porous photonic film shows strongly enhanced stimulated emission at the band edge by a factor of more than 300 with respect to the spontaneous emission of dye molecules embedded in a bulk film without nanostructure.

Major progress toward the realization of thresholdless nanolasers has been achieved with 2D photonic crystal–based nanocavities with QDs embedded as gain medium[27]. Here, the quantum dot is expected to contribute to thresholdless operation only if the exciton resonance wavelength is the same as that of the resonant wavelength of the nanocavity.

The presence of the nanocavity can conduct to an amplification of light by means of [28]:

- modes with reduced group velocity at a photonic band edge;
- localized defect states inside the photonic band gap.

The infiltrated emitter has to be chosen so that its photoluminescence band overlaps with the stop band of the opal crystal infiltrated (as referred to in section 3.3.1).

This way, the emission spectra at low intensities shows the photoluminescence band characteristic of the emitter, with a narrower emission suppression region that coincides with the opal stop band.

It has to be noticed the possibility to confine light and lead to directional lasing even without a full PBG, in weakly dispersive (“flat”) high-order bands, because the group velocity is reduced over an extended region of the reciprocal space and lasing can occur due to distributed feedback of slow propagating modes in this band (Fig. 3.12).

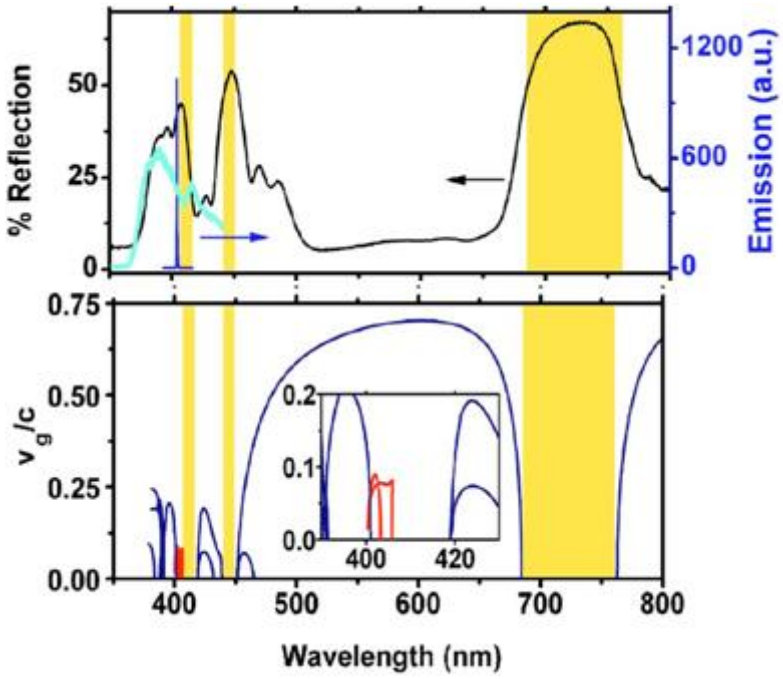

Fig. 3.12 *In the upper part, reflection (black), photoluminescence (light blue) and lasing (dark blue) spectra of a ZnO inverse opal Photonic Crystal (with d=362 nm). Lasing occurs at the high-frequency shoulder of the reflection peak at 407 nm. The photoluminescence exhibits a minimum in this region, confirming the existence of a stop band. In the lower part, representation of the calculated group velocities; light in the weakly dispersive band (red) has a very low v_g over the whole Γ-L range (adapted from[28]).*

Recently, research has placed emphasis on design and introduction of specific defects such as points, lines and layers within the 3D structures, to create localized points and pathways for photons in optical systems. One applicative example is given by Furumi et al.[29], which recently have developed a novel potential system with a light-emitting polymer layer introduced as a planar defect between a pair of colloidal crystals films. It represents a flexible polymer laser device, with low-threshold optical excitation and a highly efficient laser-feedback, due to the previously explained PBG effect of the colloidal crystal films (Fig. 3.13).

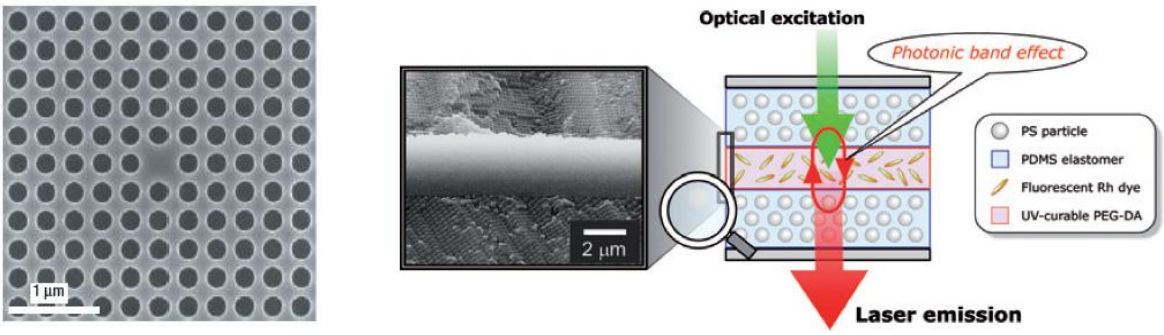

(a) *(b)*

Fig. 3.13 *Single-defect photonic crystal cavity laser with six PhC confining layers around the defect (a) (adapted from[25]). Schematic illustration of a colloidal crystal laser device; the left-hand picture is a cross-sectional SEM image of the magnified light-emitting planar defect between the PS/PDMS colloidal crystal films (b).*

Single-mode lasing is observed from single-cavity structures (Fig. 3.14) which, having larger Q/V_{mode} ratios, should achieve much larger Purcell factors.

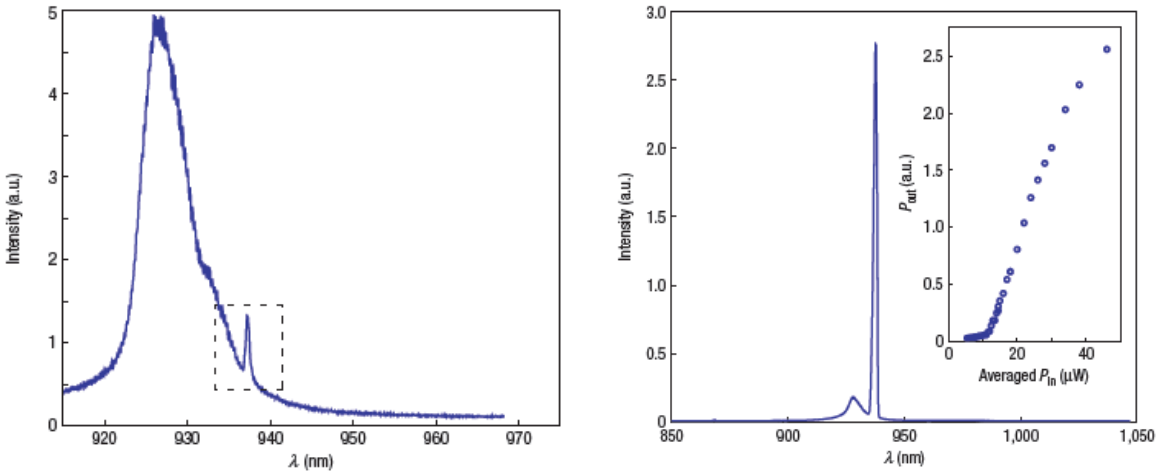

Fig. 3.14 *Spectra of the single-defect photonic crystal laser. Spectrum below lasing threshold (left), the dashed rectangle indicates the cavity mode; spectrum above threshold (right), the inset shows the lasing curve, that is, the input pump power versus output power (adapted from[25]).*

In summary, the PhC lasing mechanism has several unique performance features[30]: the laser emission is linearly polarized in parallel with the excitation polarization and can be observed even at low concentration of the infiltrated emitters; moreover, the threshold excitation energy is relatively low. In particular, this inhibition of undesired spontaneous emission in semiconductor lasers (which degrades their efficiency and performance) attract lots of attentions, in the perspective to obtain this lasing effect at extremely low excitation powers.

3.4.3.2 Random lasing

The random lasing is a different laser action regime, characteristic of photonic glasses, arising from random multiple lights scattering of the spheres-liquid interfaces, which replaces the standard optical cavity of traditional lasers. A propagating light wave in such systems makes a long random walk before it leaves the medium and is amplified in between the scattering events, giving rise to light "trapping" (Fig. 3.15)[31].

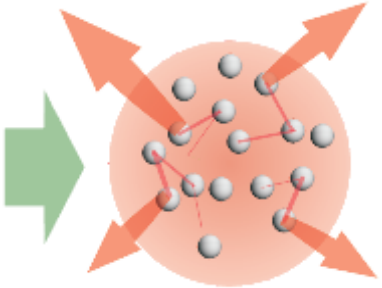

Fig. 3.15 *Schematization of a random laser.*

This effect has been typically observed in high-gain disordered structures, with high density of light scatterers in amplifying medium and with low refractive index contrast; it is strongly dependent on the concentration of fluorescent dye.

Unlike in ordinary lasers, the resulting light emission is multidirectional, but the threshold behavior, the photon statistics and relaxation oscillations are very similar to those of standard lasers.

The laser emission is spectrally seen as random superposition of narrow lasing lines; in opal photonic crystals exhibits multiple lines around the fluorescence maximum wavelength of infiltrated emitters and is not related to the spectral position of photonic stop band.

The lasing wavelength can therefore be controlled by means of the diameter and refractive index of the spheres[32], as the randomly assembled monodisperse spheres can sustain scattering resonances over the gain frequency window.

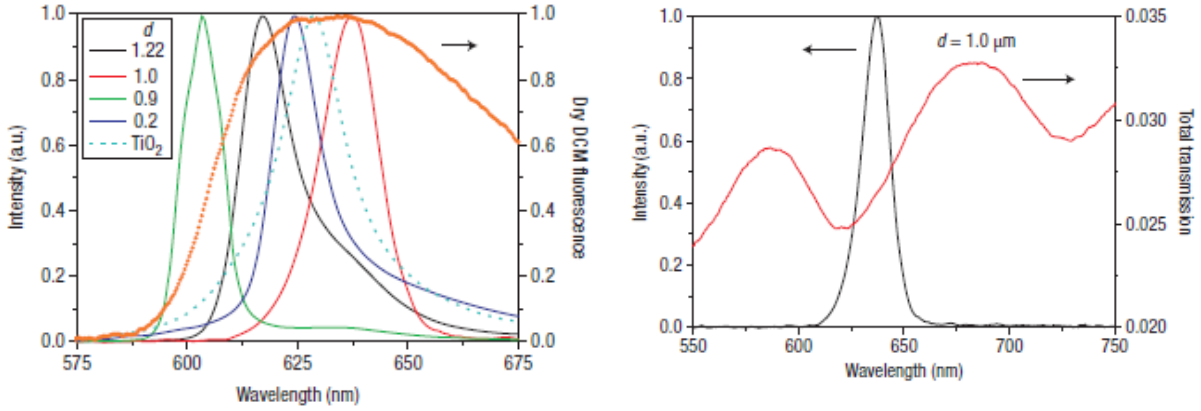

(a) *(b)*

Fig. 3.16 *Random laser emission for photonic glasses with different sphere diameters compared with the pure dry-dye fluorescence (indicated by the arrow) and a reference sample made with TiO_2 powder doped with dry DCM (dotted cyan curve); the pump energy is the same for all samples (a). Emission intensity and total transmission for photonic glasses with d=1µm; lasing occurs close to the transmission minimum (b) (adapted from[32]).*

In Tab. 3.1 are summarized a set of features to discriminate photonic and random lasing regimes.

RANDOM LASER	**PHOTONIC CRYSTAL LASER**
▪ Appears at higher laser threshold. ▪ Multiple emission line output. ▪ Always peaks at λ_{max} independent of the opal stop band. ▪ Low polarization ratio (3:2). ▪ Not observable at low dye concentrations. ▪ Eliminated by index matching.	▪ Lower threshold lasing. ▪ Single or few line output. ▪ Strongly corresponds to the opal stop band. ▪ Higher polarization ratio (15:1). ▪ Attainable even at low dye concentrations. ▪ Converts to conventional distributed feedback lasing in the index-matching case.

Tab. 3.1 *Photonic crystal lasing versus random lasing*

References

1 Miya, T., Terunuma, Y., Hosaka, T. & Miyashita, T. *Ultimate low-loss single-mode fibre at 1.55 μm*, Electronics Letters, 15, 4 (1979) 106-108.

2 Gonçalves, C. M., Fortes, L. M., Almeida, R. M., Chiasera, A., Chiappini, A. & Ferrari, M. *3-D rare earth-doped colloidal photonic crystals*, Optical Materials, 31, 9 (2009) 1315-1318.

3 Laming, R. I., Poole, S. B. & Tarbox, E. J. *Pump excited-state absorption in erbium-doped fibers*, Opt. Lett., 13, 12 (1988) 1084-1086.

4 <http://www.rp-photonics.com/ytterbium_doped_gain_media.html>.

5 Kaczkan, M., Borowska, M., Malinowski, M., Łukasiewicz, T. & Kołodziejak, K. *Up-conversion mechanisms in Er3+ doped YbAG crystals*, physica status solidi (b), 246, 7 (2009) 1677-1685.

6 Lai, B., Feng, L., Wang, J. & Su, Q. *Optical transition and upconversion luminescence in Er3+ doped and Er3+-Yb3+ co-doped fluorophosphate glasses*, Optical Materials, 32, 9 (2010) 1154-1160.

7 Liu, G., Jacquier, B. in *Spectroscopic Properties of Rare Earths in Optical Materials* (Springer, 2005).

8 Kenyon, A. J. *Recent developments in rare-earth doped materials for optoelectronics*, Progress in Quantum Electronics, 26, 4-5 (2002) 225-284.

9 Förster, T. *Zwischenmolekulare Energiewanderung und Fluoreszenz*, Annalen der Physik, 437, 1-2 (1948) 55-75.

10 Dexter, D. L. *A Theory of Sensitized Luminescence in Solids*, The Journal of Chemical Physics, 21, 5 (1953) 836-850.

11 <http://www.rp-photonics.com/energy_transfer.html>.

12 John, S. *Strong localization of photons in certain disordered dielectric superlattices*, Phys Rev Lett, 58, 23 (1987) 2486.

13 Misawa, H. *et al. Tunable single-mode photonic lasing from zirconia inverse opal photonic crystals*, Opt. Express, 16, 18 (2008) 13676-13684.

14 John, S. & Busch, K. *Photonic Bandgap Formation and Tunability in Certain Self-Organizing Systems*, J. Lightwave Technol., 17, 11 (1999) 1931.

15 Nishijima, Y. *et al. Lasing with well-defined cavity modes in dye-infiltrated silica inverse opals*, Opt. Express, 17, 4 (2009) 2976-2983.

16 Lodahl, P. *et al. Controlling the dynamics of spontaneous emission from quantum dots by photonic crystals*, Nature, 430, 7000 (2004) 654-657.

17 Gaponenko, S. V. *et al. Spontaneous emission of dye molecules, semiconductor nanocrystals, and rare-earth ions in opal-based photonic crystals*, Lightwave Technology, Journal of, 17, 11 (1999) 2128-2137.

18 Kalkman, J. *et al. Selective excitation of erbium in silicon-infiltrated silica colloidal photonic crystals*, Journal of Applied Physics, 95, 5 (2004) 2297-2302.

19 Fortes, L. M., Gonçalves, M. C. & Almeida, R. M. *Processing optimization and optical properties of 3-D photonic crystals*, Journal of Non-Crystalline Solids, 355, 18-21 (2009) 1189-1192.

20 Oertel, A., Lengler, C., Walther, T. & Haase, M. *Photonic Properties of Inverse Opals Fabricated from Lanthanide-Doped LaPO4 Nanocrystals*, Chemistry of Materials, 21, 16 (2009) 3883-3888.

21 Kenyon, A. J. *Erbium in silicon*, Semiconductor Science and Technology, 20, 12 (2005) R65-R84.

22 Lezhnina, M. M. & Kynast, U. H. *Inverse opals hosting rare earth species*, Journal of Alloys and Compounds, 451, 1-2 (2008) 545-548.

23 Weber, M. J. in *Handbook on the Physics and Chemistry of Rare Earths* Vol. 4-Non-Metallic Compounds - II (ed Jr. and LeRoy Eyring Karl A. Gschneidner) (North Holland Publishing Company, 1979).

24 Shkunov, M. N., DeLong, M. C., Raikh, M. E., Vardeny, Z. V., Zakhidov, A. A. & Baughman, R. H. *Photonic versus random lasing in opal single crystals*, Synthetic Metals, 116, 1-3 (2001) 485-491.

25 Altug, H., Englund, D. & Vuckovic, J. *Ultrafast photonic crystal nanocavity laser*, Nature Physics, 2, 7 (2006) 484-488.

26 Kim, S.-H., Kim, S.-H., Jeong, W. C. & Yang, S.-M. *Low-Threshold Lasing in 3D Dye-Doped Photonic Crystals Derived from Colloidal Self-Assemblies,* Chemistry of Materials, 21, 20 (2009) 4993-4999.

27 Noda, S. *Photonic crystal lasers-ultimate nanolasers and broad-area coherent lasers [Invited]*, J. Opt. Soc. Am. B, 27, 11 (2010) B1-B8.

28 Scharrer, M., Yamilov, A., Wu, X. H., Cao, H. & Chang, R. P. H. *Ultraviolet lasing in high-order bands of three-dimensional ZnO photonic crystals*, Appl Phys Lett, 88, 20 (2006).

29 Furumi, S., Fudouzi, H., Miyazaki, H. T. & Sakka, Y. *Flexible Polymer Colloidal-Crystal Lasers with a Light-Emitting Planar Defect*, Advanced Materials, 19, 16 (2007) 2067-2072.

30 Furumi, S., Fudouzi, H. & Sawada, T. *Self-organized colloidal crystals for photonics and laser applications*, Laser & Photonics Reviews, 4, 2 (2010) 205-220.

31 Polson, R. C., Chipouline, A. & Vardeny, Z. V. *Random Lasing in π-Conjugated Films and Infiltrated Opals*, Advanced Materials, 13, 10 (2001) 760-764.

32 Gottardo, S., Sapienza, R., Garcia, P. D., Blanco, A., Wiersma, D. S. & Lopez, C. *Resonance-driven random lasing*, Nature Photonics, 2, 7 (2008) 429-432.

Chapter 4

Fabrication and characterization of artificial opals

4.1 Outline

The incorporation of RE ions (Er^{3+} and Yb^{3+}) in an opal-like structure is aimed at the enhancement of the erbium PL intensity, especially the 1.54 μm Er emission, which is situated just inside the so-called third window ("C" band) of fiber communications systems.
Preliminary studies have suggested that, if the host matrix is nanostructured as in a 3D inverse opal structure, the Er^{3+} PL could be enhanced, due to an increased interaction of light within a photonic crystal structure[1].
Considering the photonic laser properties explained in Chapter 3, if the band gap of the PhC is in a range of wavelengths comprising the wavelength of the ion emission, features of inhibition of spontaneous emission can be obtained at the respective stopband positions and enhancement at the band edges[2].
To achieve these conditions, there is the need of a periodic structure of good quality, presenting ordered domains in a reasonable area, in order to show adequate optical properties linked to the Bragg diffraction phenomena.
The self-assembly method has been chosen, because it represents the more rapid, easy and reliable method to grow structures with relatively large quality domains.
The characteristic photonic band gap depends on the size of the spheres and the refractive index contrast. A theoretical simulation has been performed to choose the correct diameter of the spheres to self-assemble with a gap centered in a specific wavelength.
Moreover, there is the need of a structure that presents a complete photonic band gap, in which the electromagnetic waves are forbidden to propagate in any direction of the reciprocal space (as seen in Chapter 1). An FCC opal structure presents a complete gap between the eighth and ninth band only for an inverse opal topology with refractive index contrast >2.9.

For this reason, the Silicon dielectric matrix appears as a material that satisfies all requirements for building an inverse opal with a complete photonic band gap, since it presents a high refractive index (n=3,5) in the VIS[3].

Fig. 4.1 shows the optical reflectance spectrum of Silicon; to operate in a range of wavelengths centered in 1,54 μm the focus will be pointed on the reflectivity band due to high energy bands.

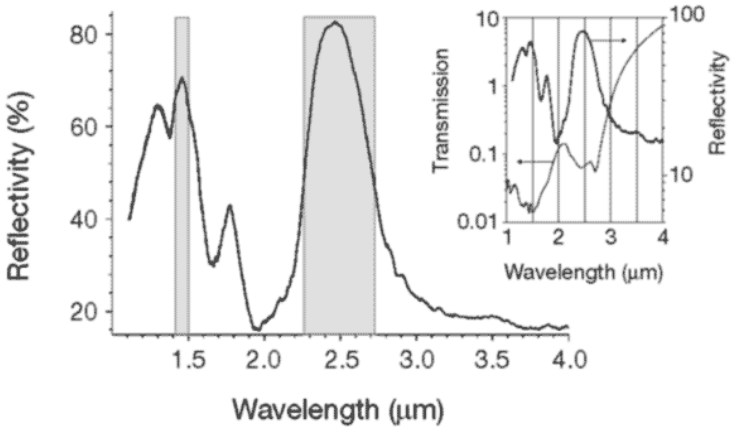

Fig. 4.1 *Optical reflectance spectrum of non-porous Silicon.*

Thus, the choice of an FCC inverse opal structure with a Silicon matrix permits, varying the structure parameter, to syntonize the photonic band gap in the NIR region desired.

4.2 Theoretical simulations

4.2.1 MIT Photonic–Bands software

To simulate the band structure and calculate the correct diameter of the spheres used to fabricate the template for the inverse structure, a theoretical simulation program has been used, the *Massachusetts Institute of Technology Photonic–Bands (MPB) package*.

The MPB package is a free licensed software for computing band structure (dispersion relations) of optical systems, developed by Steven G. Johnson of the "Joannopoulos Ab Initio Physics Group" in the Condensed Matter Theory division of the MIT Physics Department.

It computes definite−frequency eigenstates and eigenvalues of Maxwell's equations directly, using a planewave basis, in periodic dielectric structures. Its primary intended application is the study of PhCs.

For the calculus of the bands, it is necessary to specify the number of eigenvectors to be computed for the structure under study.

The program starts by making the calculation of the band structure of a direct opal, composite material (with an FCC arrangement) of dielectric spheres embedded in air; then it calculates the band structure of an infiltrated opal, composed of spheres embedded in silica and, finally, it calculates the band structure of an inverse opal, composed of spheres of air in a silica or silicon matrix.

In each case the FCC and filling material change, and so they have been adapted to adequate dielectric properties.

The parameters used by the program have default settings, the ones to specify are:

- the number of bands computed at each *k* point (eigenstates);
- the set of *k* points (Bloch wavevectors) to compute the bands at, parameter that is controlled by a list of three dimensional vectors;
- the constants related to the structure: radius of the spheres (in normalized units, $r = \sqrt{1/8} \sim 0.353553$) and dielectric constants of the materials of the composite (summarized in Tab. 4.1);

Material	**Refractive index (n) (@ 589.6 nm)**
Polystyrene (PS)	1.59
Polymethilmetacrylate (PMMA)	1.49
Air	1.0
Silicon dioxide	1.45
Silicon	3.50

Tab. 4.1 *Refractive index of the materials used in the opal-like structures.*

- the geometry of the system (lattice of the primitive cell) (Fig. 4.2).

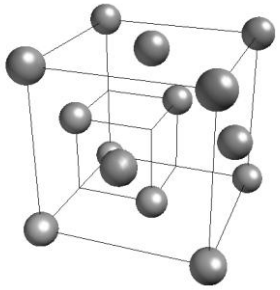

Fig. 4.2 *Schematic representation of the conventional unit cell and of the primitive cell of an FCC lattice.*

The output file contains the data corresponding to the band structure, which permit to plot the curves *w(k)*: the *k* index, the *k* components and magnitude and the frequencies of the calculated modes.

The band structure curves present the wave vector *k* in the horizontal axis, which follows a trajectory on the Brillouin zone, linking high symmetry points; in the vertical axis, the frequency in reduced units of a/λ, where a is the lattice parameter and λ the wavelength of light in vacuum. The lattice parameter a and diameter of the spheres ϕ are related by the following equation:

$$\frac{a}{\lambda} = \frac{\sqrt{2}\phi}{\lambda} \quad [4.1]$$

The convenience of the variable change is justified by the scalability of the solutions of the problem; the scalability of the Maxwell equations allows a common solution for similar structures with different lattice parameter. The solution of the problem at one length scale determines the solutions at all other length scales; the absence of a fundamental length scale in the above equations implies that a change in the length scale of the system is translated into a corresponding change in the energy scale of the eigenvalues.

To give an example, the variables of the band structure for an FCC structure composed of spheres of 400 nm diameter are the same as an FCC structure composed of spheres of 1 mm of the same material.

The graphs derived from the calculation of some photonic band structure, for the different intermediate configurations used to reach the inverse silicon opal structure, are presented in the following figures.

In Fig. 4.3, it is shown the band structure for a direct opal structure of PS spheres embedded in air, presenting a forbidden frequency interval that appears along the Γ-L direction for a reduced frequency $a/\lambda \sim 0.6$. This corresponds to the case of the pseudo gap, a frequency interval for which light may not propagate along certain directions.

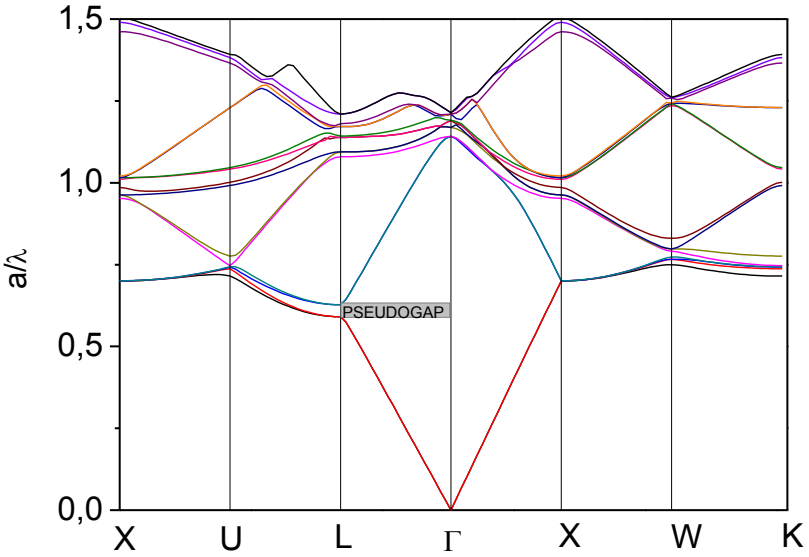

Fig. 4.3 *Band structure for a system composed by PS spheres in an air matrix.*

The infiltrated opal is composed of PS spheres in a silica matrix and its band structure showed in Fig. 4.4 presents a reduced forbidden frequency interval that appears along the Γ-L direction for a reduced frequency a/λ~0.6. This can be explained by the fact that the two materials have a very similar refractive index (n_{PS} = 1.59; n_{SiO2} = 1.45), so the effect of Bragg diffraction is reduced, compared to the case of a high index contrast.

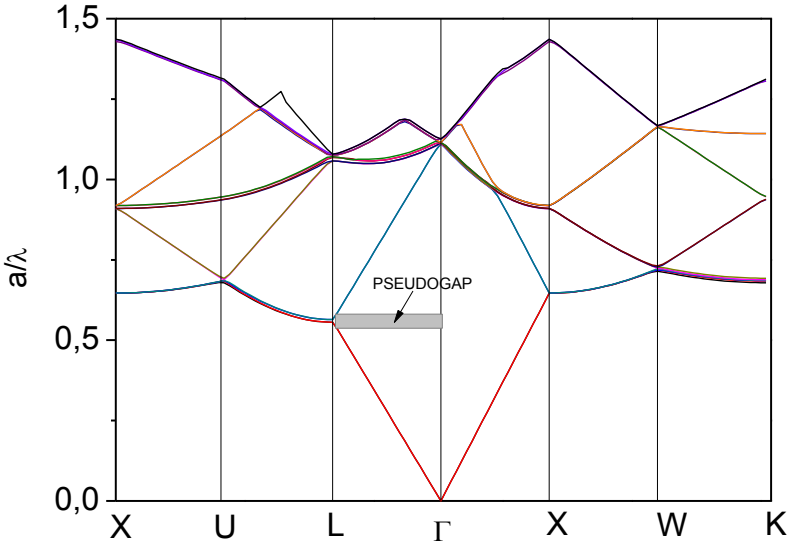

Fig. 4.4 *Band structure for a system composed by PS spheres in a silica matrix.*

The silica inverse opal structure presents a forbidden frequency interval that appears along the Γ-L direction for a reduced frequency a/λ~0.8.

As can be seen in Fig. 4.5, in this case the pseudo gap is wider and positioned at higher energy values.

This is due to the increasing difference between the refractive index of the material constituting the spheres and the matrix material (n_{AIR} = 1.0; n_{SiO2} = 1.45), and a global reduction of the effective index of the composite.

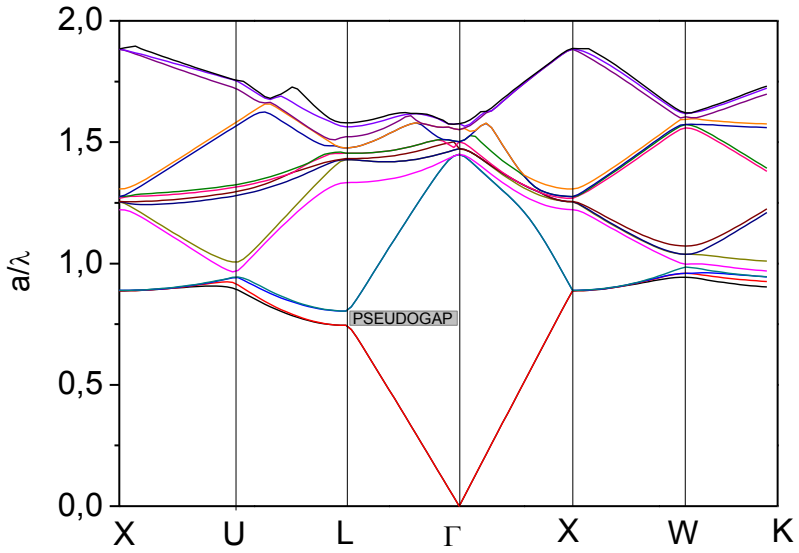

Fig. 4.5 *Band structure for a system composed by air spheres in a silica matrix.*

The porous silicon inverse opal band structure is shown in Fig. 4.6; the volume fractions used were 0.65 for the pores and 0.35 for Si. It presents a forbidden frequency interval that appears along the Γ-L direction for a reduced frequency a/λ~0.7. In this case, the pseudo gap is wider than in the previous case, due to the fact that the index contrast between the two materials of the composite is increasing (n_{AIR} = 1.0; n_{SiP} = 1.7).

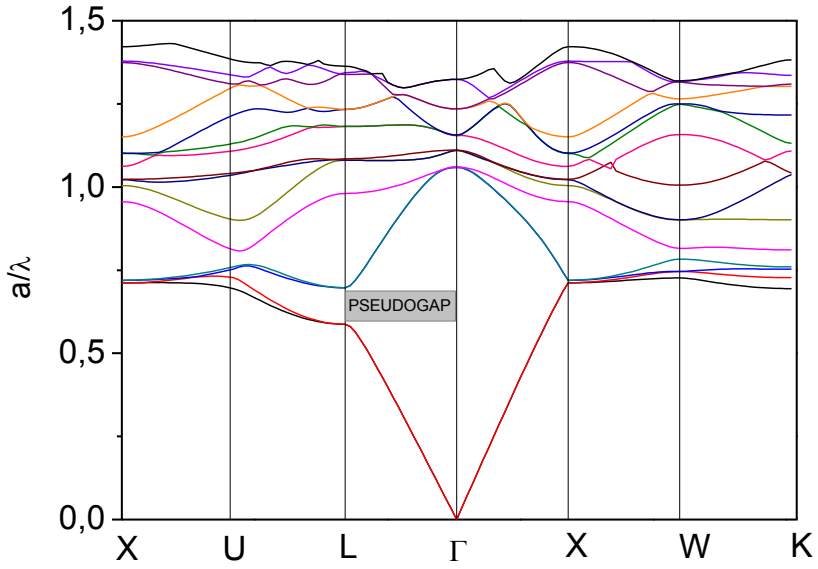

Fig. 4.6 *Band structure for a system composed by air spheres in a porous silicon matrix.*

Finally, in Fig. 4.7 is presented the photonic band structure for an FCC structure of air interconnected spheres in a non-porous silicon matrix (n_{SiNP}=3.5), accompanied by a schematization of the first Brillouin zone for an FCC structure.

The high symmetry directions in the reciprocal space are shown and the corresponding directions in the real space. The (111) planes in the real space correspond to the direction Γ-L of the Brillouin zone, the (100) planes to the direction Γ-X, etc. More information about this are found in ref.[4].

In this band structure the difference between a pseudo gap and a complete photonic gap can be clearly distinguished.

Light propagating with energy in the range comprised between a/λ=0.4 and a/λ=0.5 cannot propagate in the direction Γ-L because of the absence of available states, so the photons of this energy can propagate only in other directions; this range of energy is called the existing pseudo gap of this structure. A complete photonic gap is defined when exists an energy interval in which the photons cannot propagate, for any directions inside the crystal, and for this structure is found for an energy range between *a*/λ=0.76 and *a*/λ=0.82, that corresponds to the region between the eighth and ninth band. As anticipated, it exists here because the threshold value of 2.9 for the refractive index contrast is overcame and it is about 3.5 (n_{AIR} = 1.0; n_{SiP} = 3.5).

Moreover, its appearance is favored due to the fact that an FCC lattice presents the most spherical Brillouin zone of all 3D Bravais lattices. This means that the periodicity is similar along different directions and therefore it is more probable that forbidden intervals overlap for a sufficiently large refractive index contrast.

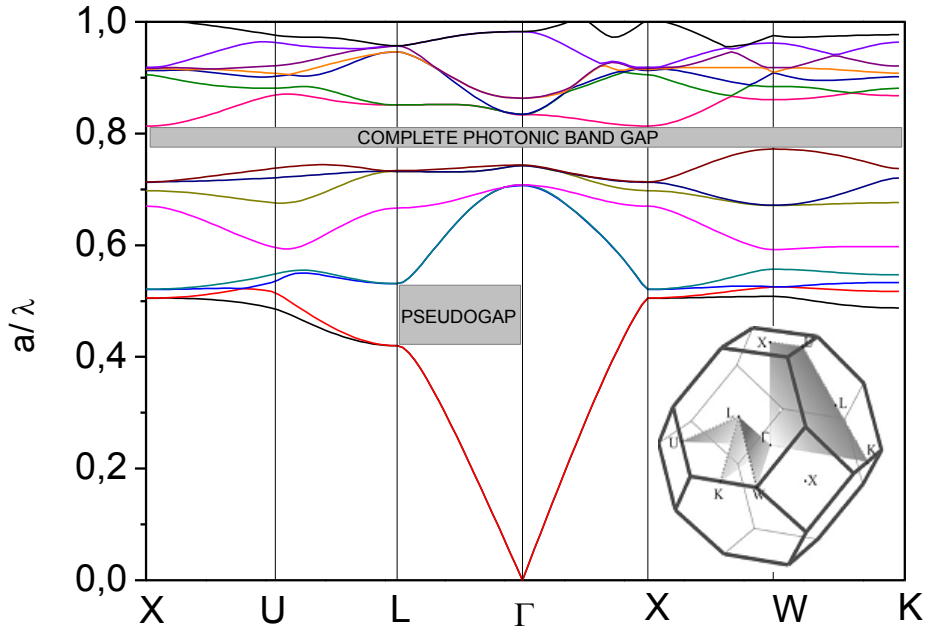

Fig. 4.7 *Band structure for a system composed by air spheres in a non-porous silicon matrix.*

Starting from the knowledge of the frequency value where the complete photonic band gap is opened, the correct dimension of spheres to be used in the production of the inverse opals can be calculated, using the equation that correlates the lattice parameter with the diameter of spheres. Therefore, this calculus has been made considering the values of an a/λ=0.82 and the desired wavelength where to place the band gap λ=1.54 μm, and, by the proper substitutions, the searched value of diameter has been found to be a ϕ =870 nm.

4.2.2 Modified Bragg's law approximation

An approximation of the theoretical calculations of the photonic band gaps can be made using the modified form of the Bragg's law. It allows the calculus of the photonic gap, by means of the diameter of particles (D), the interplanar spacing (d) and the effective refractive index of the composite (n_{eff}).

This calculus is very useful to have an idea of the position and the displacement of the main stopband with the variation of the composition of the opal under study. For this reason, it will be a useful tool to evaluate the spectra obtained.

Tab. 4.2 are reported the calculations for the opal structures of interest in this experimental work.

COMPOSITE STRUCTURE					**λ PBG (nm)**			
			D(nm)	235.00	430.00	652.00	870.00	1000.00
			d(nm)	191.88	351.09	532.36	710.35	816.50
		n_{eff}						
DIRECT OPAL	***PS***	1.37		524,89	960.43	1456.28	1943.20	2233.56
INFILTRATED OPAL	***PS/SiO_2***	1.56		597.60	1093.48	1658.02	2212.38	2542.97
INVERSE OPAL	***AIR/SiO_2***	1.14		436.57	798.83	1211.25	1616.24	1857.75
	AIR/Si(p)	1.26		482.74	883.31	1339.34	1787.15	2054.20
	AIR/Si(np)	1.98		760.28	1391.15	2109.37	2814.64	3235.22

Tab. 4.2 *Photonic band gap calculations by the modified form of Bragg's law.*

The drawback of this method is that it allows the calculus of the position of the main stopband, while the MPB program shows the complete theoretical band structure.

In our specific case, for example, the interest is in the wavelength positioned in 1.54 μm in the non-porous silicon inverse opal and it does not represent the primary photonic stopband of the structure but, as seen in Fig. 4.1, a secondary reflectivity band due to high energy bands.

To summarize: using the theoretical calculations, the inverse opal structure of silicon matrix, in a FCC arrangement, with 870 nm hollows, has been proved to present a complete photonic band gap in the range of wavelengths of interest in the near IR, centered in 1.54 μm.

The doping of this kind of structure with RE (erbium), presenting an emission in 1.54 μm will allow to study the changes in the behavior of light in such a structured matrix.

4.3 Experimental

4.3.1 Colloidal particles

Monodisperse colloidal particles of Polystyrene (PS) or Polymethilmetacrylate (PMMA), commercially available, have been used to prepare the opal-based photonic crystals.

Spheres of different diameters (240 nm, 430 nm, 625 nm, 870 nm and 1000 nm- approximately 3% standard deviation) have been tested, aiming at the optimization of the opal growth process.

For the preliminary tests, the PS particles of 240 nm supplied by "Istituto di Fotonica e Nanotecnologie", of the University of Trento (Italy) have been used.

Tab. 4.3).

Chemical Formula	**Acronym**	**Concentration (v/v)**	**Average diameter (nm)** (3% monodispersity)	**Refractive index (n)**	**Density (g/cm^3)**
[CH2CH(C6H5)]n	PS	10%	240, 430, 870, 1000	1.59	1.05
$[C_5H_8O_2]n$	PMMA	10%	625, 870, 1000	1.48	1.19

Tab. 4.3 *Properties of the commercial suspensions of PS/PMMA particles in water.*

4.3.2 Substrates

The opals have been deposited on borosilicate glass and silicon substrates.

In the primary part of the experimental work, the deposition on glass substrate was used to study the direct opal structures.

Silicon substrate was chosen for the next steps of the work, as a substrate resistant to high temperatures is required for the processing of the inverse structures.

- **Borosilicate Glass**

Borosilicate glass is mainly composed by silica and boron oxide. Borosilicate glasses are known for having very low thermal expansion coefficients (~5×10^{-6}/°C at 20°C), making them resistant to thermal shock.

Borosilicate glass slides (3 cm x 1 cm) were used as substrates.

The glass has been washed with water and soap, rinsed in bi-distilled water and dried, then put in a vial containing Hydrogen Peroxide (H_2O_2) in a 80°C water bath for nearly an hour,

and finally rinsed and dried again. This washing treatment is necessary for a correct hydrophilization of both the substrate and the vial.

Hydrophilization of the substrate is very important to achieve a correct and homogeneous wettability of all the surface, avoiding the presence of water drops, as the PS and PMMA particles are in aqueous suspensions.

The hydrophilization of the vial is important too, because it allows a more stable and uniform disposition of the suspension on the substrate. For these reasons, the growth of the opals will be taken inside the hydrophilized vials.

- **Silicon wafer**

Monocrystalline silicon or single-crystal Si, or mono-Si is the base material of the electronic industry.

The Silicon substrates have been cut from Si wafer monocrystalline <100> double-side polished. The double-side polishing was chosen as FTIR measurements in transmission mode are planned. Different procedures of cleaning have been tested for these substrates, in order to obtain the more stable hydrophilization and achieve the best adhesion of the spheres, and the results will be presented in section 4.5.1.

4.3.3 Deposition and growth

The vertical deposition method has been chosen for the growth of the opals on glass or silicon substrates. The composition of the suspension and the processing parameters have been optimized for every different opal structure, in order to obtain the best adhesion of the particles to the substrate and the best ordered 3D PhCs.

4.3.4 Characterization techniques

- **Optical Microscopy**

The optical microscope used is an adapted equipment with Nikon optics.

The photos were taken in reflectance, with a 10x microscope objective.

- **Fourier Transform Infrared Spectroscopy (FTIR)**

Fourier transform infrared spectroscopy (FTIR) is a measurement technique whereby spectra are collected based on measurements of the coherence of a radiative source, using time-domain or space-domain measurements of the electromagnetic radiation or other type of radiation.

FTIR uses an interferometer to expose the sample to all wavelength of light in the selected range and a composite response is recorded[5].

Optical transmission and reflection spectra in the visible (VIS)-near infrared (NIR) region and middle infra red (MIR) region were measured at room temperature.

A Thermo Nicolet 5700 Fourier transform infrared spectrometer equipped with a quartz beamsplitter, a DTGS detector and a white light source, at a resolution of 4 cm^{-1} has been used for the measurements made in "Instituto Superior Tecnico (Lisboa)" and an IFS 66S from Bruker Fourier transform Infrared spectrometer, with an IR microscope attached has been used for the measurements made in "Instituto de Ciencia de Materiales de Madrid (Madrid)".

As the artificial opals analyzed were deposited on borosilicate glass and silicon substrates, before collecting the spectrum, a background acquisition has been made in reflectance using a mirror and in transmittance using a glass or silicon cleaned substrate.

The optical characterization of opals has been done with normal incidence reflectance and transmission measurements, which evidenced the presence of a photonic gap in Γ-L direction as a function of the incidence angle.

A general criterion has been chosen in order to compare spectra from different samples. This criterion is based on the study of Galisteo[6] and concerns the use of an optical microscope, where a thicker sample area is selected to make the measurement. This operative choice has enabled to compare the experimental results with the theoretical simulations.

In fact, photonic bands, being an exact solution of the propagation of electromagnetic radiation inside an infinite crystal, cannot account for the optical properties of finite systems, and finite size effect in this case are likely to modify the optical behavior of the finite real system in comparison with the infinite ideal one[7]. In Fig. 4.8 can be noticed the dependence of the width of the stopband on the film thickness; the width is inversely proportional to the number of lattice planes and arbitrarily narrow lines should be obtained by increasing the crystal thickness. However, in the colloidal crystals studied here, the narrowing of the stopband saturates above a certain critical thickness.

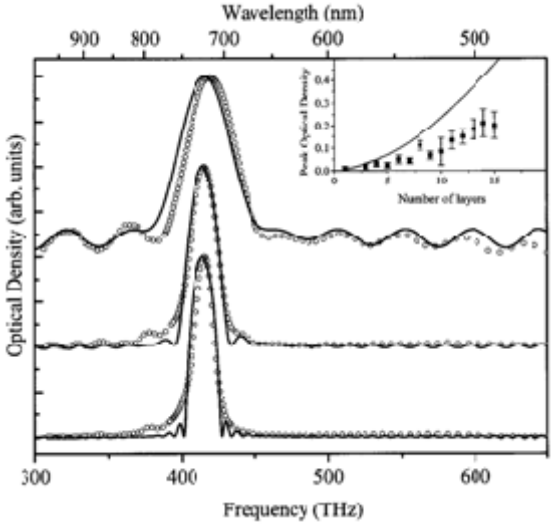

Fig. 4.8 *Normal-incidence optical density spectra for different films of close-packed arrays of silica spheres of ~342 nm diameter, with (from top to bottom) 9, 25 and 50 layers. The solid curves are calculated using an analytic approach called "scalar wave approximation" (SWA).The inset shows the monotonic increase in peak optical density with thickness; the solid line shows the SWA prediction (adapted from[7]).*

Depending on the substrate, borosilicate glass or silicon, the peak center will monotonically increase or decrease in frequency with the number of (111) lattice planes before merging into a common behavior. The number of 23 layers has been found to be the limit to do a correct approximation of the optical properties of a finite opal with an infinite crystal[6].

In a large number of cases, the central area of the sample has been found to present the major and more homogeneous thickness.

- **Field Emission Scanning Electron Microscope (FE-SEM)**
- **Energy Dispersive X-ray Spectroscopy (EDS)**

Electron microscopy in the secondary electron mode is used to study the morphologic aspect on the surface and the lattice structure of the photonic crystals.

A JEOL JSM-7001F field emission scanning electron microscope (FE-SEM) has been employed in "Instituto Superior Tecnico-Lisboa", while a FEI Nova NANOSEM 230 scanning electron microscope (FE-SEM) has been used for the images collected in "Instituto de Ciencia de Materiales de Madrid-Madrid".

EDS analysis provides a rapid qualitative and quantitative analysis of elemental composition of the structure (with a sampling depth of 1-2 microns).

It is achieved by means of the emission of an X-ray which results from the interaction of the primary beam with the atoms in the sample, since the emitted X-ray has an energy characteristic of the parent element.

- **Photoluminescence (PL)**

Photoluminescence (PL) is one of many forms of luminescence (light emission) and it is a process in which a substance absorbs photons (electromagnetic radiation) and then re-radiates photons. Quantum mechanically, this can be described as an excitation to a higher energy state and then a return to a lower energy state accompanied by the emission of a photon. The period between absorption and emission is extremely short, in the order of 10 nanoseconds.

The photoluminescence intensity I_{PL} will be proportional to:

$$I_{PL} \propto \frac{N^*}{\tau_{rad}} \quad [4.2]$$

where N is the number of excited centers and τ_{rad} is the mean radiative life of the system. The emission wavelength gives information on the type of the center that is emitting.

The PL measurements were conducted in "Instituto Superior Tecnico (Lisboa)".

To measure the energy transfer effect between Yb^{3+} and Er^{3+} ions in erbium/ytterbium co-doped samples, excitation was performed using an excitation source at 975 nm. The setup consists of a laser diode (referring model is Lumics LU0975T080-D605N12A Laser Module TO-220, 975 ± 5nm, with a power until 8W) with the emitted light being recorded with an InGaAs array detector (Control Development Inc., CDI-NIR/256/L, at 6 nm resolution). In Fig. 4.9 is represented the configuration adopted for the measurements; the fiber coming from the laser has been focused using a lens, aligning the beam with the sample, which is put in the respective sample-holder, and receiving the signal coming from the sample with the detector.

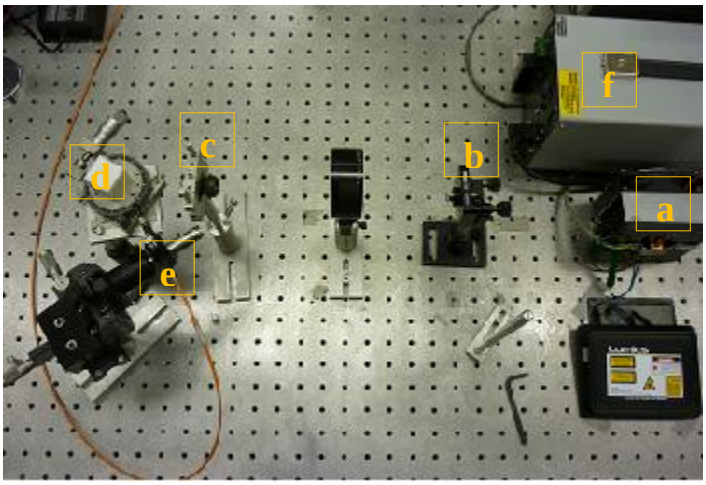

Fig. 4.9 *Laser Lumics LU0975T080-D605N12A, excitation source at 975 nm. Laser (a); fiber (b); lens (c); sample-holder (d); detector (e) and power source (f).*

To measure the Er^{3+} emission in erbium doped samples, excitation was performed with the 514 nm line of an argon ion laser, referring model Spectra-Physics, Stabilite 2017, Argon/Kripton, with a maximum power of 20 W. In Fig. 4.10 is presented the configuration adopted with this laser: the beam coming from the laser is directed to the sample by means of two lenses and two mirrors. Through them, the beam was focused on the sample, placed in the sample holder and the emitted signal is collected by a InGaAs array detector (Control Development Inc., CDI-NIR/256/L model, at 6 nm resolution).

All measurements were performed at room temperature.

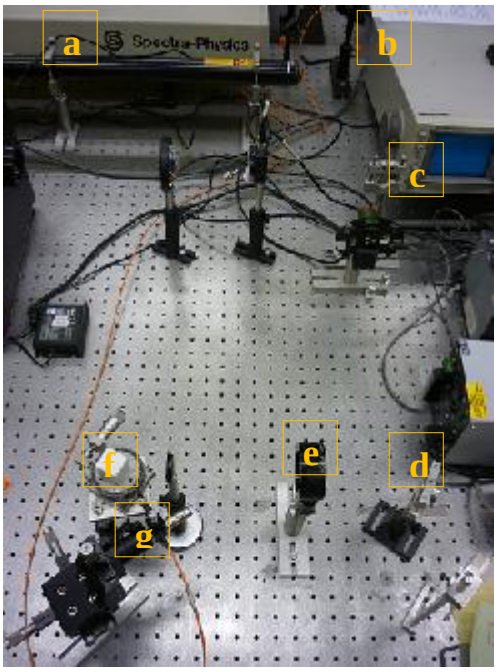

Fig. 4.10 *Laser Spectra-Physics, Stabilite 2017, Argon/Kripton, excitation source at 514 nm. Laser (a); mirror (b); lens (c); mirror (d); lens (e); sample-holder (f) and detector (g).*

4.3.5 Deposition techniques

- **Self-assembly**

Due to the large importance of the self-assembly in this work, Chapter 2 has been dedicated to this method.

- **Chemical Vapor Deposition (CVD)**

Chemical vapor deposition (CVD) is a generic name for a group of processes that involve depositing a solid material of high-purity from a gaseous phase on a solid substrate; chemical precursors are transported in the vapor phase and let to decompose on a heated substrate to form a film. The films may be epitaxial, polycrystalline or amorphous depending on the

materials and reactor conditions. The transport of the precursor is made by the use of a gas (e.g. oxygen, argon, hydrogen), which is also used to remove from the system the gaseous decomposition products from the surface of the film. The reaction responsible for the formation of the film on the substrate is the chemisorption.

A normal CVD process involves complex flow dynamics since gases are flowing into the reactor, reacting, and then by-products are exhausted out of the reactor.

The sequence of events during a CVD reaction are:

1. precursor gases input into the chamber, by pressurized gas lines;
2. mass transport of precursors from the main flow region to the substrate through the boundary layer;
3. adsorption of precursors on the substrate (normally heated);
4. chemical reaction on the surface;
5. atoms diffusion on the surface to growth sites;
6. desorption of by-products of the reactions;
7. mass transport of by-products to the main flow region.

CVD has many advantages: the pressures used allow coating of 3D structures, whose stoichiometry is more easily controlled by monitoring flow rates of precursors and high precursor flow rates give high deposition rates, the use is relatively simple and ultra-high vacuum is not needed.

The main disadvantages of this technique are that precursors are often hazardous or toxic and therefore extra steps have to be taken in the previous handling and in the treatment of the reactor exhaust. Also, many precursors for CVD, especially the metal-organics, are relatively expensive[8].

- **Atomic Layer Deposition (ALD)**

Atomic Layer Deposition (ALD) is a thin film deposition technique, based on the sequential use of a gas phase chemical process, exposing the precursors to the growth surface one-at-a-time in a sequential manner. The substrate is exposed to the first gaseous precursor molecule (elemental vapor or volatile compound of the element) in excess and the temperature and gas flow is adjusted so that only one monolayer of the reactant is chemisorbed onto the surface (Fig. 4.11-a). The excess of reactant, which is in the gas phase or physisorbed on the surface, is then purged out of the chamber with an inert gas pulse before exposing the substrate to the other reactant (Fig. 4.11-b). Then, the substrate is exposed to the second reactant, that chemisorbs and undergoes an exchange reaction with the first reactant on the substrate

surface, or to another treatment to activate the surface again for the reaction of the first precursor (***Fig. 4.11***-c). This results in the formation of a solid molecular film and a gaseous side by-product that may then be removed with an inert gas pulse (***Fig. 4.11***-d)[9].

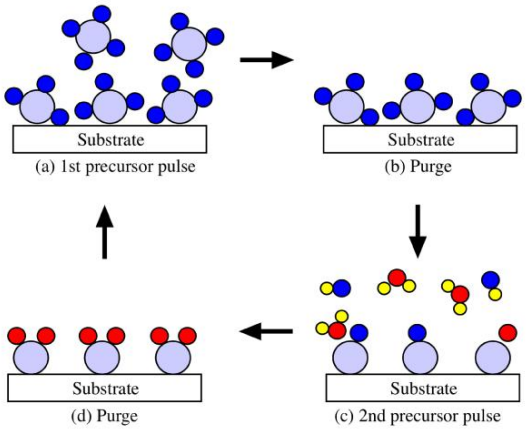

Fig. 4.11 *Schematic representation of the ALD process.*

One basic condition for a successful ALD process is that the binding energy of a monolayer chemisorbed on a surface is higher than the binding energy of subsequent layers on top of the formed layer; thus, the temperature must be kept low enough to keep the monolayer on the surface until the reaction with the second reactant occurs, but high enough to re-evaporate or break the chemisorption bond.

The concept of "ALD-window" indicates the temperature range where thin film growth proceeds by surface control resulting in a constant growth rate[10].

Using ALD, film thickness depends only on the number of reaction cycles, which makes the thickness control accurate and reproducible. One cycle may take time from 0.5 to a few seconds and deposit between 0.1 and 3 Å of film thickness.

ALD can be used to deposit several types of thin films, including various oxides (e.g. Al_2O_3, TiO_2, ZnO), metal nitrides (e.g. TiN, WN), metals and metal sulfides.

The ALD of Er_2O_3 and Yb_2O_3 on the opal-based structures was made in "Instituto de Ciencia de Materiales de Madrid (Madrid)", using a Cambridge NanoTech Inc. Savannah 200 Reactor showed in Fig. 4.12.

Fig. 4.12 *Atomic Layer Deposition (ALD) reactor.*

4.4 Fabrication of the direct opals

4.4.1 Self-assembly process

Direct opals self-assembled with PS spheres of different diameters have been produced by a vertical deposition method.

Parameters which influence the growth of the opals are:

- the type of substrate, which influences the adhesion of the particles;
- the diameter of the spheres and the spheres colloidal concentration, which are known to determine the thickness of the samples; in general, smaller and more monodisperse spheres sizes and greater colloidal concentrations yield samples with a better quality and a higher number of staked layers. A smaller starting colloidal concentration would imply a longer time scale in order to reach the threshold volume fraction to crystallize;
- the temperature; larger diameter spheres will need higher temperatures to prevent sedimentation;
- the nature of the solvent;
- the evaporation rate; a slower evaporation rate allows more time to reach a better arrangement of particles.

Based on the experience in direct opals growth acquired in Lisbon research group[11], hydrophilized substrate (borosilicate glass) have been immersed with an angle of inclination

of 20° in a 5 ml vial containing ~3 ml of an aqueous suspension of PS spheres, as illustrated in Fig. 4.13.

Fig. 4.13 *Vial containing 3 ml of PS particles colloidal suspension.*

The concentration of the suspensions was 0,1 vol%; diameters of the PS spheres of 235 nm and 1 μm were tested. 235 nm particles have been chosen to illustrate small diameter particles, while 1 μm particles to approximate the diameter needed for the PL enhancement.
The colloidal PS suspensions evaporated within 36 h, in an oven at the temperature of 45°C, and RH~25%, after which an iridescent array of spheres remained on the glass substrate.
Since the formation of good crystalline regions is strongly dependent upon the local density of spheres, sudden movements of the vials and fluctuations of temperature in the oven should be minimized, in order to reduce structural defects.

4.4.2 Results and discussion

The optical properties of the PS opals are shown in a reflectance and transmittance FTIR spectrum.
The presence of the Bragg diffraction peak evidences the stopband position, which corresponds to the photonic band gap of the structure.
The position and width of the Bragg peak depends on:

- the lattice constant (spacing between spheres);
- the filling factor (volume of the spheres/volume of the surrounding phase);
- the refractive index contrast between the two periodic media (PS spheres and surrounding phases-air in the opal case).

In Fig. 4.14 (a) and (b) are represented the reflectance spectra derived from the direct opals produced; Bragg peak is correctly placed in λ~530 nm, according to the modified Bragg's law calculations, for PS=235 nm, while for PS=1 μm the peak is not visible at the expected

wavelength value of ~2200 nm. The inset in (b) shows the wavelength position in which the peak was expected.

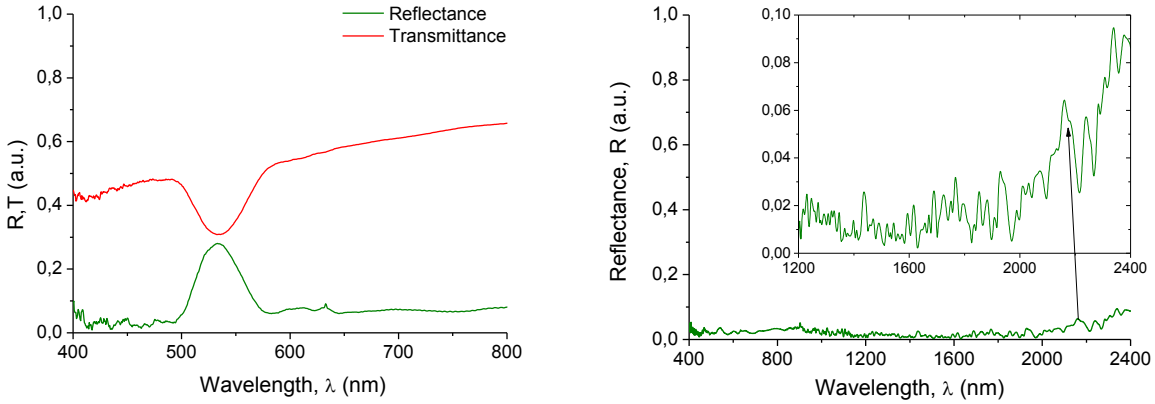

Fig. 4.14 *Optical reflectivity spectra for a direct opal made from a 0,1vol% aqueous suspension of PS spheres , in a volume=3 ml, for 235 nm (a) and 1 µm spheres (b).*

The self-assembly of 1 µm diameter particles is more difficult to achieve, as sedimentation is a competition process.

Role of the meniscus edge

The motion of the microparticles results from the competition between different forces acting on them. These forces include surface tension, due to the change of meniscus profile during liquid evaporation, as well as adhesion forces between the particles and between the particles and the substrate.

The coffee ring phenomenon is defined as the ability in concentrating particles at the rim of a dried liquid droplet[12]; the surface tension acting on the particles at the leading edge of the coffee ring structure tend to move the structure away from the contact line. The adhesion force acting within individual particle/substrate interfaces tend to resist such a motion.

A study has been made on the role of the meniscus edge, which represents the site of the first contact between the substrates and the particles and where evaporation rate is the highest[13]. In this region, as more microparticles arrive and the local volume fraction reaches the threshold to crystallize, the interparticle interactions provide the driving force to form a small cluster of an ordered monolayer, which is the onset of nucleation.

As drying proceeds, there is a buildup of immersion capillary forces while the crystal grows with the continuous flow of microparticles to the meniscus edge (As explained in Chapter 2). For a well-ordered monolayer with high crystallinity and minimum defects, the delivery speed

of the microparticles should equal the crystal growth rate. A presumable hypothesis about the larger sized aggregates is that they lose the mobility to rearrange, so they adhere onto the glass surface randomly.

Further, the sedimentation tendency competes with convective fluxes and the amount of microparticles in the meniscus decreases with time. A higher volume of suspension could modify the shape of the meniscus that reduce the surface tension, keeping the microparticles for longer times near the interface line.

For this reason, another set of samples has been prepared to test the effect of different volume contents. Hydrophilized borosilicate glass substrates were immersed with an angle of 20°, in a 20 ml vial containing ~10 ml of an aqueous suspension of PS spheres, as illustrated in Fig. 4.15. The concentration of the suspension and the evaporation parameters are the same as the previous tests.

Fig. 4.15 *Vial containing 10 ml of PS particles colloidal suspension.*

Fig. 4.16 (a) and (b) represent reflectance spectra of direct opals produced in a 10 ml volume. Photonic band gap peak position is positioned at λ~530 nm, according to the modified Bragg's law, for PS = 235 nm, with an increase in optical reflectivity intensity.

For PS = 1 μm the peak is clearly visible and positioned at the wavelength of ~ 2400 nm, near the expected value of ~ 2200 nm, with a good reflectivity of ~ 0,5.

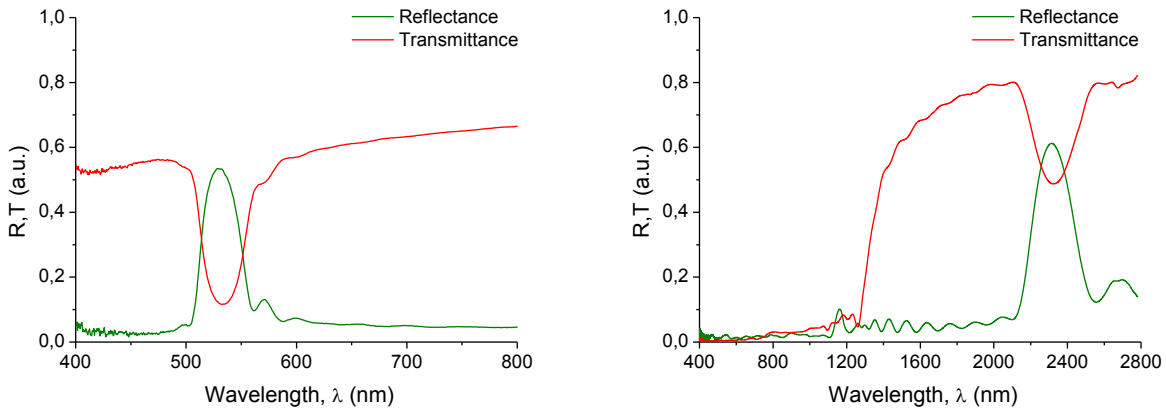

(a) *(b)*

Fig. 4.16 *Optical reflectivity spectra for a direct opal made from a 0,1vol% aqueous suspension of PS spheres, in a volume=10 ml, for 235 nm (a) and 1µm spheres (b).*

The obtaining of the stopband of 1µm PS opal shows the importance of the meniscus in the self-assembly process for particles of big diameters. For this reason, all the following opal growths will be made using 10 ml volume solutions.

To highlight the dependence of the Bragg peak with the spheres diameter, a comparative study based on reflectance spectra is presented in Fig. 4.17, for PS direct opals of increasing spheres diameter: 240, 430, 870 and 1000 nm. For all the samples, reflectance and transmittance spectra indicate that the Bragg's peak is well defined, which proves that the structure is ordered and periodic.

The opals made of PS spheres of dimension 240 and 430 nm show a narrower and "sharper" peak (compared to the 870 and 1000 nm samples) with higher values of Q factor, which is an evidence of very good reflectance properties. So, in terms of sample thickness and optical quality, in the range of sphere diameter 200-450 nm similar results have been found, independently of sphere size, while for spheres with a diameter of 850-1000 nm, these conditions vary.

According to the modified Bragg's law, there is a red shift of the peak with the increment of the diameter.

Intensities of the Bragg peak comprised in a range of values between 0,6 and 0,8 (y-axis) indicate opals of very high quality, even if the reflectance values achieved have not to be considered as absolute values, because, as we demonstrated before, this kind of measurements is very sensitive to the area of the sample where the spectrum is taken.

Scanning Electron Microscopy (SEM) is a useful tool for the correct in-depth investigation and structural characterization of PhCs as it can show the presence of crystalline order and/or defects at a nano-level scale.

The images presented in Fig. 4.18 show the PS opals under study (all have been taken from the central part of the sample).

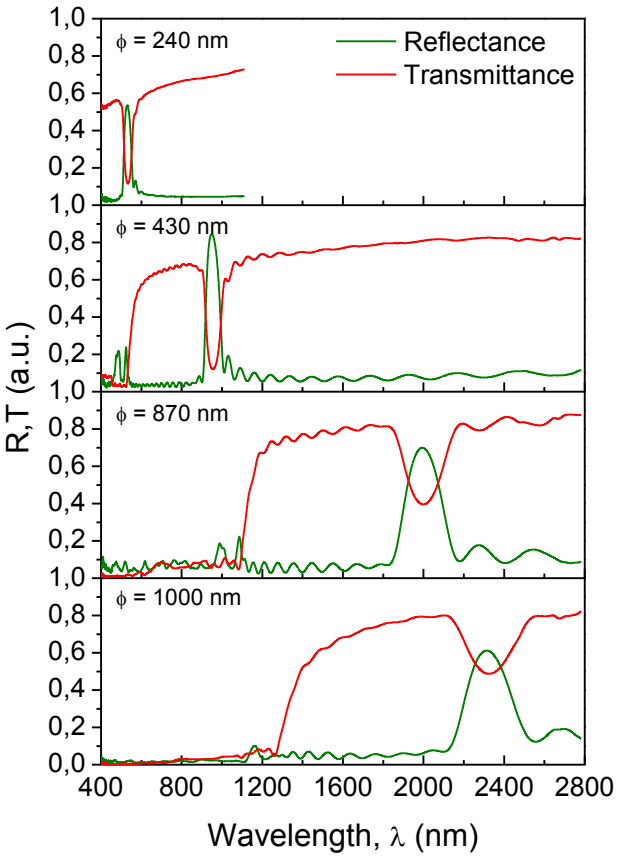

Fig. 4.17 *Optical reflectance and transmittance spectra for direct opals of 240, 430, 870 and 1000 nm PS spheres.*

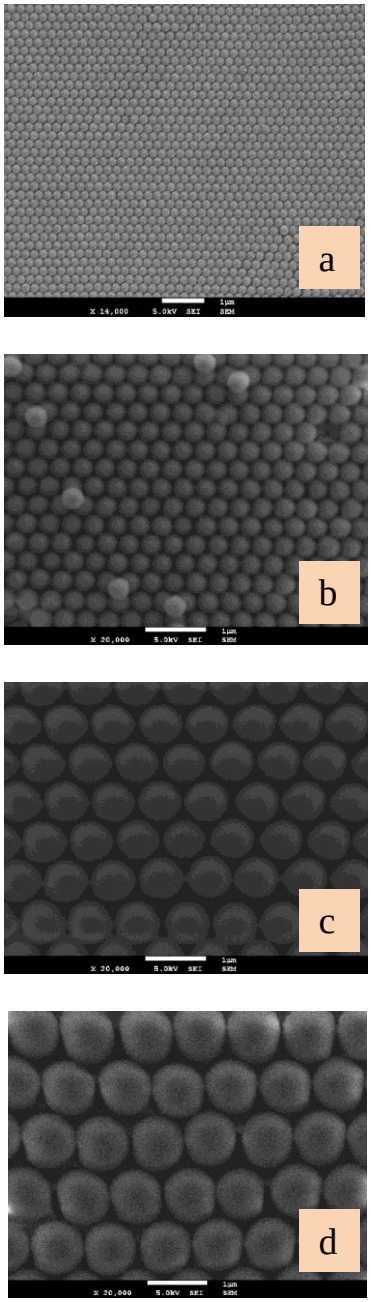

Fig. 4.18 *SEM micrographs of direct opals of 235 nm (a), 430 nm (b), 870 nm (c) and 1000 nm (d) PS spheres, made by convective self-assembly from an aqueous suspension of 0,1vol%.*

The SEM images show hexagonal packing, corresponding to the (111) plane of an FCC structure.

The most common type of structural defects in opal structures are planar stacking faults along the (111) direction. These defects are the same as reported long ago for natural opal and correspond to the various ways in which one or more hexagonal stacking sequences disrupt the cubic structure. Other types of defects include dislocations, vacancies and local distortions of the lattice originated by slightly different sized spheres.

Images taken at lower magnifications show the cracks; a tendency is observed for cracks to appear along rows of spheres, defining hexagonal patterns. A closer look into the regions at both sides of a crack shows that the crystalline orientation is the same across the crack; this had led to the belief that these cracks appear in the process of drying of the crystal, once the ordering has taken place.

A square arrangement of colloidal particles (corresponding to the (100) plane of an FCC structure) over large regions has also been observed.

In the bottom of the sample, where the growth process stops once the sample is withdrawn from the vial, can be seen how the crystal ends in an abrupt manner at an angle nearly perpendicular to the substrate. This indicates that the direction of sample growth is parallel to that of meniscus advance.

4.5 Fabrication of silica infiltrated opals

4.5.1 Co-assembly process

The co-assembly method for producing silica infiltrated PS opal films in a single step is innovative. The procedure attempted has been proposed by Hatton et al.[14].

The silica infiltrating material consists in a TEOS solution prepared by adding tetraethylorthosilicate (TEOS), hydrochloric acid (HCl, 0,10 M) and ethanol (EtOH) in the weight ratio TEOS:HCl:EtOH = 1:1:1.5, stirring for 1 h at room temperature prior to use.

In this method, the main parameters that influence the optimal growth conditions are:

- the hydrophilization of the substrate;
- the concentration of the sol-gel solution;
- the concentration of the PS nanoparticles in the suspension.

For this reason, these parameters were optimized in the process.

Substrates hydrophilization

The infiltrated opals, once produced, have to be subjected to a thermal treatment, to eliminate the PS template, giving rise to the inverse opal structure. For this reason, a silicon substrate has been used.

The interaction of the PS nanoparticles on the Si substrate has been studied, in order to achieve the best adhesion of the spheres.

Three different procedures of cleaning/hydrophilization have been tested:

- acid-base cleaning (based on Piranha solution);
- ethanol : acetone : bi-distilled water cleaning;
- RCA cleaning.

The acid-base cleaning is a procedure based on the effects of the Piranha solution.

The Piranha solution, also known as piranha etch, is a mixture of sulfuric acid (H_2SO_4) and hydrogen peroxide (H_2O_2), used to clean organic residues off substrates. Because the mixture is a strong oxidizer, it will remove most organic matter, and it will also hydroxylate most surfaces (add OH groups), making them extremely hydrophilic (water compatible). Many different mixture ratios are commonly used and all are called piranha. A typical mixture is 3:1 concentrated sulfuric acid to 30% hydrogen peroxide solution; other protocols may use a 4:1 or even 7:1 mixture.

Immersing a substrate (such as a silicon wafer) into the solution should be done slowly to prevent thermal shock that may crack the substrate material. Cleaning usually requires about 10 to 40 minutes, after which the substrates can be removed from the solution.

The effectiveness of piranha solution in removing organic residues is due to two distinct processes that operate at noticeably different rates. The first and faster process is removal of hydrogen and oxygen (as water molecules) by the concentrated sulfuric acid. This occurs because hydration of concentrated sulfuric acid is thermodynamically strongly favorable, with an ΔH of -880 kJ/mol.

The dehydration process exhibits itself as the rapid carbonization of common organic materials, especially carbohydrates, when immersed in piranha solution.

The second process can be understood as the sulfuric-acid boosted conversion of hydrogen peroxide from a relatively mild oxidizing agent into one sufficiently aggressive to dissolve elemental carbon, a material that is notoriously resistant to room temperature aqueous

reactions. This transformation can be viewed as the energetically favorable dehydration of hydrogen peroxide to form hydronium ions, bisulfate ions, and, transiently, atomic oxygen:

$$H_2SO_4 + H_2O_2 \rightarrow H_3O^+ + HSO_4^- + O \quad [4.3]$$

It is this extremely reactive atomic oxygen species that allows piranha solution to dissolve elemental carbon.

For cleaning the Silicon substrates following a procedure based on Piranha, the substrates have been firstly washed with ethanol (in the ultrasounds for 10 minutes), rinsed with bi-distilled water and dried, then immersed a 1:1 solution of $H_2SO_4 : H_2O_2$ for 1 hour and a half, then, rinsed again and dried, immersed in a 1:1:5 solution of NH_3 : H_2O_2 : bi-distilled H_2O for 1 hour and a half and rinsed and dried again with a nitrogen flux.

The ethanol : acetone : bi-distilled water cleaning consists in cleaning the substrate at first with a washing in the ultrasounds in a 1:1:1 solution of Ethanol : Acetone : Bi-D Water for 30 minutes and then putting it into a 4% solution of HF for ~5 minutes, then rinsing and drying the substrates.

The RCA cleaning is a standard set of cleaning steps of silicon wafers, which needs to be performed before high temperature processing (such as oxidation, diffusion, CVD) in semiconductor manufacturing. It involves the following :

-removal of the organic contaminants (Organic Clean);

-removal of thin oxide layer (Oxide Strip);

-removal of ionic contamination (Ionic Clean).

The wafers are prepared by soaking them in distilled water.

The first step (called SC-1, where SC stands for Standard Clean) is performed with a 1:1:5 solution of NH_4OH (ammonium hydroxide) + H_2O_2 (hydrogen peroxide) + H_2O (water) at 75 or 80 °C typically for 10 minutes. This treatment results in the formation of a thin silicon dioxide layer (about 10 angstrom) on the silicon surface, along with a certain degree of metallic contamination (notably iron) that shall be removed in subsequent steps. This is followed by transferring the wafers into a distilled water bath.

The second step is a short immersion in a 1:50 solution of HF + H_2O at 25 °C, in order to remove the thin oxide layer and some fraction of ionic contaminants.

The third and last step (called SC-2) is performed with a 1:1:6 solution of HCl + H_2O_2 + H_2O at 75 or 80 °C. This treatment effectively removes the remaining traces of metallic (ionic) contaminants.

Three standard PS opal samples infiltrated with silica have been made (with same concentrations), following the three cleaning procedures; co-assembled infiltrated opal of PS 870 nm spheres, by vertical deposition on a silicon substrate have been obtained and the optical properties have been measured by FTIR.

A comparison between the three different cleanings has been made, based on the reflectance spectra, which shows the quality of the opal and allows to choose the best cleaning procedure. Fig. 4.19 presents the reflectance spectra of opals deposited on substrates submitted to different cleaning procedures.

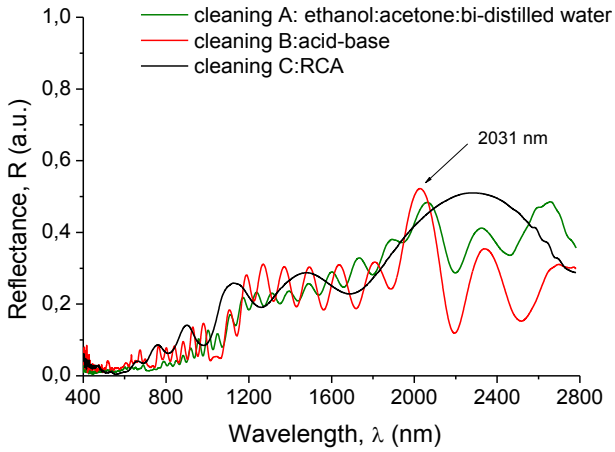

Fig. 4.19 *Reflectance spectra of co-assembled opals of PS spheres of 870 nm, made by vertical deposition on Si substrates washed with three different cleaning procedures.*

From the spectra collected, the Bragg peak is enhanced in substrates submitted to cleaning procedures A and B.

Comparing the maxima of reflectance spectra with the expected theoretical values, a blueshift of ~ 200 nm is observed. This is inherent with the changes in the effective refractive index of the composite (compared to the theoretical value expected) which is directly proportional to the decreasing of the stopband wavelength (following the modified Bragg's law). In fact, the infiltrated opal structure should be composed, as an FCC structure, of 74% of PS spheres with n=1,59 and 26% of SiO_2 with n=1,45. The amount of porosity remaining inside the matrix material and the different percentages of silica achieved during the infiltration phase can modify these ideal percentages. The presence of defects or cracks means the presence of

porosity and air in the structure and contributes with its n=1 to the mentioned effect of a overall reduction of the effective refractive index.

A silica overlayer could occur in certain areas, which contributes to the increase of the total percentage of silica in the structure and so in the reduction of the effective refractive index of the composite. These considerations will remain valid for the spectra of all the infiltrated structures.

In the opals grown on substrates cleaned with procedure C, the peak is not clearly evidenced. A possible explanation can be related to the fact that the RCA cleaning procedure do not aim surface hydrophilization; a good wettability is mandatory for the obtaining of good quality opal-based structures.

Therefore, in our work, the acid-base cleaning has been chosen. This washing treatment is necessary for achieving a correct hydrophilization of the substrate and the vial. In fact, like in the case of the glass substrates cleaning procedure (as seen in section 4.3.2), it will be carried out inside the same vials where the opals will be grown.

4.5.1.1 Optimization of the growth process

The infiltrated opals were grown in 20 ml vials containing 10 ml volume solution, for the same 4 different dimensions of PS spheres used in the self-assembling of the direct opals.
Tab. 4.4).

PS particles 200-400 nm	0.1 vol%
TEOS solution	0,7 vol %
Bi-D H_2O	99,2 vol %

Tab. 4.4 *Experimental concentrations for the first set of co-assembled opals prepared.*

Cleaned silicon substrates were vertically suspended in the vial containing the PS colloidal/TEOS suspension, using a kit illustrated in Fig. 4.20; the substrate is grab with a plastic clamp and sustained by a plastic clip, by means of a light copper wire. This configuration is adapted to allow for a sample growth over a distance of 1 cm along the vertical direction, while the lateral dimension remains fixed by the substrate width.

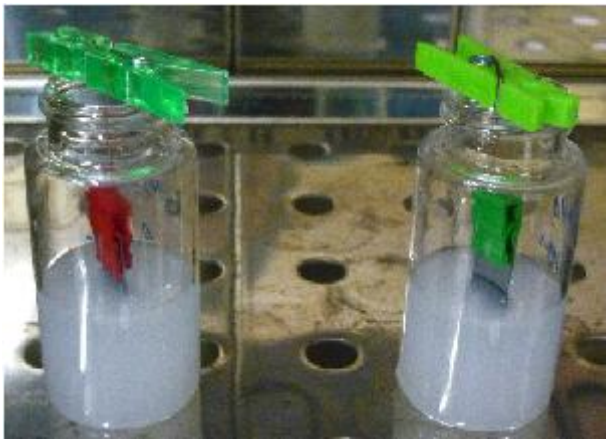

Fig. 4.20 *Kit for the growth of co-assembled opals on Si substrates.*

In Fig. 4.21 is schematized the sample growth on the substrate, which starts from the top of the sample (arrow) parallel to the meniscus moving direction. Fig. 4.22 represents a picture of a typical infiltrated opal. In general, three growth zones parallel to the liquid/substrate interface can be observed for each sample:

- the first opal film growth band (I), more thin and transparent, where the upper edge is inhomogeneous and the growth starts in a disordered way;
- the second film growth band (II), exhibiting iridescent coloring due to strong scattering effects and more uniform in thickness, nevertheless very fine cracks running parallel to the growth direction are still observed;
- finally, in band (III), the film becomes thicker and quite inhomogeneous, due to the composition changes in the suspension during the evaporation.

The band formation is determined by the colloidal concentration progressive increase during the evaporation process.

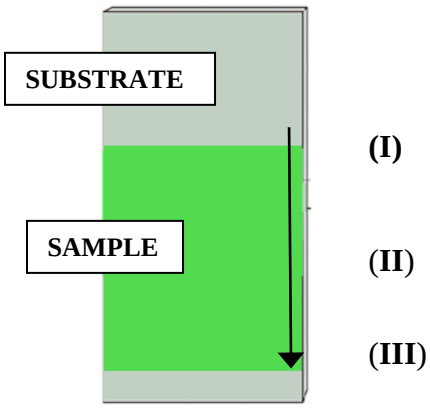

Fig. 4.21 *Schematic representation of substrate (grey) and sample (green). The vertical arrow indicates the growth direction.*

Fig. 4.22 *Picture representing the aspect of a co-assembled opal.*

Optical microscopy is a preliminary observation technique used to study and verify the quality of the structure obtained after the growth, and permits to understand quite in a clear manner how the mechanism of growth has taken place.

In its first stages, the sample grows forming terraces of increasing number of layers.

The images for infiltrated opals of PS 240 nm and 430 nm are shown in Fig. 4.23, in a sequence starting from the upper edge of the sample until the lower edge.

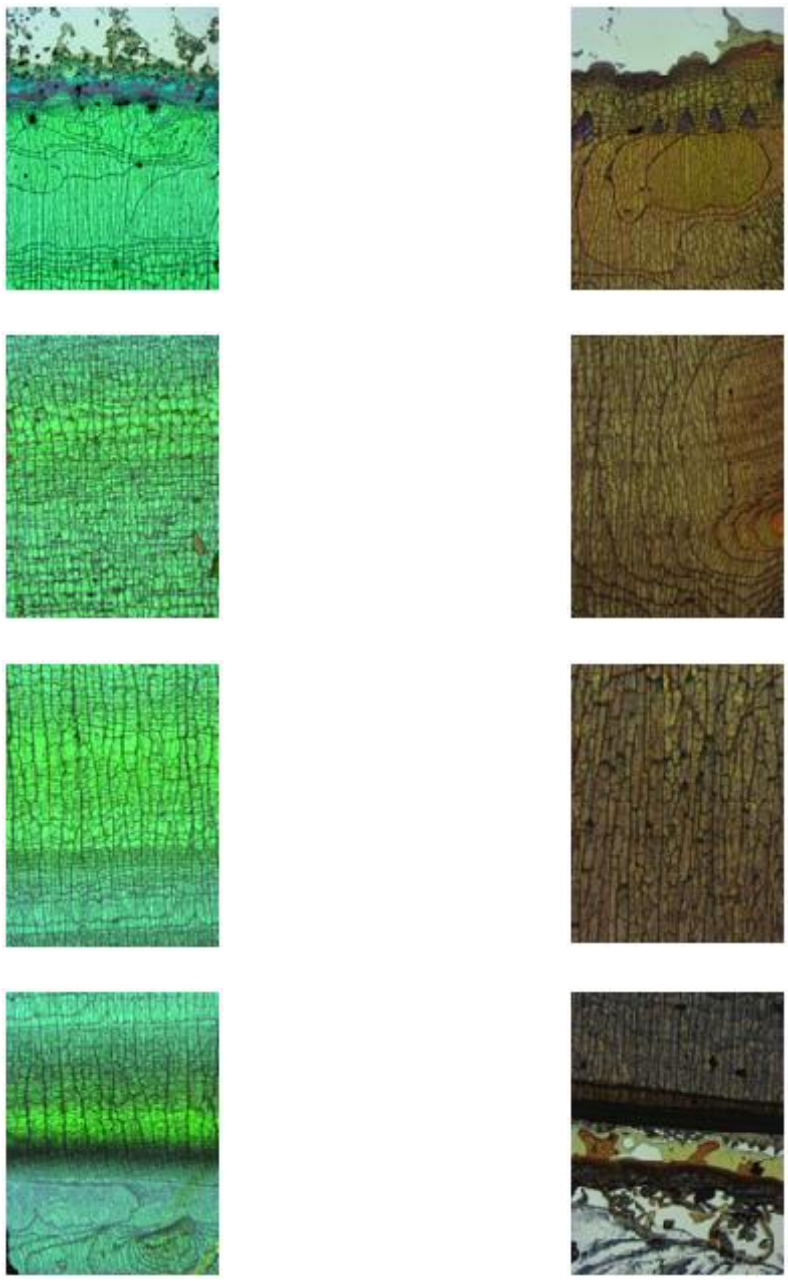

(a) *(b)*

Fig. 4.23 *Optical microscopy images of co-assembled opals of PS 240 nm (a) and PS 430 nm (b), in 4 different areas, from the upper edge to the lower edge.*

The pictures referring to the infiltrated opal made of spheres of 240 nm show a bright green color, due to the position of the Bragg peak for these structures at λ~590 nm, which is a value comprised in the green region of the VIS electromagnetic spectrum. The ones referring to the infiltrated opal made of spheres of 430 nm show a homogeneous brown color, due to the displacement of the peak towards the IR region at λ~1000 nm. The stacking of the layers of spheres may arise according to three different arrangements: face-centered cubic, hexagonal close packed, or double hexagonal close packed. Different colors correspond to different ways of packing[15]. The transmission spectra features are characteristic of the type of stacking, and, thus, each colored region observed under the optical microscope can be unambiguously associated with one of the stacking types. Regions with a constant thickness usually have dimensions of 0.5-3 mm in the growth directions and up to 1 cm in the direction perpendicular to it. As we move towards the lateral edges of the sample the morphology changes; at the edge the sample presents the same terrace-like shape as the top. As we move towards the center, the boundaries between terraces are curved, indicating the transition from the vertical behavior at the edge to the horizontal one at the center. Further, the above mentioned cracks normally curve away from the vertical towards the edge, probably due to a deformation of the meniscus at the substrate edge.

Volume effect

One trial has been made to grow opals of 240 nm PS spheres using a 20 ml volume solution, to follow literally the procedure reported by Hatton[14]. In Fig. 4.24 are presented the reflectance spectra resulting from the 10 ml and 20 ml volume, for a comparison.

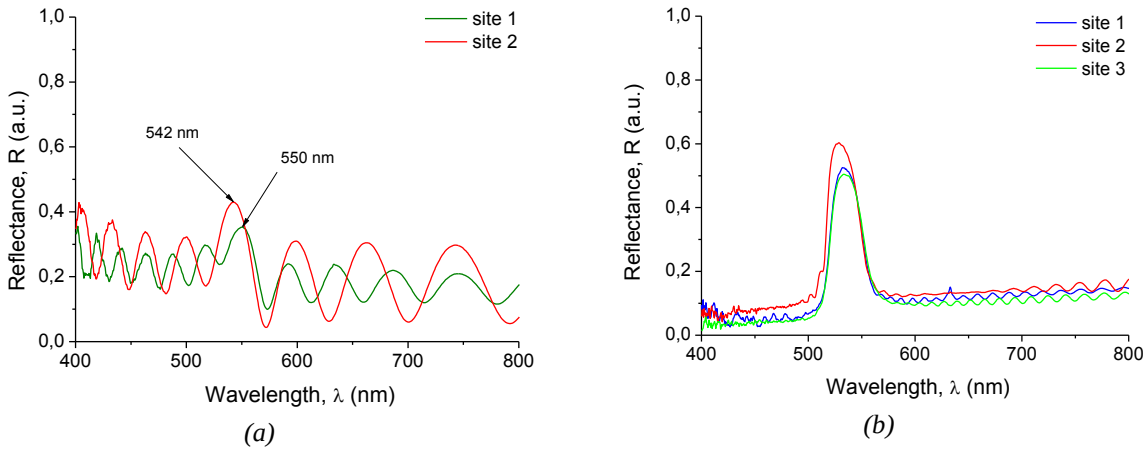

Fig. 4.24 *Reflectance spectra of a co-assembled opal of PS 240 nm spheres, made by vertical deposition on a Si substrate, in a volume solution of 10 ml (a) and 20 ml (b).*

The Bragg peak of diffraction is visible in both cases and correctly positioned at λ~540 nm, near the expected value of λ~597 nm, with a similar reflectance intensity (~0.4-0.5).
The position of this peak is independent from the thickness, while its intensity can vary with the thickness of the area where the measure is taken (as seen in section 4.3.4). Therefore, for measurements made in different sites, the position maintains and this is useful to have a confirmation of its appearance.
On the contrary, the Fabry-Pérot oscillations (Δλ) show a dependence from the thickness (*d*, distance between two reflecting surfaces) given by the following equation:

$$d = \left(\frac{\sqrt{2}\psi}{2n_{eff}}\right)\frac{\Delta\lambda}{\Delta m} \quad [4.4]$$

where *m* is the peak order. Therefore, they vary in function of the area of measurement and they result more pronounced in case of thinner areas.
The difference on the overall shape of the graphs in comparison stays mainly in the presence of Fabry-Pérot oscillations more pronounced in the 10 ml volume sample. Therefore, even if the optical results are similar, we can deduce that the two measurements have been probably made in different thickness areas. So, as operative choice, the decision is to maintain the volume of a 10 ml solution, to avoid the wasting of material without a proper significant reason.

The focus of the following phases of the research is fabricating co-assembled structures of 870 nm diameter, to serve as sacrificial colloidal templates for the inverse opal structure; for this reason, from now on, the co-assembly process for particles of bigger dimensions will be implemented.

Optimization of the infiltrating material concentration

The hydrolysis and condensation sol-gel reactions may affect the PS microspheres self-assembly. This is the reason why the experimental parameters in co-assembled opal growth have to be optimized.
The first parameter in which the optimization process has been focused on is the amount of the infiltrating material (labeled as "TEOS solution"), which will change in relation to the different dimensions of the template of spheres. This optimization phase has been made without changing the concentration of PS spheres and with the addition of different amounts of TEOS solution (Tab. 4.5).

PS particles	0,1vol%	0,1 vol%	0,1 vol%
TEOS solution	0.4 vol%	1.0 vol%	1.3 vol%
Bi-D H_2O	99.5vol%	98.9vol%	98.6vol%

Tab. 4.5 *Experimental concentrations of the opal samples prepared with different amounts of TEOS solution.*

At a first eyesight, in the sample with the less amount of TEOS solution (0.4 vol%) appears a white stripe in the lower part that divides it in two main areas; this is probably due to the lack of sufficient TEOS solution for completing the infiltration in the last phases of the evaporation process.

The reflectance spectra collected for the samples with different amount of TEOS are presented in Fig. 4.25.

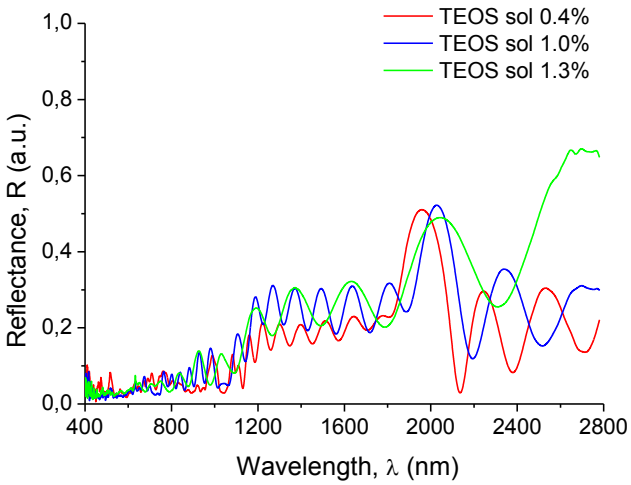

Fig. 4.25 *Reflectance spectra of co-assembled opals of PS 870 nm with different TEOS amounts.*

It is clearly noticed that the optical properties of the different samples do not differ as much as to make a quantitative comparison, being the position and the intensity of the Bragg peak similar for all the concentrations chosen. So, to make an evaluation becomes necessary the use of microscopy techniques. The SEM images (top-view) of the infiltrate opals with the lower and higher concentration of TEOS solution (0.4 vol% and 1.3 vol%) are shown in Fig. 4.26.

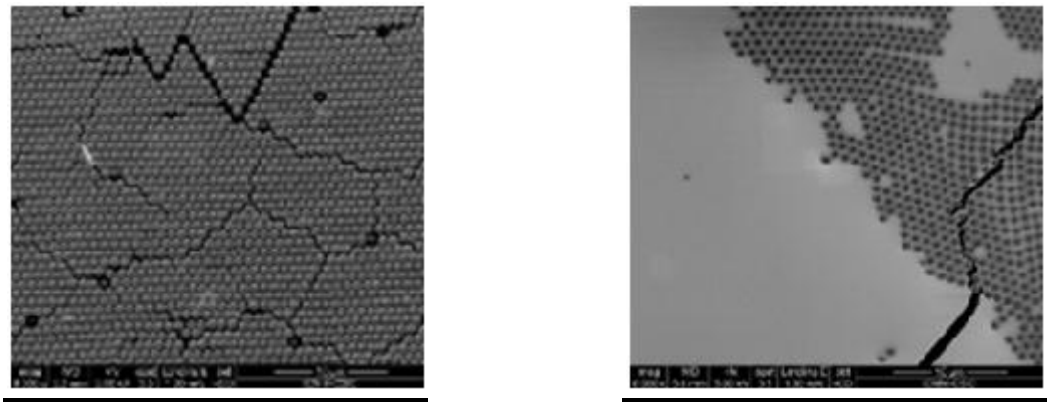

(a) *(b)*

Fig. 4.26 *SEM micrographs of co-assembled opals of 870 nm PS spheres, with 0.4 vol% added TEOS solution (a) and 1.3 vol% added TEOS solution (b).*

In Fig. 4.26 (a) the too low amount of TEOS solution causes the presence of defects and cracks, mainly positioned along the arrangement planes. On the contrary, a too large increase in the TEOS amount in Fig. 4.26 (b) leads to an over layer of silica on the PS structure that is clearly visible and that can cause the lack of signal, because the ordered structure will result hidden. The operative choice is based on the assumption that the two negative effects can be reduced in an intermediate value of concentration. In fact, the optimized range should be placed in the range between 0.7-1.0 vol% of TEOS.

After different trials, the concentration of 1 vol% TEOS is chosen, for the major reproducibility.

Optimization of process parameters

From theoretic statements, the assembly of bigger diameter particles is subjected to a stronger sedimentation competition, which can overcome the equilibrium between attraction and repulsion forces that is usually responsible of the spontaneous self-assembly.

The parameters that can influence this behavior are:

- concentration of the spheres;
- temperature and humidity of the oven;
- nature of the solvent.

Concentration of spheres

A study on the PS spheres concentration has been made, to understand how changes can occur in modifying the ratio between template material and infiltrating material. The optimization of PS spheres concentration has been made without changing the amount of the first optimized parameter chosen (TEOS solution concentration=1 vol%).

The study has started with a concentration of PS spheres=0,05 vol% and, as seen in Fig. 4.27, the optical properties give good results, in agreement with the Bragg's peak theoretical position at λ~2200 nm. The separation of the Fabry-Pérot oscillations indicate that in this measured area the thickness is reduced.

In order to increase the thickness of the sample, the concentration of 0.1 vol% has been compared and it shows similar optical properties, while a constriction of Fabry-Pérot oscillations indicates an increase in thickness. For this reason, the choice is to continue working with a concentration of 0.1 vol%.

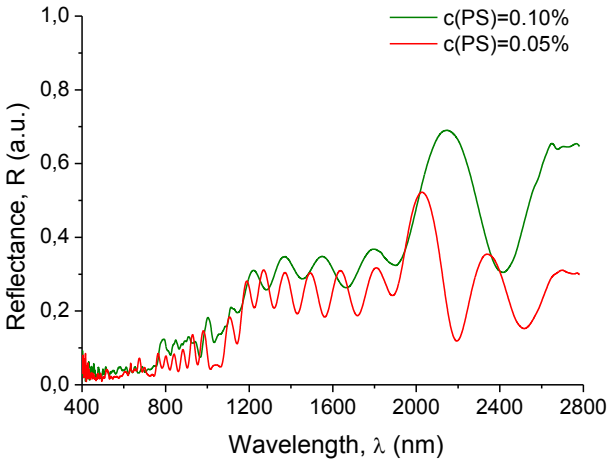

Fig. 4.27 *Reflectance spectra of co-assembled opals of PS 870 nm with different PS particles concentrations.*

Temperature

The evaporation temperature controls both the crystal growth and the particle flux rates.

An increase in temperature can be relevant for an increase in the evaporation rate of the solution, giving rapidity to the whole self-assembly process and consequently less time for the particles of bigger diameter to sediment. The optimization of temperature of growth has been made without changing the parameters already chosen (c(PS)=0.1 vol%; c(TEOS sol)=1 vol%).

In Fig. 4.28 are represented reflectance spectra for the more significant opal growths trials, carried out at 55°C, 65°C, 70°C.

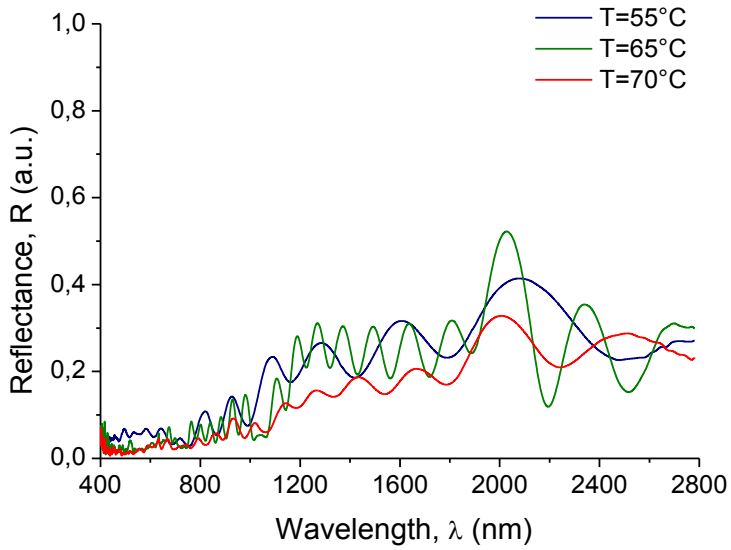

Fig. 4.28 *Reflectance spectra of co-assembled opals of PS 870 nm with different growth temperatures.*

The observation of the optical quality and the intensity of Bragg peak at 0.5 direct the choice towards the 65°C growth temperature.

With T=55°C the spheres sediment too much rapidly and also the sample is very thin, presenting regions in which the substrate is clearly visible. A too low temperature would imply a longer time scale to reach the threshold volume fraction to crystallize, so the gravity forces can predominate on the interaction forces between particles.

Humidity

A humidity study has been made, to achieve a control on the humidity conditions inside the oven. With the increase in dimensions of the particles there is the need for a more dry atmosphere; in fact, it is a more dry atmosphere that can allow a faster evaporation.

The number of samples put inside the oven at the same time is a parameter that can partially alter the humidity conditions and, for this reason, can affect the final result. The ideal condition is putting 1 sample at each time, to guarantee an uniform atmosphere, but it has been found that placing 2 samples at the same time do not alter significantly the environment. This last possibility is adopted, for a saving time compromise.

Furthermore, it was found that covering the vial with a beaker of 1 liter volume can improve the sample aesthetics quality, probably due to a slower evaporation rate.

In Fig. 4.29 are summarized the results of the whole optimization process, with the reflectance spectrum of the corresponding reference sample:

PS spheres 870 nm	0.1 vol%
TEOS solution	1.0 vol%
Bi-distilled H_2O	98.9 vol%
Temperature	65°C

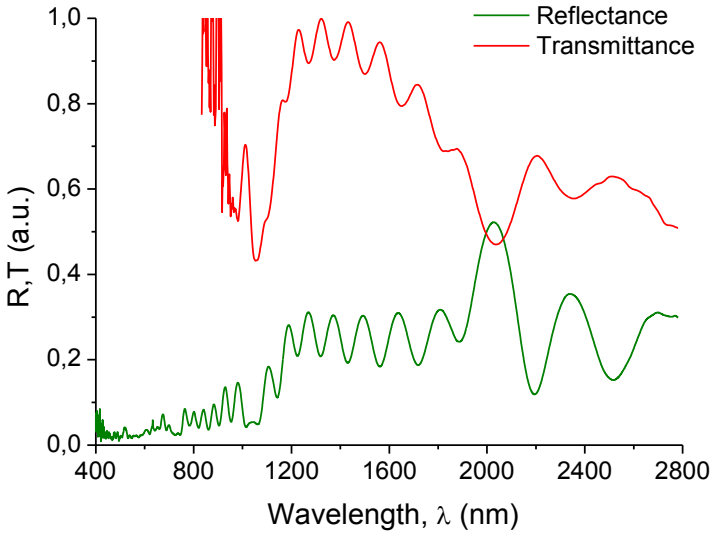

Fig. 4.29 *Optimized process parameters and optical reflectance/transmittance spectrum for the co-assembled opal of PS 870 nm spheres.*

4.5.2 Results and discussion

In the following graph (Fig. 4.30) is presented a summary of the reflectance and transmission spectra of the co-assembled samples for the dimensions of PS spheres 240, 430, 870 and 1000 nm, with corresponding SEM micrographs in Fig. 4.31.

The red-shift of the Bragg's peak can be noticed for particles of increasing diameter.

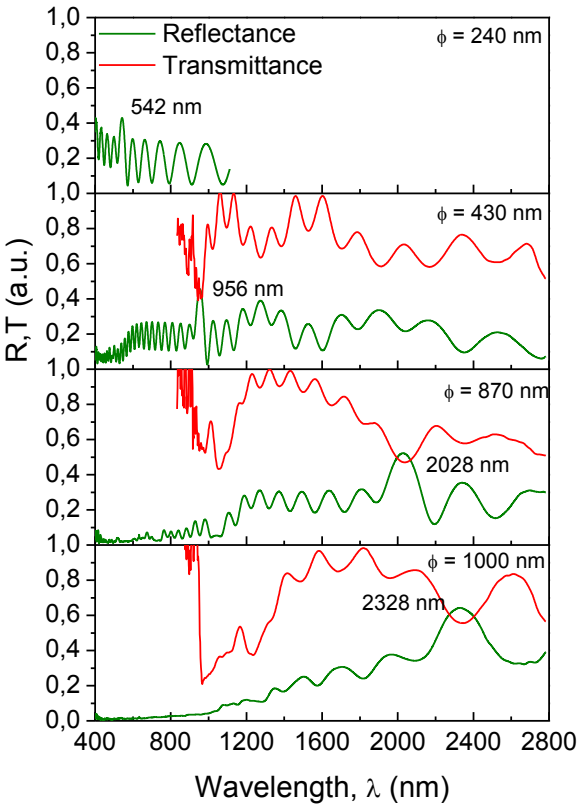

Fig. 4.30 *Optical reflectance and transmittance spectra for co-assembled opals of 240, 430, 870 and 1000 nm PS particles.*

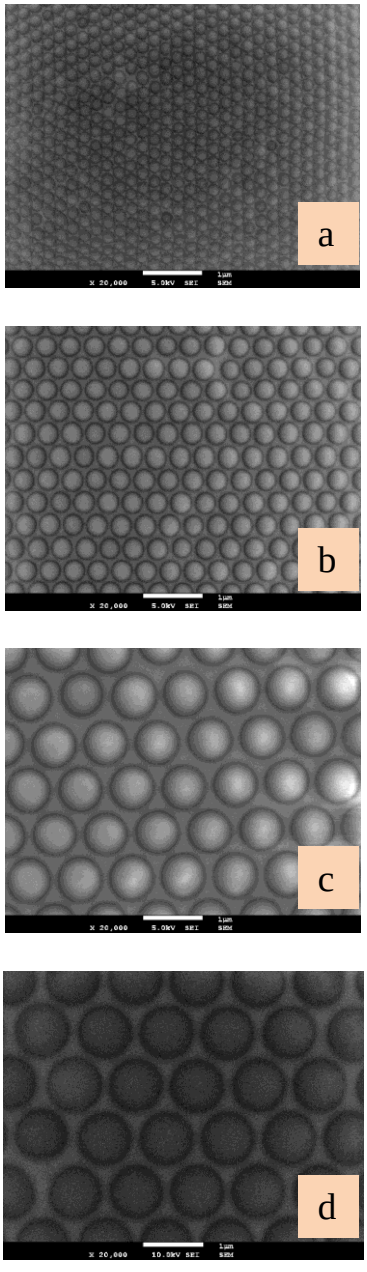

Fig. 4.31 *SEM micrographs of co-assembled opals of 235 nm (a), 430 nm (b), 870 nm (c) and 1000 nm (d) PS spheres infiltrated in a SiO_2 matrix.*

In these samples, the Bragg's peak are all placed near the theoretical value, but they are not very well defined. This is due to the low contrast between the refractive indexes of the two materials of the composite, that are closely approximates (n_{PS}=1.59 and n_{SiO2}=1.45). So, a reduction of intensity due to index-matching has to be considered.

Even in the presence of a low intensity, to demonstrate the presence of the peak, reflectance and transmission measurements have been made in the same area of the sample and their coincidence gives a confirmation about the correct position.

On the contrary, in the case of a comparison with direct opal structures (Fig. 4.17), the peaks had a very high resolution, due to the higher contrast existing between the refractive index of PS and of the air surrounding it (n_{PS}=1.59 and n_{AIR}=1.0).

With the aim of improving the deposition and adhesion of particles of big diameter, a trial to increase silicon substrate inclination inside the vial has been made, with the idea to reproduce the deposition conditions used for a glass substrate. A slice of silicon of about 1x4 cm has been cut and positioned inside the vial containing the particle suspension, with an inclination angle of ~30°.

In Fig. 4.32 are shown the results of the reflectance and transmission spectra collected for a co-assembled opal of PMMA spheres of 1 μm diameter, with this experimental set-up.

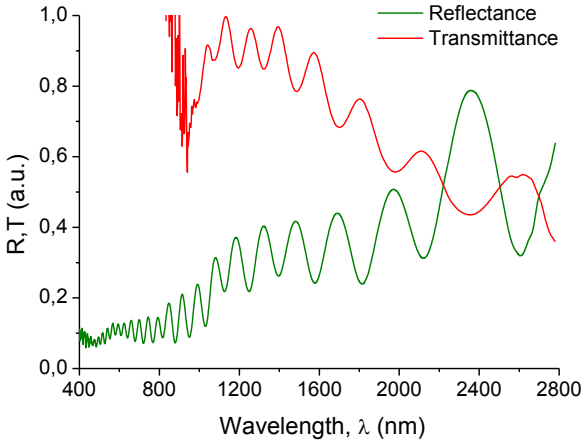

Fig. 4.32 *Reflectance and transmission spectra collected for a co-assembled opal of PMMA spheres of 1μm diameter, deposited with the substrate inclined of ~30°.*

The sample presents good aspect at eyesight and the Bragg's peak is correctly positioned, with an intensity of about 0.7. As a conclusion, it can be said that this configuration of the substrate can be a useful suggestion for the future work.

4.6 Fabrication of the inverse opals

4.6.1 Calcination process

The silica infiltrated PS opals are used to fabricate inverse silica opals. In fact, the inverse opals can be regarded as the negative replica of opals, constituted by an FCC array of micrometric spherical cavities surrounded by a higher refractive index material, in which both the cavities and the matrix material are connected throughout the structure.

The fabrication of the inverse opal was obtained by a thermal treatment carried out in a tubular oven (presented in Fig. 4.33) coupled to a PID controller, in order to remove the polymer template and partially sinter the SiO_2 structure, to obtain a consistent matrix. The graph in Fig. 4.33 (b) illustrates the different stages of the treatment; the first stage goes from room temperature up to 90°C at a rate of 2°C/min, the second maintains the sample at 90°C for 3 hours, the third goes from 90°C up to 500°C at a rate of 1°C/min and the fourth maintains this temperature for 8 hours. The cooling is programmed to reach room temperature at a rate of 5°C/min, but it is controlled by the natural inertia of the oven.

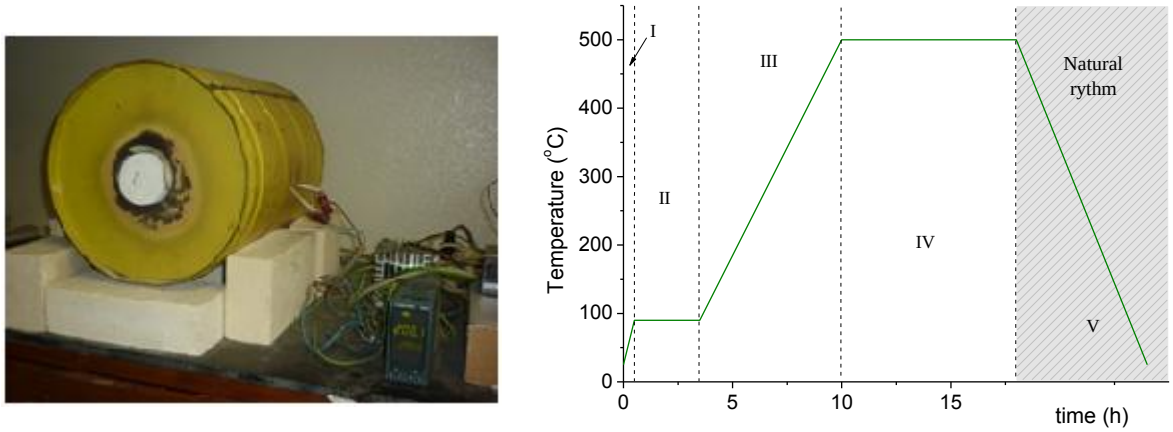

(a) *(b)*

Fig. 4.33 *Circular oven (a) and heating treatment (b) used for the calcinations of the infiltrated opals.*

At 240°C, the PS spheres start to melt, then leaving air spheres in a dielectric matrix. The release of the gas causes an increase of pressure inside the structure; that is why it is important to heat slowly, to avoid ruptures at weakest structural points.

4.6.2 Results and discussion

The graph in Fig. 4.34 reports optical reflectance spectra of the calcined opals made of PS spheres of 240, 430, 870 and 1000 nm; Fig. 4.35 shows the corresponding SEM images, that evidence the classical inverse opal structure characterized by a "holed ordered structure" interconnected by a network of material, silica in our case.

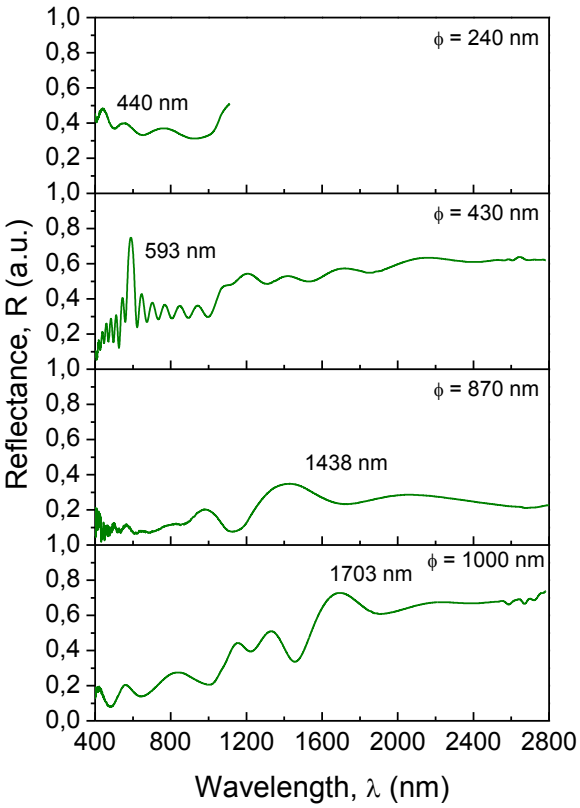

Fig. 4.34 *Optical reflectance and transmittance spectra of inverse opals made from 240, 430, 870 and 1000 nm PS spheres templates.*

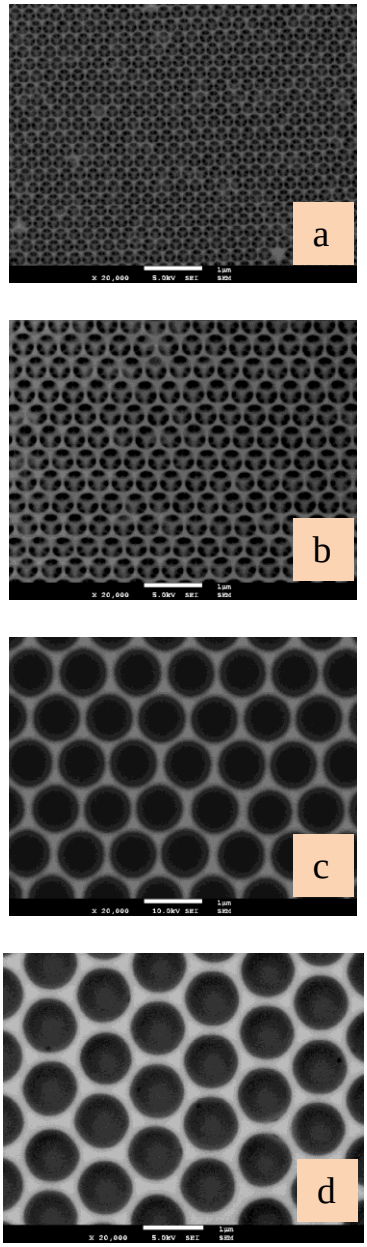

Fig. 4.35 *SEM micrographs of inverse opals made from 235 nm (a), 430 nm (b), 870 nm (c) and 1000 nm (d) PS spheres templates .*

The position of Bragg's peak is reasonably coincident with the theoretical approximations. The inverse opal structure should be composed, in theory, of 74% air and 26% of silica (assuming a maximum infiltration fraction), but the presence of some cracks increases the percentage of air inside the structure and so reduces the effective refractive index of the composite, giving proportionally, in all cases, a shift to the blue.

Although, the peak is not well resolved, even if, in principle, the increment of the contrast of index between the material of the spheres (n_{AIR}=1) and the matrix material (n_{SiO2}=1.45) should give a better resolution in the diffraction phenomena. After the heating treatment, the reduction of the photonic band intensity is due to a sum of different factors, mainly present localized states and a given amount of undesirable defects (like voids, stacking faults) that may contribute to the reduction of an existing photonic pseudo gap, turning the density of electromagnetic modes inside to a non-zero value. On the other hand, propagation in allowed bands cannot be simply described by means of Bloch modes having a well defined propagation direction, due to the presence of incoherent scattering[16].

A shrinkage of the spheres occurs during the sintering process, simultaneously to the elimination of the PS decomposition gases. Moreover, the sol-gel silica matrix will eliminate water and other liquid reactants still present inside the matrix gel. Following the Bragg's approximation, this reduction implies a further blue shift in the FTIR spectra.

To estimate the average reduction of the diameter of spheres during the heat treatment, a statistical comparison has been made, using SEM images of the infiltrated and inverse opal structures, for the spheres of bigger dimension (1 μm). The statistical curves are presented in Fig. 4.36.

The curve relative to the infiltrated opal shows a distribution of the diameters of the spheres around the value of 1,01 μm, while the one referring to the inverse opal around the 990 nm. It can be correctly affirmed that the treatment caused a reduction of ~2% in the average dimension of the spheres and it is an acceptable value, because in literature is reported that shrinkage values until ~10% are possible to occur.

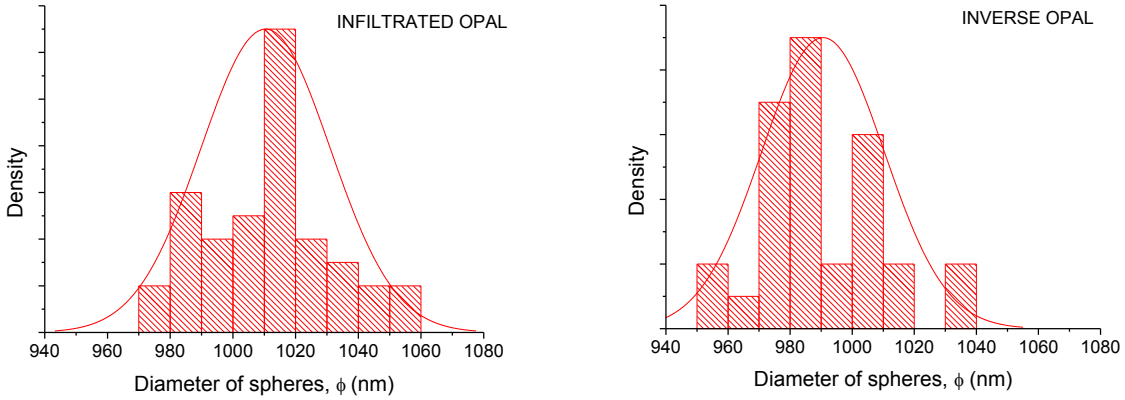

Fig. 4.36 *Approximated Gaussian curves used to evaluate the reduction in the diameter of the spheres in a PS template of 1 µm after the thermal treatment.*

Nevertheless, in many cases, a sufficiently good quality of the structure is maintained after the thermal treatment. Optical microscopy images are used to prove this assumption, referring to a comparison between an infiltrated opal of PS spheres of 1 µm (Fig. 4.37) and the calcined one (Fig. 4.38).

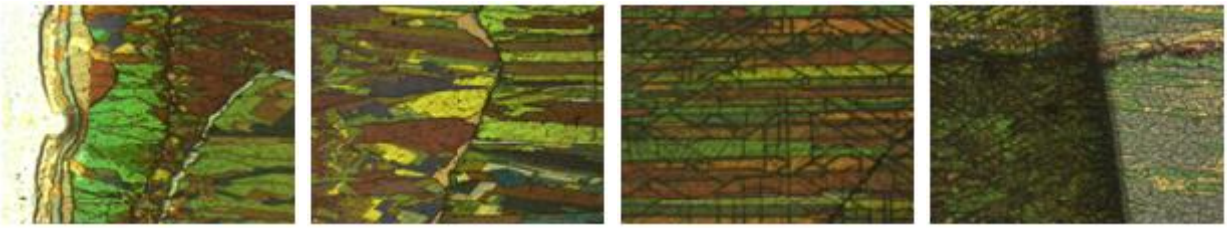

Fig. 4.37 *Optical microscopy images of PS 1µm co-assembled opal, in four different areas of the sample, from the upper edge to the lower edge, starting from the left.*

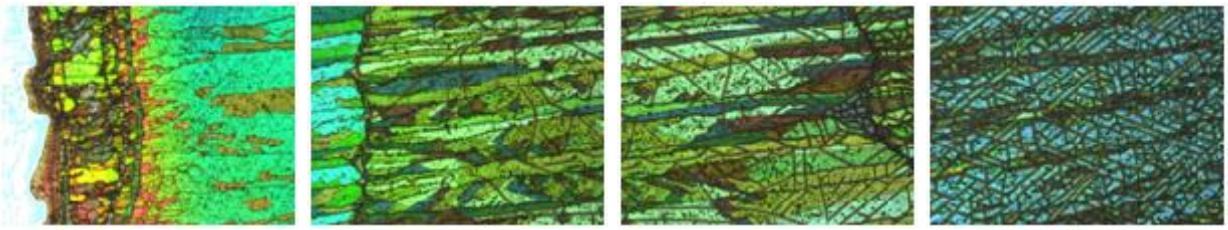

Fig. 4.38 *Optical microscopy images of PS 1µm inverse opal, in four different areas of the sample, from the upper edge to the lower edge, starting from the left.*

In the infiltrated opal of Fig. 4.37, arranged colored domains are clearly visible. The central part of the sample shows a relevant thickness and, in the final part, cracks appear as dark lines, arranged in a triangular pattern. They show an unexpected, unique orientation along

(110) planes of the colloidal crystal and develop during the co-assembly of colloids with the silica gel, therefore reflecting the unique fracture mechanism of a more complex, composite opal/matrix system.

A transition between the area with silica gel to the area without it is clearly seen in the image on the right; the reason stays in the increasing on refractive index contrast from the structure of PS spheres in a silica matrix to the one of PS spheres in an air matrix.

In the inverse opal of Fig. 4.38, the arranged and colored structure is still observed; the difference is an increase in the amount and distribution of cracks, mainly along triangular patterns. However, the presence of iridescent and ordered domains are sufficient to assert the maintenance of a good quality structure.

In Fig. 4.39 we summarize the different steps run to achieve the silica inverse opal, starting from a template of 870 nm PS colloidal particles.

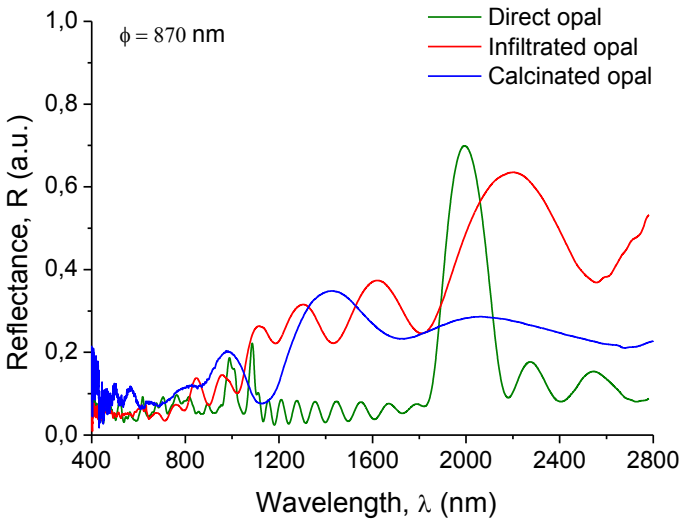

Fig. 4.39 *Comparison between optical reflectance spectra of direct, infiltrated with silica and inverse opal of 870 nm PS spheres.*

The Bragg peak moves of a redshift for the increase in the effective refractive index of the composite, when the template of PS particles is infiltrated with silica, and of a blueshift of ~1000 nm after the removal of the template. The reduction in quality is related to the different steps underwent by the opal, which increase the amount of defects in the structure.

4.7 Fabrication of porous silicon inverse opals

4.7.1 Magnesiothermic reduction

In order to fabricate an inverse opal structure with an index contrast sufficiently high to produce a complete photonic band gap, the silica matrix obtained needs to be converted into a non porous silicon one, as seen in theoretical calculations presented in section 4.2.

To achieve this, a carbothermal reduction of silica into silicon would require the use of temperatures well above the silicon melting point (≥2000°C) and the use of an electrochemical reduction in molten salts would produce silicon products that do not retain the micro scale morphology of the starting silica. Thus, another innovative method, demonstrated by Sandhage et al.[17], is a low-temperature (650°C) magnesiothermic reduction process, implemented for converting 3D nanostructured silica micro-assemblies into micro porous nanocrystalline silicon, preserving the complex shape of the silica template, although with the introduction of nanometer-scale pores.

The use of this method, followed by a Deposition in Chemical Vapor (CVD), has already been tested with opal films and has enabled to obtain opals formed by monodisperse silicon spheres[18].

Magnesium vapor in the presence of silica reacts according to the following reaction, spontaneous at temperatures above the melting point of magnesium:

$$SiO_2(s) + 2Mg(g) \rightarrow Si(s) + 2MgO(s) \quad [4.5]$$

The magnesia is then removed quickly with an acid solution, to leave only traces of silica and structured silicon.

In the present work, the reduction process has been conducted inside a dedicated stainless steel reactor, composed of two hollow chambers separated with CF format flanges (showed in Fig. 4.40), sealed under an Argon atmosphere in a glove bag.

A ~0.5 cm^2 silica inverse opal film has been placed into one chamber (with an inner volume of ~3 cm^2) and ~3 mg of Mg was placed in the other chamber, about 1 cm away from the sample. After being hermetically closed, it was introduced into a furnace to generate Mg vapor and then submitted to a thermal treatment (Fig. 4.41), to remove all the silanol groups present in the silica matrix.

(a) *(b)*

Fig. 4.40 *Reactor used for the magnesiothermic reduction in the different phases of the process: introduction of Mg powder and the opal sample in controlled atmosphere (a); thermal treatment (b).*

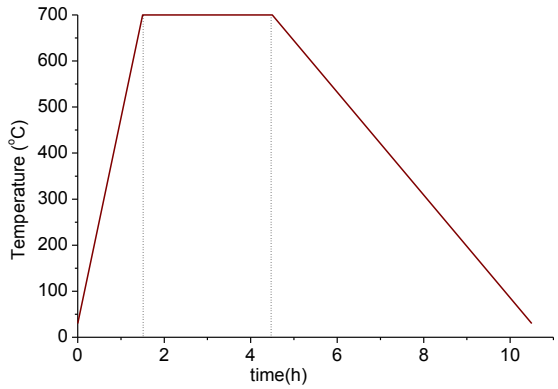

Fig. 4.41 *Temperature/time profile for the magnesiothermic reduction process.*

The Si-MgO inverse opal produced was then immersed in an HCl solution (1M) and soaked for 4 h, to remove magnesia by a selective etching and to leave an inverse opal structure of porous Si. The final material resulting is pure polysilicon with mesostructured pores.

After the selective etching with HCl, a qualitative and quantitative elemental analysis with the Energy Dispersive X-ray Spectroscopy (EDS) (Fig. 4.42) was made to confirm the success of the etching process.

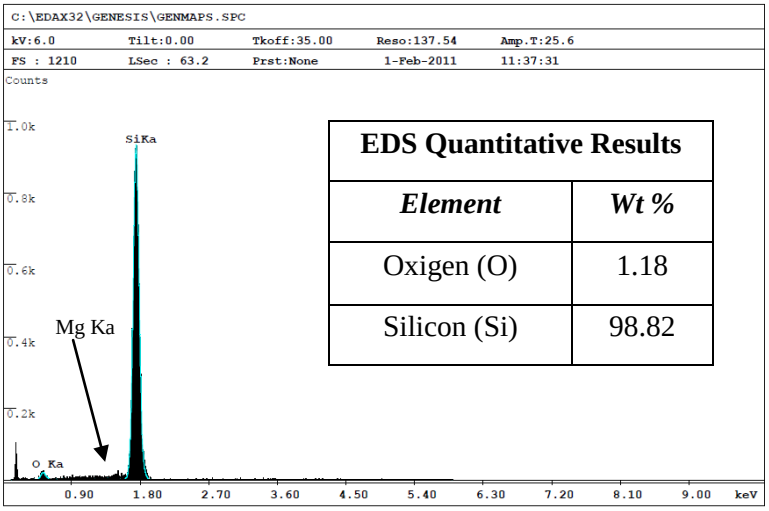

EDS Quantitative Results	
Element	***Wt %***
Oxigen (O)	1.18
Silicon (Si)	98.82

Fig. 4.42 *EDS qualitative and quantitative result (illustrating the K series peaks, according to the atomic number of the atom of X-Ray origin, and the wt% of the elements) after the selective etching of magnesia in the Si-MgO inverse opal.*

As can be seen, effectively, the removal of magnesia results to be complete; the Si quantity is in percentage much higher face to the O (98.82 wt%) and the position of Mg in the EDS spectrum is indicated by an arrow.

4.7.2 Results and discussion

The SEM images presented confirm that, after the thermal treatment at 700°C and the etching of MgO with HCl, the structure maintains the order and periodicity.

The profile images in Fig. 4.43 show clearly the typical FCC structure and the different possible planes of fracture (e.g. triangular, squared).

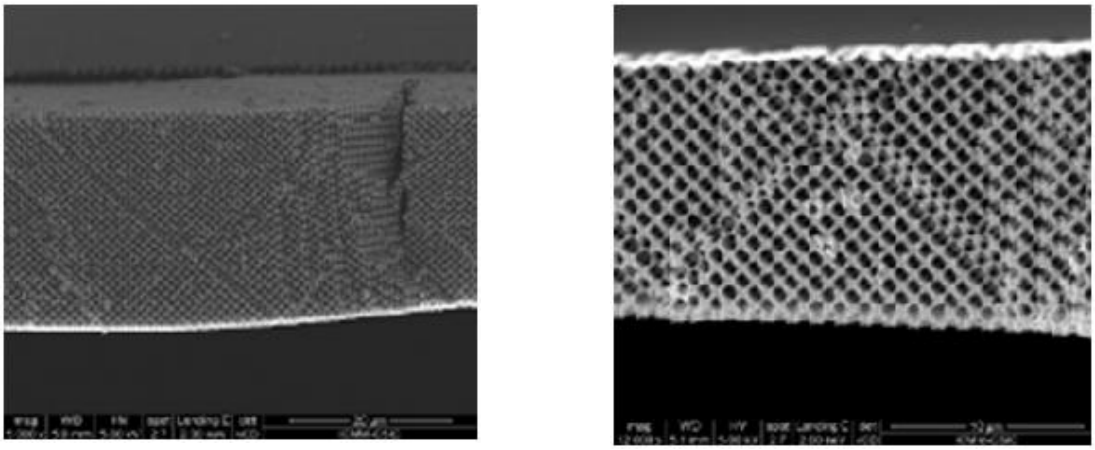

Fig. 4.43 *SEM micrographs of an inverse opal of PS 870 nm after magnesiothermic reduction (profile view), at two different magnifications.*

Top views (Fig. 4.44) show the porosities (white points) inside the silica matrix, due to the removal of the MgO by HCl. The black points inside the spheres represent the points of contact between spheres which composed the template 3D structure.

The magnesiothermic reduction process induces a decrease of the air sphere diameter, due to the inclusion of MgO in the structure. Therefore, the slight modification of size implies some strain, but the overall structure and the optical quality are preserved.

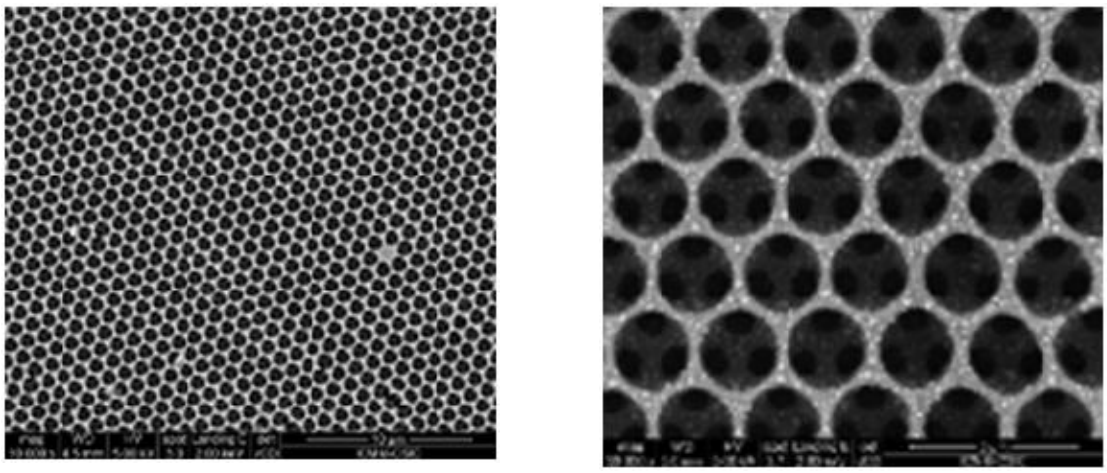

Fig. 4.44 *SEM micrographs of an inverse opal of PS 870 nm after magnesiothermic reduction (top view), at two different magnifications. The porosity inside the silicon matrix can be noticed.*

The optical properties of the porous silicon inverse opal obtained have been studied, as usual, by reflectance measurements, at near-normal incidence, and the results are showed in Fig. 4.45. The spectra show that, after the process of magnesiothermic reduction, the Bragg peak suffers of a redshift of about 300 nm, due to the higher refractive index of the composite constituted by Si and MgO, and then, after selective etching of MgO (equivalent to a refractive index decrease), moves in a blueshift. A total displacement of the Bragg peak of about 72 nm can be evaluated; in fact, the silica inverse opal spectrum showed a peak centered at 1236 nm, corresponding to the first photonic pseudo gap opening at point L of the Brillouin zone, and the porous silicon inverse opal spectrum shows a peak centered at 1308 nm. Fabry-Pérot oscillations are evidenced on the left and right sides of the Bragg's peak, due to the fact that the opal sample is relatively thin.

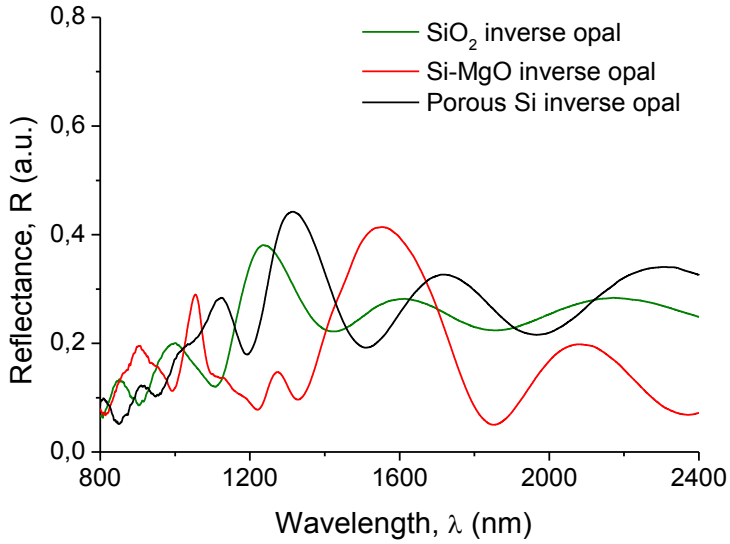

Fig. 4.45 *Comparison between optical reflectivity spectra of an inverse opal of PS 870 nm: SiO_2 structure after calcination, Si-MgO structure after magnesiothermic reduction, porous Si structure after removal of magnesia with HCl.*

The agreement of the total displacement value (~72 nm) with the one calculated by the modified Bragg's law approximation (~171 nm) is quite good, because the real position of the peaks normally is related to the presence of different amounts of porosity, which are variable in the different steps of the process and not controllable in an ideal theoretical approximation. As for the theoretical calculations, a 100% efficiency on the silica reduction is assumed.

4.8 Fabrication of non-porous silicon inverse opals

4.8.1 Chemical Vapor Deposition

The nature of the porous silicon (p-Si) inverse opal involves a refractive index lower than the non porous silicon (np-Si) one.

Our objective requires high refractive index materials, to achieve the threshold for the formation of a full photonic band gap inside the structure. Then, to increase the refractive index, the p-Si inverse opals have been treated by Chemical Vapor Deposition (CVD) to infill the pores of the Si matrix. The installation used is shown in Fig. 4.46.

Fig. 4.46 *Chemical Vapor Deposition (CVD) installation.*

Polycrystalline silicon is deposited from disilane precursor (Si_2H_6) (Sigma Aldrich), using the following reaction: $Si_2H_6 \rightarrow 2Si + 3H_2$ [4.6]

The deposition contemplates a vacuum of $8.6 \cdot 10^{-6}$ mbar and the value of the precursor opening pressure is 38 kPa. After the condensation of the disilane vapor on the substrate introduced in the ampoule (the p-Si inverse opal), the ampoule is moved and put inside an heating chamber, where the sample is heated at 325°C in 30 minutes and let at this temperature for 12 hours.

4.8.2 Results and discussion

The CVD process has the aim of progressively infilling the pores of the porous silicon inverse opal structure. The SEM image presented in Fig. 4.47 confirms that, after the deposition phase, the structure maintains the order and periodicity; in some cases, with the vapor penetration, the closure of the holes remaining from the 3D connections between spheres can be observed. It is important to not damage the interconnected structure with a too high deposition, because it would mean a loss in the peculiar resonance properties.

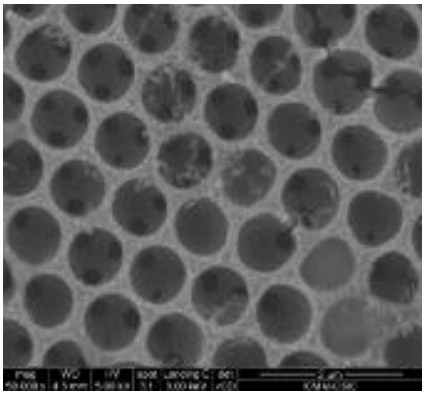

Fig. 4.47 *SEM micrograph of a np-Si inverse opal of PS 870 nm after CVD process.*

The optical characterization of the non-porous silicon inverse opal obtained has been studied by reflectance measurements, at near-normal incidence (Fig. 4.48).

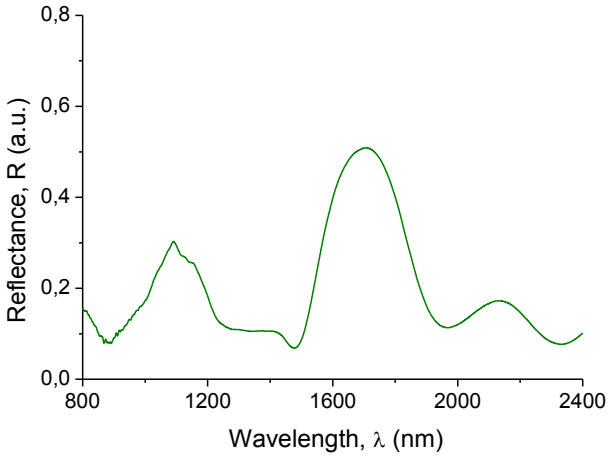

Fig. 4.48 *Optical reflectance spectra of a PS 870 nm np-Si inverse opal.*

The spectrum shows the Bragg peak in a range of wavelengths centered in 1,6 μm; it moved of a redshift of ~400 nm from the previous porous silicon one. Therefore, the position of the peak, placed at lower wavelengths than in the case of a theoretically non-porous silicon matrix, and the calculus of the n_{eff} of the composite =1.20 (lower than n_{eff}=1.98), lead to state that some porosities stayed after the CVD.

These results conduct to some considerations.

Original idea was to obtain a non-porous silicon inverse opal with stopband centered at 2,6 μm and reflectance high energy bands at 1,54 μm, so that to achieve the threshold value of refractive index contrast >2.9 as to open a full photonic band gap.

The results obtained open the possibility of considering the stopband of the silicon inverse opal still with some porosities, after CVD, centered at 1.54 μm. In this case, the refractive index contrast is lower, due to the porosities inside the composite, sufficient only to achieve a pseudo gap in the Γ-L direction.

This pseudo gap can be exploited, even if also more deposition cycles can be applied to increase the index; the greater the number of CVD cycles, the greater the risk of closing the interconnected channels, damaging the structure.

4.9 Conclusions

The fabrication and characterization of artificial opal structures has given these results:

- Synthesis of **silica infiltrated opals** of good quality by co-assembly:

the optimization of the innovative co-assembly process for the growth of silica infiltrated opals, using PS spheres of bigger diameter (0.8-1 μm) has conducted to good quality composite nanostructures, exhibiting iridescence and Bragg diffraction properties.

- Fabrication of **silica inverse opal** nanostructures:

the thermal treatment carried out for the calcinations of the co-assembled silica infiltrated opals has allowed the fabrication of silica inverse opals which maintain sufficiently good optical properties of Bragg diffraction.

- Fabrication of **silicon inverse opal** nanostructures:

after the magnesiothermic reduction, while still presenting some porosities which influence the position of the Bragg peak, the inverse structure of silicon was found to be fairly good.

In Fig. 4.49 is reported an overall comparison between the reflectance spectra of the opal-based structures in all the processing phases.

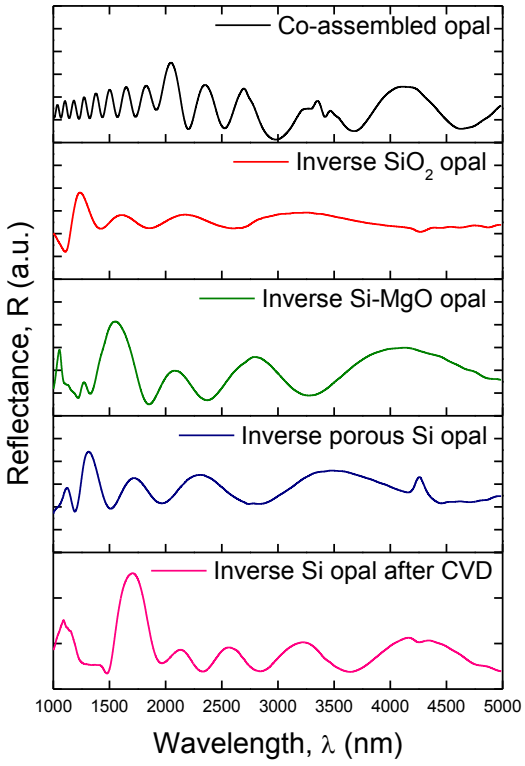

Fig. 4.49 *Comparison of optical reflectance spectra for the different steps towards a np-Si inverse opal.*

Some considerations have to be made about the difficulties in the reproducibility of results; these processes, in fact, do not require specific equipments to be made but, being spontaneous, are very sensitive to all environmental variables.

For this reason, even if a correct implementation of the process using the same working conditions has been made, still a lot of work must be done before addressing to a mass production.

References

1 Gonçalves, C. M., Fortes, L. M., Almeida, R. M., Chiasera, A., Chiappini, A. & Ferrari, M. *3-D rare earth-doped colloidal photonic crystals*, Optical Materials, 31, 9 (2009) 1315-1318.

2 Kim, S.-H., Kim, S.-H., Jeong, W. C. & Yang, S.-M. *Low-Threshold Lasing in 3D Dye-Doped Photonic Crystals Derived from Colloidal Self-Assemblies*, Chemistry of Materials, 21, 20 (2009) 4993-4999.

3 Montes, Á. B. *Cristales fotonicos opalo-semiconductor* Doctorado en Ciencias Físicas thesis, Universidad Autónoma de Madrid (2001).

4 Ashcroft N.W., M. N. D. *Solid State Physics*, (Thomson Learning, 1979).

5 Lau, W. S. *Infrared characterization for microelectronics*, (World Scientific, 1999).

6 Galisteo-Lopez, J. F., Palacios-Lidon, E., Castillo-Martinez, E. & Lopez, C. *Optical study of the pseudogap in thickness and orientation controlled artificial opals*, Phys Rev B, 68, 11 (2003).

7 Bertone, J. F., Jiang, P., Hwang, K. S., Mittleman, D. M. & Colvin, V. L. *Thickness Dependence of the Optical Properties of Ordered Silica-Air and Air-Polymer Photonic Crystals*, Phys Rev Lett, 83, 2 (1999) 300.

8 <http://cnx.org/content/m25495/1.2/>.

9 <http://cnx.org/content/m25737/latest/>.

10 Niinistö, L., Päiväsaari, J., Niinistö, J., Putkonen, M. & Nieminen, M. *Feature Article: Advanced electronic and optoelectronic materials by Atomic Layer Deposition: An overview with special emphasis on recent progress in processing of high-k dielectrics and other oxide materials*, physica status solidi (a), 201, 7 (2004) 1375-1375.

11 Gonçalves, M., Brás, J. & Almeida, R. *Process optimization of sol–gel derived colloidal photonic crystals*, Journal of Sol-Gel Science and Technology, 42, 2 (2007) 135-143.

12 Wong, T.-S., Chen, T.-H., Shen, X. & Ho, C.-M. *Nanochromatography Driven by the Coffee Ring Effect*, Analytical Chemistry, 83, 6 (2011) 1871-1873.

13 Tan, K. W., Koh, Y. K., Chiang, Y.-M. & Wong, C. C. *Particulate Mobility in Vertical Deposition of Attractive Monolayer Colloidal Crystals*, Langmuir, 26, 10 (2010) 7093-7100.

14 Hatton, B., Mishchenko, L., Davis, S., Sandhage, K. H. & Aizenberg, J. *Assembly of large-area, highly ordered, crack-free inverse opal films*, Proceedings of the National Academy of Sciences, 107, 23 (2010) 10354-10359.

15 Checoury, X., Enoch, S., Lopez, C. & Blanco, A. *Stacking patterns in self-assembly opal photonic crystals*, Appl Phys Lett, 90, 16 (2007).

16 Li, Z.-Y. & Zhang, Z.-Q. *Fragility of photonic band gaps in inverse-opal photonic crystals*, Phys Rev B, 62, 3 (2000) 1516.

17 Bao, Z. H. *et al. Chemical reduction of three-dimensional silica micro-assemblies into microporous silicon replicas*, Nature, 446, 7132 (2007) 172-175.

18 Ibisate, M., Golmayo, D. & López, C. *Silicon Direct Opals*, Advanced Materials, 21, 28 (2009) 2899-2902.

Chapter 5

Doping procedures in opal-based photonic crystals

5.1 Introduction

The composite structures fabricated and discussed in the previous chapter have been studied with the final aim of controlling and enhancing the spontaneous emission inside a so obtained periodically ordered structure, with a structured photonic band gap.

To achieve this, the exploitation of the luminescence properties of emitters such as rare earth (RE) ions (Er^{3+}; Yb^{3+}) has to be optimized, and the focus is on the region around erbium emission at 1,54 μm.

This chapter deals with the first trials of introduction by co-assembly and by Atomic Layer Deposition of these RE ions inside an infiltrated opal and inside an inverse opal and the understanding of the effects made by this incorporation on the nanostructure.

5.2 Rare earth co-doped artificial opals by co-assembly

The introduction of the RE ions inside the inverse opal structure has been made following a sol-gel route.

The innovation stays on the use of the implemented co-assembly method also in the doping phase; the co-assembled method, in fact, is a promising route to have the incorporation of the RE ions directly inside the forming silica network. A dissolution of the RE ions inside the silica by sol-gel route would imply, from the beginning, a more homogeneous dispersion of the emitter ions inside the silica infiltrating material. Then, after the co-assembly and the removal of the template, it would allow the obtaining of an inverse opal with an already activated silica structure.

Thus, doping ions will be added to the TEOS solution, which is added to the aqueous suspension of colloidal polymer particles in water, and the growth of infiltrated co-doped silica opals will be carried out in a one step procedure. The maximum doping level (molar percentage) in silica host matrix is reported to be 1 mol% for Erbium and 7,5 mol% for Ytterbium, before quenching phenomena[1].

Also here, a thermal treatment will be needed to obtain the inverse opal.

Choice of the Erbium precursor

To make the correct choice of the erbium precursor, silica films were doped with Er salts belonging to different precursors and were deposited on bare silicon substrates. The idea is to understand which precursor gives the best RE dispersion in the silica matrix, thus allowing a higher PL efficiency.

In detail, three TEOS solutions (solution of 1:1:1.5 (ratio in grams) of Tetraethyl Orthosilicate (TEOS):Hydrochloric Acid (HCl):Ethanol (EtOH), as referred in Chapter 4) have been prepared and stirred for 45 min at room temperature.

Different erbium precursors have been added to each pre-hydrolized TEOS solution (1 mol%, considering the TEOS molar amount as 100%): ErF_3 (99.9%, Sigma-Aldrich), $ErCl_3$ (99.9%, Sigma-Aldrich), $Er(NO_3)_3 \cdot 5H_2O$ (99.9%, Sigma-Aldrich).

The doped sol-gel solutions have been stirred with ultrasounds still for 15 minutes, to reach the complete dissolution of the RE; after this time, at naked eye, the dissolution was completed.

Three different solutions have been deposited on a substrate, and then heat treated at 1000 °C for 1 hour. This heat treatment was carried out in order to promote a more complete condensation and densification of the silica matrix and also for the removal of -OH groups, which are mandatory for an efficient emission of the RE, because they could quench the emission of the dopants. In fact, it is known that free-OH groups, whose fundamental vibration ranges between 2500 and 3600 cm^{-1}, are one of the dominant quenching centers in Er^{3+} doped glasses[2]. From the analyses of the total decay rate of the $^4I_{13/2}$ level of Er^{3+}, it was confirmed that the OH groups can cause concentration quenching of 1.5 μm band emission.

Since the energy gap between the $^4I_{13/2}$ and $^4I_{15/2}$ levels (6500 cm^{-1}) approximately corresponds to the energy of overtone of the free-OH stretching vibration, nonradiative relaxation from $^4I_{13/2}$ can occur when an Er^{3+} ion is coupled to a OH group.

Moreover, the 1100°C temperature is advised to obtain the SiO_2 densification, with the complete removal of water and the creation of network structure in which the erbium ions are encapsulated.

Photoluminescence spectroscopic measurements were performed in NIR upon excitation at 514.5 nm with the excitation power of ~500 mW, and the spectra obtained in Fig. 5.1 show the $^4I_{13/2}$ and $^4I_{15/2}$ transition of the trivalent erbium ion.

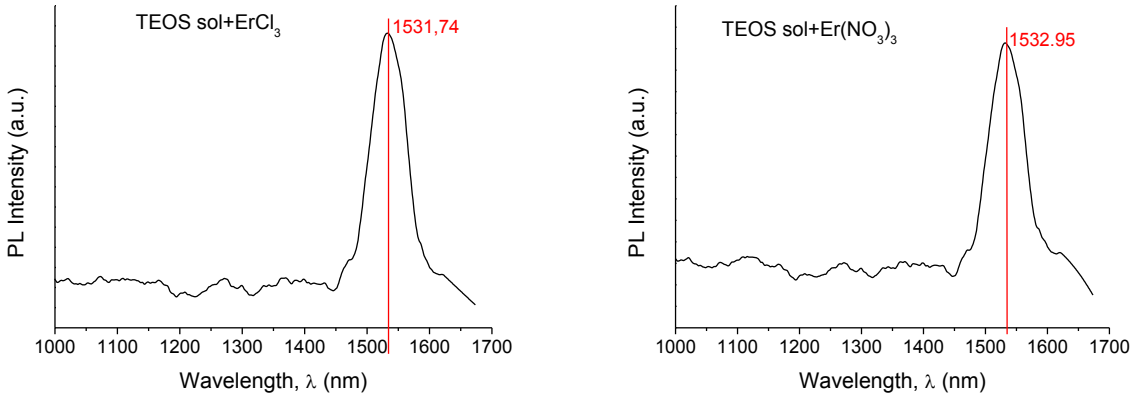

(a) *(b)*

Fig. 5.1 *Photoluminescence spectra for different Erbium precursors inside the silica host matrix: $ErCl_3$ (a) and $Er(NO_3)_3$ (b).*

Similar PL results have been obtained for two different precursors, $ErCl_3$ and $Er(NO_3)_3{\cdot}5H_2O$, which exhibit the main emission peak of Er situated in a wavelength of 1532 nm, as expected.

Incorporation of Er from the ErF_3 precursor did not evidence the presence of a PL peak; probably the reason is that this kind of precursor presents very low solubility in acid environment.

Considering the acid environment in the present sol-gel process (H^+; Cl^-), the presence of the same kind of ions could probably allow better short distance interactions, between the PS/PMMA spheres and the cations in solution. For this reason, we chose $ErCl_3$ precursor and $YbCl_3$ precursor[3]. It is worthwhile to mention that in this preliminary test an amorphous SiO_2 film deposited was used, with an amount of erbium of 1 mol%. The corresponding PL spectra was useful but will not predict in a precise way the emission of Er ions inside a nanostructured material like the opal.

5.2.1 Sedimentation

In order to test the Pl of Er in the co-doped suspension, an opal was co-assembled and co-doped by sedimentation, on a cleaned silicon substrate (Tab. 5.1).

PS microparticles	0.1 vol%
TEOS solution	1 vol%
$ErCl_3$	1 mol%
$YbCl_3$	3 mol%

Tab. 5.1 *Experimental concentrations for the preparation of the suspension for the sedimentation growth.*

Drying process was carried out inside an oven and the sample underwent the thermal treatment illustrated in the diagram of Fig. 5.2. The first stage starts at room temperature and reaches 70°C at a rate of 5°C/min, the second starts from 70°C up to 500°C at a rate of 1 °C/min and the third from 500°C up to 1000°C, at a rate of 3°C/min. The cooling is made following the natural thermal inertia of the oven.

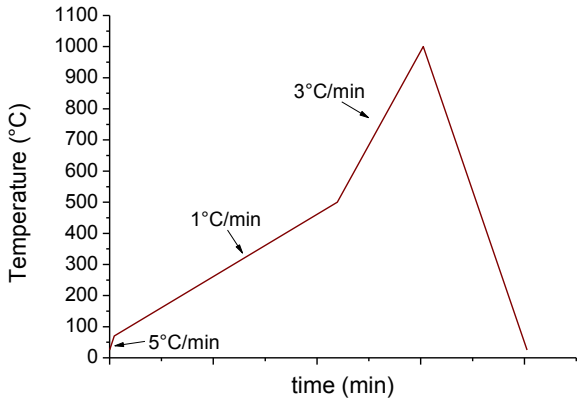

Fig. 5.2 *Thermal treatment underwent by the film sample.*

This treatment, mainly divided in two phases, has been chosen to the removal of the polymer template in the first phase (aiming at the inverse structure) and to the thermal annealing of the erbium at 1000°C. From literature, activation of erbium in silica colloids occurs only for anneal temperatures above 700 °C[4].

5.2.2 Results and discussion

Although opal-based structures can be obtained by sedimentation, in the present study the opal film revealed a white aspect without any iridescence when exposed to white light.

The PL properties in the NIR have been measured upon excitation at 975 nm, which causes the excitation of Yb^{3+} in silica by optical excitation into the $^4F_{5/2}$ manifold and energy transfer to the Er^{3+} $^4I_{11/2}$ manifold (as explained in Chapter 3).

The spectra performed with the excitation power of 5W and 7W, are presented in Fig. 5.3.

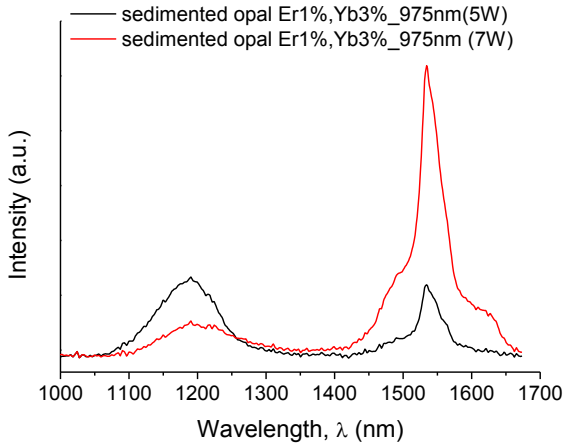

Fig. 5.3 *PL spectra performed on a co-assembled and co-doped opal (with Er mol1% and Yb mol3%) by sedimentation.*

In this spectrum, the characteristic Er emission peak at 1540 nm increases with the intensity of the excitation power. The 1200 nm broad peak is an artefact of the measurement operative procedure.

A broad emission spectrum, with a full width at half maximum (FWHM) of 31 nm can be observed. The presence of erbium is, for these results, detected inside an inverse opal structure and, even in case of few order, the crystalline nanostructure as host allows an enhancement of the emission, compared to the amorphous silicon oxide film as host[5-6], as seen in the comparative spectrum of Fig. 5.4.

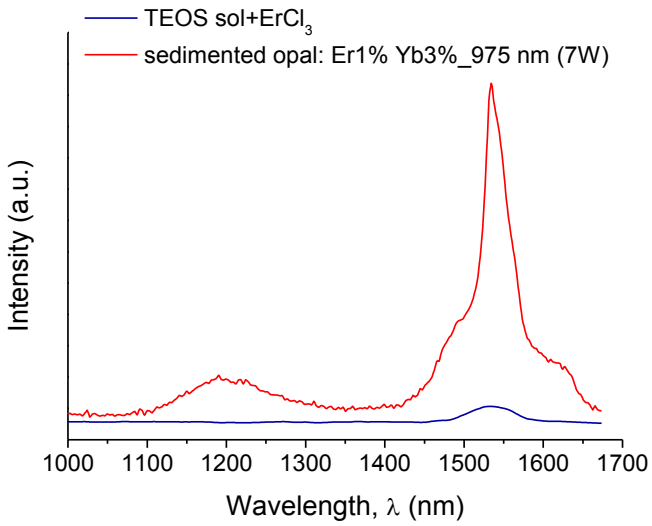

Fig. 5.4 *Comparison between the Er PL emission inside an Er doped amorphous silica matrix and a co-assembled co-doped inverse opal by sedimentation.*

5.2.3 Vertical deposition

To study the enhancement of the erbium emission in an inverse opal structure, the most promising idea is a fabrication obtained by vertical deposition, method which leads to good quality nanostructures.

PS spheres

Polystyrene (PS) commercial particles produced with an hydrophobic anionic surface have been tested. In order to test the Er PL, an opal of PS 870 nm spheres was co-assembled and co-doped. Before the opal growth, a comparative study has been made for testing different concentrations of RE ions, with the aim to ensure the homogeneity and the colloidal stability of the co-doped sol-gel solution with PS microparticles. These preliminary tests have been made reproducing the conditions of the opal growth (Tab. 5.2).

	Vol (ml)	**TEOS sol (vol%)**	**PS 870 nm (vol%)**	**Er (mol %)**	**Yb (mol %)**	**PRELIMINARY TEST**
S1	10	1%	0,1%	1	7,5	Flocculation
S2	10	1%	0,1%	1	3	Flocculation
S3	10	1%	0,1%	1	0	Stable, homogeneous aspect
S4	10	1%	0,1%	0,5	0	Stable, homogeneous aspect
S5	10	1%	0,1%	0	0	Stable, homogeneous aspect

Tab. 5.2 *Summary of the experimental concentrations of the preliminary tests for the PS 870 nm opals growth.*

After some hours, flocculation phenomena with formation of aggregates were observed in the suspensions S1 and S2, containing the greater amounts of RE ions. A photo of the flocculated suspensions is shown in Fig. 5.5:

Fig. 5.5 *Pictures showing the flocculation in the suspensions S1 (left) and S2 (right).*

From the results of this preliminary test, the threshold value for the incorporation of RE in the suspension seemed to be 1 mol%, in order to maintain the metastability of the colloidal suspension, but with kinetic stability.

The presence of RE ions affects the electric double layer potential of the PS colloidal particles, allowing flocculation, which decreases the Gibbs free energy of the colloidal system ("Colloidal stability" described in Chapter 2)[7].

Infiltrated opals have been prepared by vertical deposition method, with the Er concentration threshold value of 1 mol% and a lower one of 0.5 mol% (Tab. 5.3), following the operative procedure already described in Chapter 4.

	Vol (ml)	**TEOS sol (%vol)**	**PS 870 nm (%vol)**	**Er (mol %)**	**Yb (mol %)**	**OPALS**
S1	10	1%	0,1%	1	0	X
S2	10	1%	0,1%	0,5	0	V
S3	10	1%	0,1%	0	0	V

Tab. 5.3 *Summary of the experimental concentrations of the co-assembled co-doped opals of PS 870 nm spheres.*

The results show that an opal film/substrate adhesion is observed only for a RE doping level inferior to 0,5 mol%, with an aesthetic aspect showing very few traces of iridescence and a

very thin thickness. For all the other doping concentrations, PS spheres did not adhere to the substrate, which remained clean, due to the occurrence of flocculation phenomena.

The difference in the equilibrium doping concentration between the preliminary test and the opal growth can be due to the role of temperature; in fact, while the test was conducted at room temperature, the growth at 65°C could have an effect on the suspension, promoting the microparticles aggregation.

PMMA spheres

Polymethylmethacrylate (PMMA) commercial particles produced with an hydrophilic anionic surface have been tested for the co-doped co-assembled opal structures.

The objective was to compare the effect of the hydrophilicity of the polymeric microparticles on the interaction with the aqueous suspension containing the positively charged lanthanide ions.

Preliminary tests, analogous to the ones reported in Tab. 5.2 , have been made (Tab. 5.4).

The diameter of PMMA particles firstly used was 652 nm diameter, due to its more rapid availability.

	Vol (ml)	**TEOS sol (vol%)**	**PS 652 nm (vol%)**	**Er (mol %)**	**Yb (mol %)**	**PRELIMINARY TEST**
S1	10	1%	0,1%	1	7,5	Homogeneous aspect
S2	10	1%	0,1%	1	0	Homogeneous aspect
S3	10	1%	0,1%	0.75	0	Homogeneous aspect
S4	10	1%	0,1%	0,5	0	Homogeneous aspect
S5	10	1%	0,1%	0	0	Homogeneous aspect

Tab. 5.4 *Summary of the experimental concentrations of the preliminary tests for the PMMA 652 nm opals growth.*

As no flocculation occurred in the present case, the opal growth has been tried (Tab. 5.5).

	Vol (ml)	**TEOS sol (vol%)**	**PS 652 nm (vol%)**	**Er (mol %)**	**Yb (mol %)**	**OPALS**
S1	10	1%	0,1%	1	7,5	X
S2	10	1%	0,1%	1	0	X
S3	10	1%	0,1%	0.75	0	V
S4	10	1%	0,1%	0,5	0	V
S5	10	1%	0,1%	0	0	V

Tab. 5.5 *Summary of the experimental concentrations of the co-assembled co-doped opals of PMMA 625nm .*

The results show that only for a RE concentration lower than 0,75 mol% the adhesion of polymeric microparticles to the substrate occurs.

5.2.4 Results and discussion

PS co-assembled doped opals

The 0.5 mol% Er doped infiltrated PS opal has been characterized by optical reflectance and SEM (Fig. 5.6), to understand how the RE affect the self-assembly of the microparticles.

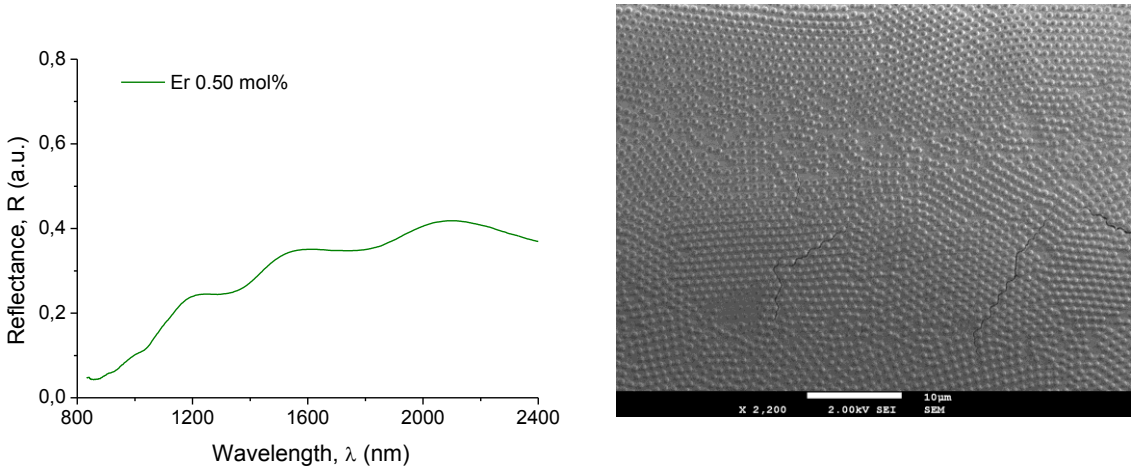

(a) *(b)*

Fig. 5.6 *Optical reflectance spectra (a) and SEM micrograph (b) of an infiltrated opal Er-doped 0.5 mol% of PS 870 nm.*

The Bragg peak is not detected and the SEM image confirms the lack of relatively big ordered domains. These results are an evidence that by adding the RE ionic salts the colloidal suspension of PS microparticles becomes unstable, the spheres flocculate and sediment, having a modification in the forces of attraction and repulsion and not allowing the self-assembly. A possible explanation can be linked to the negative charge of the anionic surface of PS microparticles, which mostly attracts the trivalent erbium ions and disrupts the local weak interactions equilibrium.

PMMA co-assembled doped opals

The control sample without erbium presents the Bragg's peak near the theoretical value of λ~1650 nm. Also in this case, with the increase of the erbium concentration, a destabilizing effect on the ordered arrangement of the structure can be clearly noticed, that conducts to the progressive disappearance of the Bragg peak (Fig. 5.7).

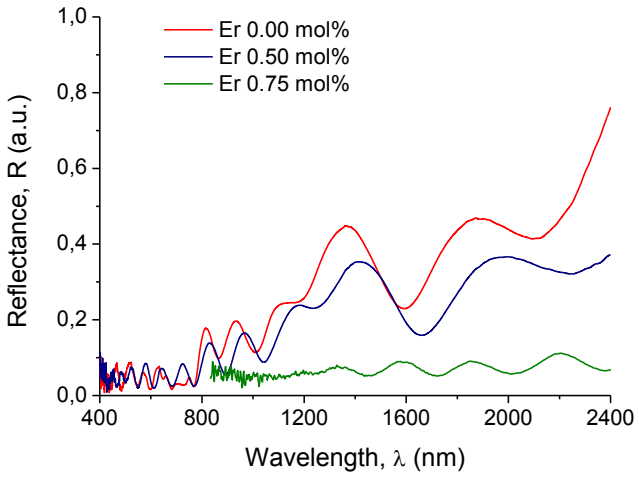

Fig. 5.7 *Comparison between optical reflectance spectra of co-assembled Er-doped opals of PMMA 652 nm, with the increasing of the doping level.*

To comment the morphology of these samples, SEM micrographs, at two different magnifications, are presented in Fig. 5.8.

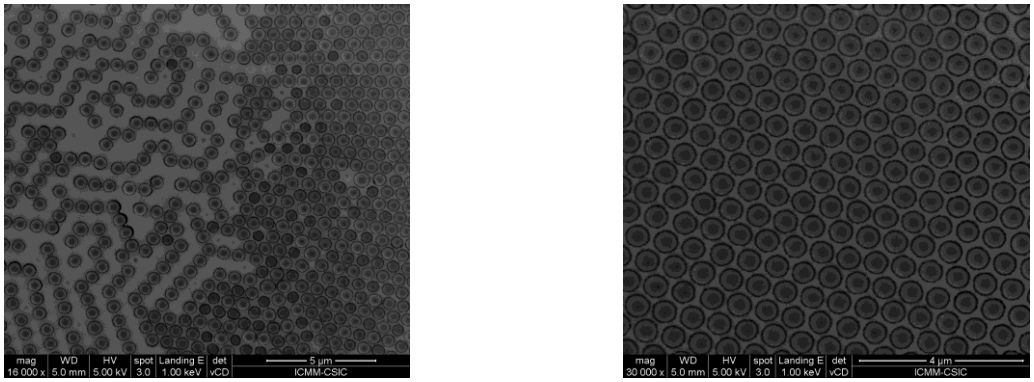

Fig. 5.8 *SEM micrographs of co-assembled Er-doped (0,5 mol%) opal of PMMA 652 nm.*

While in the left image the arrangement is completely random, some ordered regions are found at a more local level, at higher magnifications (right image).

Thus, even if the reflectance spectra do not show the stop band, these images prove that, for this size of spheres, the doping does not interfere totally in the self-assembly process.

Therefore, since no doped good quality opal structures were obtained by co-assembly method, a more deep analysis was carried out on the following experimental parameters:

- time of addition of RE ions during the sol-gel process;
- influence of RE precursor on the kinetics of the sol-gel;
- chemical species belonging to the Re precursor.

Time of addition of RE ions

The complete dissolution of RE precursor, with no visible clusters, is determinant for the incorporation of these RE inside the silica opal matrix.

RE were soluble in TEOS sol-gel solution independently on the addition time. The difference is in the way the RE precursor can interact with the other species in the sol-gel solution, before or after the complete hydrolysis of the silica. However, the silica chains formation is a kinetically slow process; it keeps reacting until at least one of the reagents will be finished.

Two procedures have been followed, for the growth of co-assembled Er-doped opals with PMMA spheres of 1 µm:

1. addition of the Er ions before the hydrolysis of TEOS and 1 h stirring (RE initial addition);
2. addition of the Er ions after 45 min of pre-hydrolysis of TEOS and 15 min stirring (RE final addition).

The optical reflectance spectra are reported in Fig. 5.9:

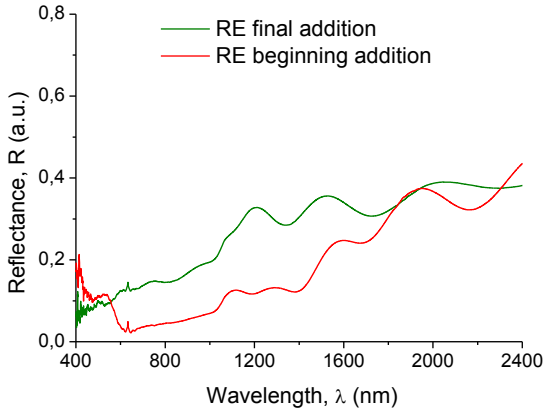

Fig. 5.9 *Comparison between co-assembled Er-doped opals of PMMA 1 µm with RE addition in the beginning or in the end.*

In the spectrum, diffraction peaks are not observed, so the time of RE addition is not a determinant parameter for the self-assembly.

Influence of RE precursor on the kinetics of the sol-gel

Co-doped opal-like structures obtained by co-assembly do not exhibit iridescence; at present, the aspect of the silica matrix is taken into account.

In particular, in the co-assembled Er-doped opal of Fig. 5.10, a disordered structure is observed (up image), joined to a granular aspect of the silica matrix, evidenced at bigger

magnifications (down image). It differs from the usual self-assembled ordered structure in a non doped opal and from its silica matrix homogeneous aspect (Fig. 5.11 up and down).

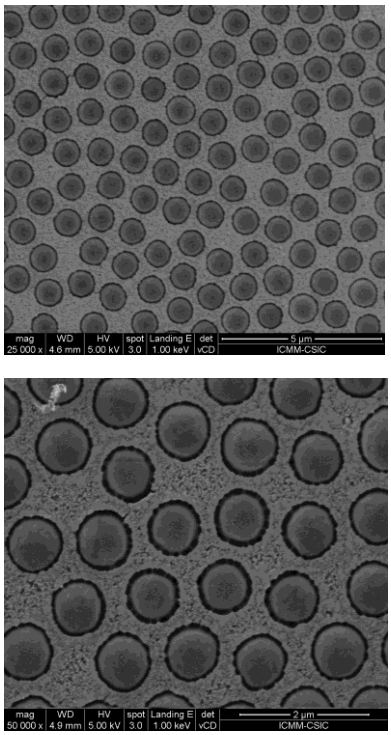

Fig. 5.10 *SEM micrographs of co-assembled Er-doped opal of PMMA 1µm, at different magnifications.*

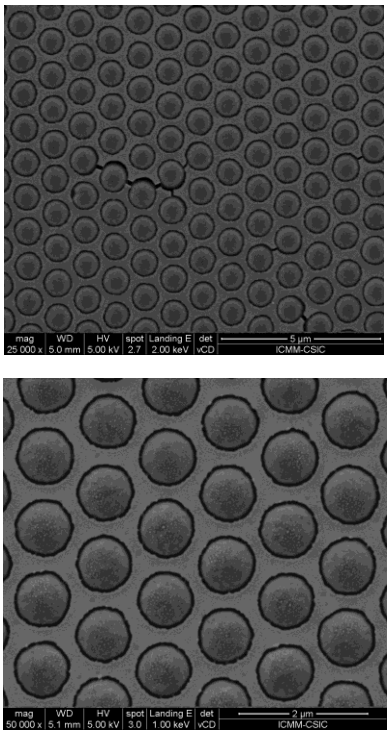

Fig. 5.11 *SEM micrographs of co-assembled non-doped opal of PMMA 1µm, at different magnifications.*

This can be probably due to the influence of the RE precursor ($ErCl_3$) in the silica chains formation and the granular aspect be explained by an increase in the reaction kinetics of the sol-gel.

To understand the role of Cl^- ions in the suspension, the trial of reducing the amount of acid catalyst in the composition of the TEOS solution has been made (Tab. 5.6).

	Vol (ml)	**TEOS sol (%vol)**	**TEOS sol composition (ratio in grams) EtOH:HCl:TEOS**	**PS 1 µm (%vol)**	**Er (mol %)**	**Yb (mol %)**	**OPALS**
S1	10	1%	1.5:1:1	0,1%	1	0	X
S2	10	1%	1.5:0.75:1	0,1%	1	0	X
S3	10	1%	1.5:0.5:1	0,1%	1	0	X
S4	10	1%	1.5:0.1:1	0,1%	1	0	X

Tab. 5.6 *Summary of the experimental concentrations of the co-assembled Er-doped opals of PMMA 1µm, varying the amount of HCl in TEOS solution.*

However, with these compositions the aspect of the opals does not result modified; the reduction of the amount of catalyst does not play an active role in promoting the co-assembly process.

Zeta potential measurements could be used for quantifying the magnitude of the electrical charge at the double layer and would be desirable for clarifying these occurring phenomena.

Modification of the RE precursor

Other precursors for erbium have been tested, since the Cl^- ion has resulted to affect in a negative way the development of the sol-gel reaction.

- **Precursor $Er(NO_3)_3$,** which has a PL emission efficiency comparable with $ErCl_3$ (Fig. 5.1). Although flocculation has not been observed, the adhesion of opals to the substrate was not acceptable (Tab. 5.7).

	Vol (ml)	**TEOS sol (vol%)**	**PMMA 1 µm (vol%)**	**Er (mol %)**	**Yb (mol %)**	**PRELIMINARY TEST**	**OPALS**
S1	10	1%	0,1%	1	7,5	Inhomogeneous aspect	X
S2	10	1%	0,1%	1	0	Stable, homogeneous aspect	X
S3	10	1%	0,1%	0	0	Stable, homogeneous aspect	V

Tab. 5.7 *Summary of the experimental concentrations for the PMMA 1 µm opals growth, with $Er(NO_3)_3$ as Erbium precursor.*

- **Precursor Er(2,2,6,6-tetramethyl-3,5-heptanedione)$_3$** has been tested to evaluate a precursor where the erbium is protected by organic groups and could be not so reactive like in salts precursors. $Er(thd)_3$ is a fairly bulk precursor molecule with the center Er^{3+} ion coordinated by three negatively charged β-diketonate ligands. Co-assembled opals have been produced with 1 mol% Er doping (Fig. 5.12 and Fig. 5.13).

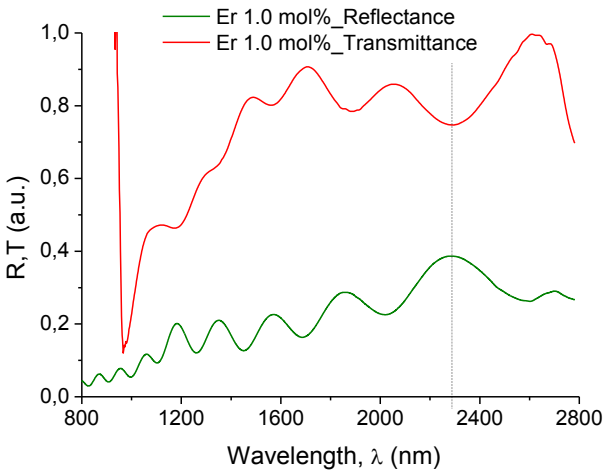

Fig. 5.12 *Optical reflectance spectra of co-assembled Er-doped (precursor Er(2,2,6,6-tetramethyl-3,5-heptanedione)$_3$) opal of PMMA 1 µm.*

EDAX ZAF Quantification
Element Normalized
SEC Table : Default

Element	Wt %	At %	K-Ratio
SiK	97.56	99.58	0.9444
ErL	2.44	0.42	0.0173
Total	100.00	100.00	

Element	Net Inte.	Bkgd Inte.
SiK	479.04	2.97
ErL	0.70	0.57

Fig. 5.13 *EDS analysis of Er presence in the opal structure.*

At first sight, the opal presents some traces of iridescence, which correspond to reflections in wavelengths of the VIS. The presence of these reflections belonging to stop bands of the second order suggests that those of the first order may be even more intense. The appearance of a wide Bragg peak can be recognized, placed in a position in agreement with the predicted theoretical values (~2200 nm). Furthermore, the EDS analysis reveals the presence of 2.44 wt% Er, incorporated in the silica matrix.

Thus, PL measurements were tried, but there was no evidence of the Er emission at 1.54 µm. Possible explanations are as follows:

- the excitation energy of 514 nm used in this laboratory for the PL measurements in case of doping with erbium has a low power (500 mW);
- the amount of material (emitter ion) that can be incorporated within the silica matrix is very low (1 mol%), because higher amounts give rise to flocculation phenomena. Moreover, this quantity should be considered only related to a theoretical percentage of 26% that represents the silica in an inverse opal FCC.
- the erbium efficiency is low because its effective cross-section of absorption is reduced.

Another condition concerns the obtaining of resonance properties in the inverse structure, by means of a high refractive indices contrast; at these conditions, the emitted radiation is not lost in the structure itself and an emission improvement can occur.

5.3 Rare earth co-doped artificial opals by Atomic Layer Deposition

The difficulties met in the RE doping of artificial opals by co-assembly has moved the research towards another doping technique, as to maintain the same investigation objective.
The Atomic Layer Deposition (ALD) is a technique which can allow the deposition of small amounts of active ions. It is performed in a second step, after the obtaining of the inverse opal structure, but has the advantage of avoiding the problems of the achievement of a kinetic stability in the suspension composed by the colloidal particles and the doping ions.
The objective is an homogeneous dispersion of erbium and ytterbium inside an inverse opal of non porous silicon, by means of this operative procedure:

- obtain a porous silicon inverse opal by co-assembly and magnesiothermic reduction;
- use the ALD to infill the RE ions (Er^{3+} and Yb^{3+}) into the pores of the porous silicon inverse opal;
- apply the CVD to fill the silicon porosities.

5.3.1 Atomic Layer Deposition

Atomic Layer Deposition (ALD) is an advanced technique for depositing metal oxide thin films[8].
To achieve a high concentration of erbium and ytterbium doping in inverse opal films, an alternative deposition of Yb_2O_3 and Er_2O_3 can be done using atomic layer deposition. The substrate used is a porous silicon inverse opal obtained from a silica inverse opal by magnesiothermic reduction (Chapter 4).
The deposition of Er_2O_3 thin films have been made by using Er(tetramethyl-3,5-heptanedione)$_3$ as precursor for the erbium[9]. β-diketonate complexes have been chosen for their thermal stability, but they do not readily react with water and require the use of a stronger oxidizer such as ozone (O_3)[10]. O radicals were found to create reactive sites for precursor adsorption and effectively remove the β-diketonate ligands.
Ozone (O_3) was produced from >99.999% oxygen (O_2) in an ozone generator (DelZone LG-7 CD Laboratory Ozone Generator) and used as oxidizer, while nitrogen (N) (>99.999%) was used as carrier and purge gas.
The deposition of Yb_2O_3 thin films have been studied by using Yb(tetramethyl-3,5-heptanedione)$_3$ for the ytterbium.

Stoichiometry and low impurity levels lead to stoichiometric oxides films, with some hydrogen (1.7-4.0 at%), carbon (0.5-1.8 at %) and fluorine (0.7-1.7 at%) as impurities.
The RE precursors peculiarities are summarized in Tab. 5.8:

Material	**Metal precursor**	**Oxygen source**	**Evaporation temperature (°C)**
Er_2O_3	Er(tetramethyl-3,5-heptanedione)$_3$ Er(thd)$_3$	O_3	160
Yb_2O_3	Yb(tetramethyl-3,5-heptanedione)$_3$ Yb(thd)$_3$	O_3	220

Tab. 5.8 *RE precursors peculiarities for the deposition of oxides by ALD.*

The doping level was controlled by varying the ratio of cycles of Yb_2O_3 : Er_2O_3 during deposition and a ratio of 7:1 was chosen.
Incorporation of erbium and ytterbium was carried out on the substrate at 300°C by depositing seven cycles of Yb_2O_3 and one cycle of Er_2O_3 in an alternating fashion (Tab. 5.9), for 40 cycles.

Chamber temperature	300ºC in the center 250°C in the edge
Er(thd)$_3$ pulsing time	0.01 s
Yb(thd)$_3$ pulsing time	0.01 s
N purge time	10 s

Tab. 5.9 *Parameters of the program used for the ALD deposition on porous silicon inverse opals.*

The growth rate (thickness increment during one cycle) for Er_2O_3 has a value of 0.25-0.3 Å/(cycle)$^{-1}$ and is obtained at optimal deposition temperatures, on silicon substrates. This represent a relatively low value, but, in this case study, it can be useful to have a more accurate control on the amount of erbium deposited, to avoid the damage of the interconnected structure during the deposition or excessive quantities, which can lead to quenching effects in the PL measurements.

Moreover, the film thickness is linearly dependent on the number of deposition cycles; this is a feature of ALD and it provides an easy and accurate way to control the film thickness.

Another interesting observation is that it has been found that the similarities in crystal structure and lattice constant between Yb_2O_3 and Er_2O_3 can allow a much efficient RE deposition, due to a higher concentration of Er^{3+} ions to be incorporated in a Yb_2O_3 host, compared to a SiO_2 host[11].

The RE deposition on the porous silicon inverse opal by ALD has been followed by the treatment with CVD (Chapter 4) to infill the silicon pores.

5.3.2 Results and discussion

During the whole deposition process, the observation of the pressure peaks, in correspondence of the alternating deposition of the Er/Yb precursors, is a first confirmation that the process has been successfully conducted.

The optical characterization of the co-doped silicon inverse opal obtained has been made, with the aim of verifying the maintenance of the interconnected 3D photonic structure after the doping process.

Reflectance spectra confirm the presence of the Bragg peak (at $\lambda \sim 1350$ nm) in the porous silicon inverse opal, before and after the deposition of RE ions by ALD (Fig. 5.14-left). The Bragg peak represents the permanence of the periodically ordered structure, which was not damaged during the treatment; SEM micrograph in Fig. 5.15 evidences the regularity of the FCC lattice of air spheres in a porous silicon matrix, giving a further confirmation to this assumption.

A peak redshift of ~50 nm can be noticed after RE deposition (Fig. 5.14-right); this can probably be explained by an increase of the effective refractive index of the co-doped structure, which corresponds to a lower band gap energy.

An EDS compositional analysis has detected the presence of Er/Yb inside the matrix and has given an estimate of their quantitative amount (Fig. 5.16).

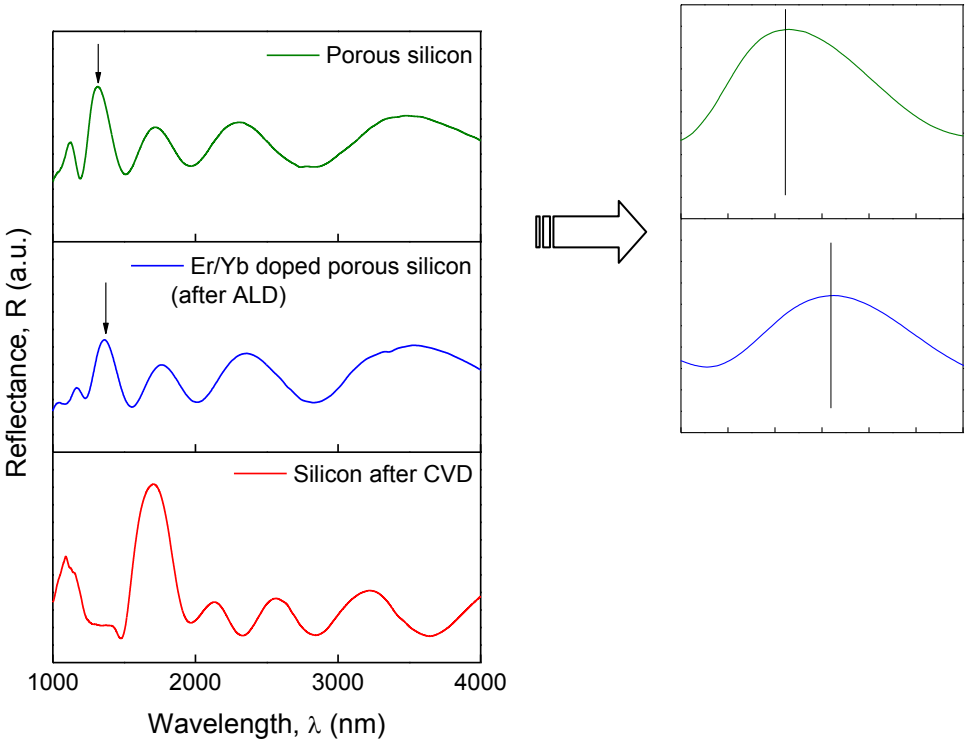

Fig. 5.14 *Optical reflectance spectra of porous silicon, co-doped porous silicon, non-porous silicon inverse opal of PS 870 nm.*

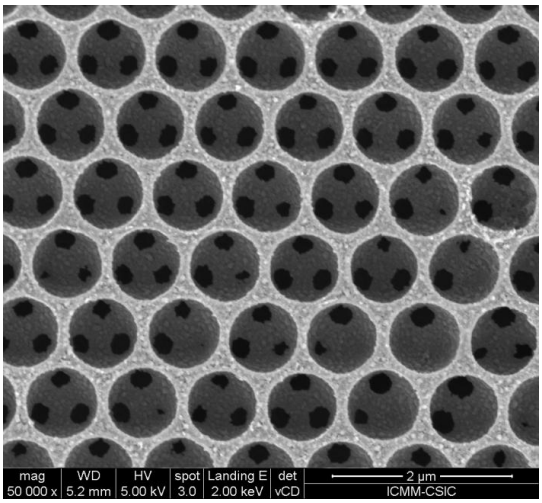

Fig. 5.15 *SEM micrograph of porous silicon inverse opal of PS 870 nm after co-doping by ALD process.*

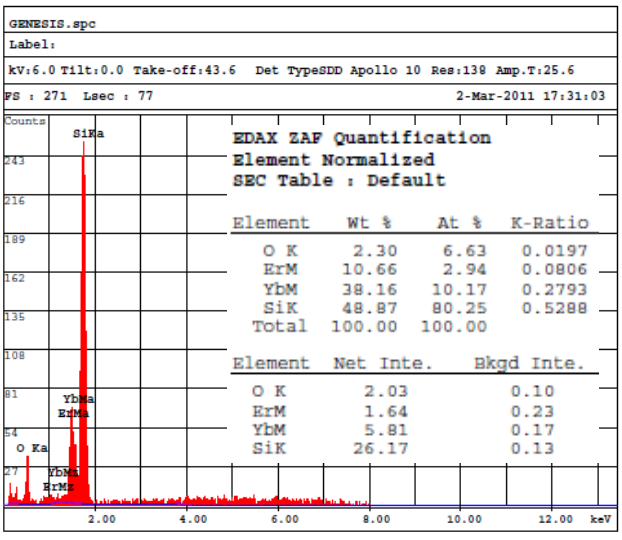

Fig. 5.16 *EDS analysis of Er/Yb presence in the co-doped inverse opal structure.*

At this point, we can therefore affirm that a nanostructure of silicon inverse opal co-doped with erbium and ytterbium has been successfully obtained, by a two-step procedure including the co-assembly method for the growth of the opal and the ALD method for the co-doping.

Consequent continuation will be the performance of PL measurements to determine the optical activity of the incorporated RE ions and to test the expected emission properties.
As reported in literature, a high temperature (above 700°C) annealing is always needed to activate the erbium ions, oxidizing them into the optically active Er^{3+} state[12].
However, considering the ALD deposition temperature, in some cases no annealing at high temperature could be required. In fact, it is specifically required for the elimination of -OH groups, which tend to be more present in processes carried out in aqueous phase (as the sol-gel method), in which the structure itself tends to trap more water.
The possibility of carrying out the ALD process in the vapor phase could, therefore, be an advantage for this purpose.
The co-doped nanostructure obtained is very promising, as the combined incorporation of Yb ions as sensitizer for the Er ions can lead to an increase of the erbium emission, due to the following peculiarities:

- the ALD allows an incorporation of a higher amount of material (emitter ions) inside the silicon matrix, programming the deposition of alternative cycles of the two RE precursors;
- the ytterbium efficiency itself is high, because its effective cross-section of absorption is about 25 times larger than the erbium one.

Moreover, the efficiency of energy transfer mechanisms is favored by the proximity between the RE ions, which is facilitated by this type of vapor-phase deposition.

5.4 Conclusions

- ***Co-assembly as a doping method***

The co-doping of co-assembled opals in one step by sol-gel method is a process very difficult to implement, in case of polymer colloidal spheres of big dimension (~1µm).

In fact, the insertion of salts (like $ErCl_3$, $Er(NO_3)_3$) inside a suspension composed of polymer microparticles can rapidly give rise to flocculation phenomena, directly proportional to the amount of salts, the time and the temperature.

For this reason, we were forced to conduct the majority of the tests for little concentrations of salts, which also can affect the colloidal stability, leading to the lack of self-assembly and adhesion of the artificial opal film on the substrates.

The study of different precursors for the erbium confirmed that the colloidal stability depends from the charge interactions between the surface of the polymer microparticles and the trivalent RE ions.

A precursor where the erbium ion is less reactive (due to the presence of bulky organic groups) showed some better results in the self-assembly of the opal structure and evidenced the presence of the Bragg peak in the reflectance spectrum, even if the amount of RE doping ions was still not enough sufficient to achieve PL results.

- ***Atomic Layer Deposition (ALD) as a doping method***

ALD is a viable technique which has proved to be successful in the co-doping with Er and Yb of porous silicon inverse opal structures.

This kind of doping procedure requires an optimization of all the deposition parameters to guarantee the control in the deposited thickness of material and the incorporation of a high concentration of erbium.

It does not allow the direct control on the spatial distribution of the RE ions, even if an homogeneous distribution of them inside the matrix is always desirable to avoid clustering and aggregation, which can lead to detrimental self absorption mechanisms.

The two-step procedure including the co-assembly method for the growth of the opal and the ALD method for the co-doping is an innovative work, presenting by the first time a RE active silicon inverse opal with expected laser emission properties.

References

1 Réfega, R. J. M. *Nanopartículas para Aplicação Biomédica* Mestre em Engenharia de Materiais thesis, Universidade Tecnica de Lisboa-IST, (2010).

2 Nie, Q. *et al. Effect of hydroxyl groups on Er3+ doped Bi2O3-B2O3-SiO2 glasses*, Journal of Physics and Chemistry of Solids, 68, 4 (2007) 477-481.

3 Mioduski, T., Guminski, C. & Zeng, D. *IUPAC-NIST Solubility Data Series. 87. Rare Earth Metal Chlorides in Water and Aqueous Systems. Part 3. Heavy Lanthanides (Gd--Lu)*, Journal of Physical and Chemical Reference Data, 38, 4 (2009) 925-1011.

4 Slooff, L. H., de Dood, M. J. A., van Blaaderen, A. & Polman, A. *Erbium-implanted silica colloids with 80% luminescence quantum efficiency*, Appl Phys Lett, 76, 25 (2000) 3682-3684.

5 Gu, Z.-Z. *et al. Varying the Optical Stop Band of a Three-Dimensional Photonic Crystal by Refractive Index Control*, Langmuir, 17, 22 (2001) 6751-6753.

6 Tsvetkov, M. Y., Samoilovich, M. I., Kleshcheva, S. M., Chigirinskii, Y. I. & Shushunov, A. N. *Rare-earth doped opal nanocomposites: technologies, photoluminescence and optimization*, Advanced Optoelectronics and Lasers, 2005. Proceedings of CAOL 2005. Second International Conference on 2(2005) 74 - 77.

7 Wu, K. L. & Lai, S. K. *Theoretical Studies of the Early Stage Coagulation Kinetics for a Charged Colloidal Dispersion*, Langmuir, 21, 8 (2005) 3238-3246.

8 Päiväsaari, J., Putkonen, M. & Niinistö, L. *A comparative study on lanthanide oxide thin films grown by atomic layer deposition*, Thin Solid Films, 472, 1-2 (2005) 275-281.

9 Niinistö, L., Päiväsaari, J., Niinistö, J., Putkonen, M. & Nieminen, M. *Feature Article: Advanced electronic and optoelectronic materials by Atomic Layer Deposition: An overview with special emphasis on recent progress in processing of high-k dielectrics and other oxide materials*, physica status solidi (a), 201, 7 (2004) 1375-1375.

10 Päiväsaari, J., Putkonen, M., Sajavaara, T. & Niinistö, L. *Atomic layer deposition of rare earth oxides: erbium oxide thin films from [beta]-diketonate and ozone precursors*, Journal of Alloys and Compounds, 374, 1-2 (2004) 124-128.

11 Van, T. T. & Chang, J. P. *Controlled erbium incorporation and photoluminescence of Er-doped Y2O3*, Appl Phys Lett, 87, 1 (2005).

12 Polman, A. *Erbium implanted thin film photonic materials*, Journal of Applied Physics, 82, 1 (1997) 1-39.

Final conclusion and future perspectives

The present work led to an optimization of an innovative method of co-assembly (based on a sol-gel route) as for the compositions, the parameters of the vertical deposition and the process variables, for the growth of co-assembled silica infiltrated opals.
The silica infiltrated opal constituted from 870 nm PS spheres has been used as a template for inverting the structure, which has been processed to obtain a silicon inverse opal. It presented iridescence and aesthetic quality and, at the same time, good optical properties of Bragg diffraction, with a stop band in the IR, centered in 1,54 μm.
The exploitation of this photonic band gap represents a new way of controlling and confining the light, inside a range of wavelengths of specific interest for the telecommunications field.

The opal-based structures have been integrated with RE emitter ions (Er/Yb), following two different operative strategies: the co-doping co-assembly method and the Atomic Layer Deposition (ALD).
The co-doping of co-assembled opals in one step by sol-gel method presented considerable difficulties of implementation, in case of polymer colloidal spheres of big dimension (~1μm), for the occurring of flocculation phenomena, due to charge interactions among the RE precursors and the polymer microparticles, which prevent the self-assembly.
A suggestion for the future work could be the execution of Zeta-potential measurements and the use of surfactants, aiming at the stabilization of the suspension.
The ALD method for the co-doping of inverse opals was successful and it is an innovative work, presenting by the first time a RE active silicon inverse opal.

Photoluminescence measurements are now under study to test the enhancement of the laser emission properties (in the IR) of the RE ions embedded in the 3D PhC structure obtained, in the perspective to the application of this effect in the optoelectronic field and in the realization of low-threshold nanolaser devices.

List of abbreviations

ALD = Atomic layer deposition

CVD = Chemical vapor deposition

EDS = Energy dispersive X-ray spectroscopy

FCC = Face centered cubic

FTIR = Fourier transform infra red spectroscopy

HCP = Hexagonal close packed

IR = Infrared

LDOS = Local density of states

NIR = Near infrared

PBG = Photonic band gap

PhC = Photonic crystal

PL = Photoluminescence

PMMA = Polymethylmethacrylate

PS = Polystyrene

RE = Rare earths

SEM = Scanning Electron Microscope

TEOS = Tetraethylorthosilicate

VIS = Visible

Acknowledgements

Reached the end of this path, I'd like to express my warmest thanks to my portuguese supervisor Profª. Drª. Maria Clara Henriques Batista Gonçalves for the opportunity given to participate in this research project, as well as to my italian supervisor Prof. Massimo Guglielmi for his suggestions and kind availability.

My sincere thanks to my co-supervisor Dr. Luís Miguel Amante Fortes, for his constant presence in every phase, as the help in the laboratory work and the daily prompt advice during the thesis writing.

Special thanks to all the "Photonic Crystal Group" of ICMM/CSIC of Madrid, for their warm welcome and useful discussions on the subject, especially to Dr. Marta Ibisate and PhD Student André Espinha, who gave me the best assistance in the samples fabrication and optical characterization. I was impressed about their great availability in sharing ideas and in realizing them. Your dedication and enthusiasm in the research work is admirable, and it was really a pleasure for me to stay with you during the three intensive weeks.

Furthermore, I am very grateful also to Eng. Isabel Nogueira and Andrés Valera, for the SEM images obtained, in Lisbon and Madrid respectively.

I'd like to mention FCT (Fundação para a Ciência e a Tecnologia) and ICEMS (Instituto de Ciência e Engenharia de Materiais e Superfícies) for the financial support and the given possibility of the transfer in Madrid.

Last but not least, I'd like to thank all the other students, who are working in the ICEMS laboratories (Rui, Elizabeth, Bruno, Gonçalo, Anandkumar, Alexandre) for their kindness and useful suggestions given me during these months.

Ringraziamenti

Alla fine di questi cinque anni di studio, conclusisi con la stesura della tesi presso l' "Universidade Tecnica de Lisboa-IST", sono molte le persone che mi sento in dovere di ringraziare per avermi accompagnato nel raggiungimento di un così importante traguardo.
Innanzitutto, la mia relatrice portoghese Profª. Drª. Maria Clara Henriques Batista Gonçalves per avermi dato la possibilità di partecipare a questo progetto di ricerca, e poi il mio relatore dell'Università di Padova Prof. Massimo Guglielmi per la fiducia accordatami.
Un grazie sincero al mio co-relatore Dr. Luís Miguel Amante Fortes, per la sua costante presenza in ogni fase della mia ricerca, sia nell'attività di laboratorio che nella prima stesura della tesi.
Un ringraziamento speciale è rivolto anche a tutto il gruppo di ricerca "Photonic Crystal Group" appartenente al ICMM/CSIC di Madrid, nella persona della Dott.ssa Marta Ibisate ed André Espinha, per l'amichevole accoglienza nel loro laboratorio e per tutto l'aiuto nella fabbricazione e caratterizzazione ottica dei campioni, nonché la grande disponibilità nel condividere idee e scelte operative.

Pensando agli anni di studio a Padova, il mio primo ringraziamento va ad Erika ed Irene, amiche e compagne insostituibili di tante ore di lezione, di spuntini veloci e di lunghe chiacchierate; in particolare ad Erika, compagna storica infaticabile di numerose preparazioni d'esami e, in molte occasioni, punto di riferimento prezioso in qualsiasi difficoltà.
Un grazie anche a tutti i colleghi di università, su cui so di poter sempre contare, assieme a tutti gli altri miei amici, che mi hanno sostenuto e dimostrato il loro affetto: a Marika, per avermi saputo ascoltare; a Beatrice, per i consigli di vita; a Kia, Ele e Angi, perché mi vogliono felice; a Chiara, perché sa rendere speciali anche le cose più semplici; a Mauro, per le consulenze informatiche gratuite e la sua estrema disponibilità, a Federico, per il suo saper capire ed essere presente al momento giusto.
"Obrigada" anche verso tutti gli amici conosciuti nei 7 mesi di Erasmus a Lisbona, per avermi insegnato ad apprezzare la bellezza delle cose semplici e dello stare insieme.
Non posso, infine, dimenticare di ringraziare i miei genitori, che mai mi hanno fatto mancare la loro comprensione ed il loro appoggio in ogni occasione.